1-1-1998

New pyroelectric phenomena from graded ferroelectric barium strontium titanate thin films

Feng Jin

NEW PYROELECTRIC PHENOMENA FROM GRADED FERROELECTRIC BARIUM STRONTIUM TITANATE THIN FILMS

by

FENG JIN

DISSERTATION

Submitted to the Graduate School

of Wayne State University,

Detroit, Michigan

in partial fulfillment of the requirements

for the degree of

DOCTOR OF PHILOSOPHY

1998

MAJOR: ELECTRICAL ENGINEERING

Approved by:

Gregg W. [illegible] 4/9/98

Advisor Date

Ratna Naik

[illegible]

[illegible]

To my wife and parents.

ACKNOWLEDGMENTS

I would like to thank my advisor, Prof. Auner, for suggesting me to work on this interesting research project, and for his support and help throughout my dissertation research.

I would like to thank Dr. Joseph Mantese, for letting me use the research facilities in General Motors Research laboratories, and for his support and help throughout this research project.

I would also like to thank my dissertation committee members, Prof. Pepe Siy, Prof. Ratna Naik and Prof. Franklin Westervelt for their time and support.

Special thanks go to the GM GFD's research team members, Norman Schubring, Antonio Catalan, Dr. Adolph Micheli and Majed Mohammed for their support and help throughout this research work.

I would like to thank Kim Scalise for proof reading the manuscript of this dissertation.

I would also like to thank the electronic shop and the machine shop at Wayne State University for their support and help.

TABLE OF CONTENTS

LIST OF TABLES

Table **Page**

LIST OF FIGURES

Figure **Page**

CHAPTER I

OVERVIEW OF FERROELECTRICITY AND ITS APPLICATION IN PYROELECTRIC INFRARED DETECTORS

1.1 PYROELECTRIC PHENOMENON

Pyroelectric materials possess a spontaneous or permanent polarization P_s even in the absence of an applied electric field. This polarization is governed by the crystal symmetry and bonding, and it also depends on material temperature. [1, 2, 3, 4] The pyroelectric effect arises when the polarization changes as temperature varies. Quantitatively, the pyroelectric effect can be described in term of the pyroelectric coefficient p, which is the rate of change of P_s with temperature, and thus:

$$dP_s = p\,dT \tag{1.1.1}$$

Pyroelectric effects occur in any material which possesses a polar point symmetry. Of the 32 point group symmetries, there are 11 that possess a center of symmetry, and have no polar properties. In such centrosymmetric crystals, the movements of charges, when under temperature perturbation or uniform stress, are symmetrically distributed about the center of symmetry, and thus cause no net charge displacement overall, and therefore exhibit no pyroelectric effect. The remaining 21 non-centric crystal point groups, all except one, exhibit electrical polarity or piezoelectricity when under stress. Among the 20 piezoelectric crystal classes, 10 of them have a unique polar axis/axes, and possess a spontaneous polarization. These are the materials that exhibit a pyroelectric effect, These ten classes of materials, grouped according to crystal system and can be

expressed using International notation of space group as: triclinic (1), monoclinic (2, m), orthorhombic (2mm), tetragonal (4, 4m), trigonal (3, 3m), and hexagonal (6, 6mm). [1, 4]

Microscopically, the pyroelectric effect occurs because of the asymmetric environment experienced by the electrically charged species within the crystal structure of the materials. It can be qualitatively understood by the following. The crystal structure of a pyroelectric material has a unique polar axis/axes, the charges (for instance, cations) are displaced from the center of gravity of the unit cells, and give rise to electrical dipole moments, or spontaneous polarization macroscopically. This polarization changes with temperature, since any excitation which causes change in lattice temperature will make the system change its energy from a lower energy state E_1 to a higher energy state E_2. Furthermore, because of the asymmetrical nature of the lattice, the E (energy) Vs. x (displacement) potential energy curves that the cations experienced are also asymmetrical. This means that they will form new equilibrium positions (from x_1 to x_2) when excited from E_1 to E_2, and therefore create a change in polarization.

1.2 PYROELECTRIC INFRARED DETECTORS

The change of polarization in a material causes a change in the surface charge of the material. So when a thin film of pyroelectric material is connected to a closed external circuit, as illustrated in Fig. 1.2.1, the temperature dependent polarization causes a current to flow through the circuit as the temperature of the material changes. [2, 5] The thin film acts as a current source, with the current is proportional to the rate of change of surface charge and the area of the material. This can be expressed as :

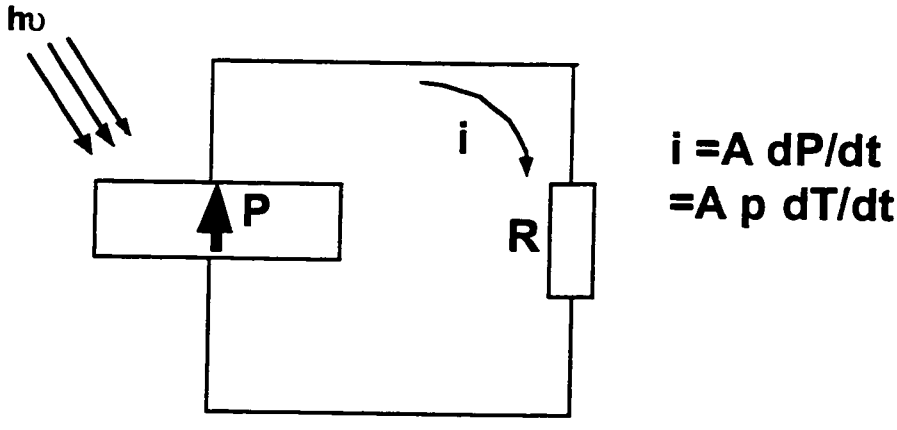

Fig. 1.2.1. A schematic diagram of a pyroelectric thin film connected in a simplified model circuit which shows a pyroelectric current flow due to the temperature change caused by infrared radiation.

$$i = A\frac{dP_s}{dt} \tag{1.2.1}$$

where A is the area of the material, P_s is the spontaneous polarization, and t is the time. Combined with Eq.1.1.1, we have:

$$i = Ap\frac{dT}{dt} \tag{1.2.2}$$

So from this equation we can see that the signal or the pyroelectric current from the film is proportional to the pyroelectric coefficient as well as the rate of change of temperature, which is proportional to the infrared radiation the material receives. This effectively makes it an infrared radiation detector. The fact that the pyroelectric current from this device is proportional to the rate of change of temperature, instead of temperature itself is a huge advantage for pyroelectric infrared detectors, and it is this characteristic of pyroelectric IR detectors that make them suitable for uncooled room temperature infrared detection.[2, 3, 5] Another major type of infrared detector, semiconductor infrared detectors (such as photon detectors, photodiodes, and Schottky-barrier detectors, etc.), require cryogenic cooling in order to suppress thermal noise. Thermal energy creates noise by exciting electrons to the conduction band in a photon detector, by generating electron-hole pairs in a photodiode, and by emitting thermal electrons in a Schottky-barrier detector.[6, 7] Unlike semiconductor detectors, pyroelectric IR detectors do not have to be cryogenic cooled in operation, since they only respond to the change of temperature, they can be operate at any temperature as long as the pyroelectric coefficient, or the sensitivity is high at that temperature. Furthermore, a mechanical chopper is required in front of a pyroelectric detector to create periodic change in infrared

radiation, and thus periodic change of temperature.[5, 8] So the signal from the detector has a definite frequency corresponding to the frequency of the mechanic chopper. By designing a proper filter circuit, for instance a mixer that mixes the signal from detector and chopper (reference), plus a low pass frequency filter, one can detect signals at a definite frequency (chopper reference frequency) and reject most other noise at the other frequencies.

Again, from Eq.1.2.2, it is obvious that a high pyroelectric coefficient p is desired. In all circumstances, the detectivity of a system is always directly proportional to the pyroelectric coefficient of the material,[2, 3, 8] and thus it is critical to obtain high a pyroelectric coefficient p, especially at the room temperature from detector material in order to achieve high sensitivity without cryogenic cooling. We should also point out that the overall performance of a pyroelectric IR detector is not solely determined by pyroelectric coefficient of the detector material, it also depends on many other characteristics of the detector and the detector material, such as the dielectric constant and the dielectric loss of the detector material, which affect the parasite capacitance and output impedance of the detector, and the thermal conductance of the detector material, which affect the thermal time constant of the detector, etc.. A figure of merit $F_v = p/c'\varepsilon_0\varepsilon$, is usually used to measure the performance of a pyroelectric material, c' here is the specific heat capacity of the material, ε, is the relative dielectric constant of the material, and ε_0 is the dielectric constant of air, [3] There are many compromises and trade off in circuit design in order to make the detector and the circuit work together to achieve the

highest possible performance. [2, 3, 5, 7, 8, 9, 10, 11]

1.3 FERROELECTRICITY

In most cases, the largest pyroelectric effects are observed in a class of materials, known as ferroelectrics.[1, 2, 3, 4] For a material in the ferroelectric state, the center of positive charges in the crystal does not coincide with the center of negative charges, i.e. a ferroelectric crystal exhibits electric dipole moments even in the absence of an external electric field. And the dipole moments have two different orientation states, which are identical in crystal structure and differ only in the direction of electric polarization at a null field. The direction of the dipole moments can be switch by the application of an electric field.[1, 12] A typical plot of polarization versus electric field for a ferroelectric crystal is shown in Fig.1.3.1. The loop is called a hysteresis loop, and it is a sign of a ferroelectric state. The basic characteristics of a hysteresis loop are also shown in Fig. 1.3.1. There are two stable polarization states or spontaneous polarization which are identical except the direction. The spontaneous polarization, P_s, can be reversed by the application of an electric field. The value of the spontaneous polarization, P_s, can be determined by extrapolating the saturation value of the electric displacement to zero field as indicated in the following equation:

$$D = P_s + \varepsilon E \qquad (1.3.1)$$

where D is the electrical displacement, ε is the dielectric constant, and E is the electric field. The field required to reverse the spontaneous polarization is called the coercive field

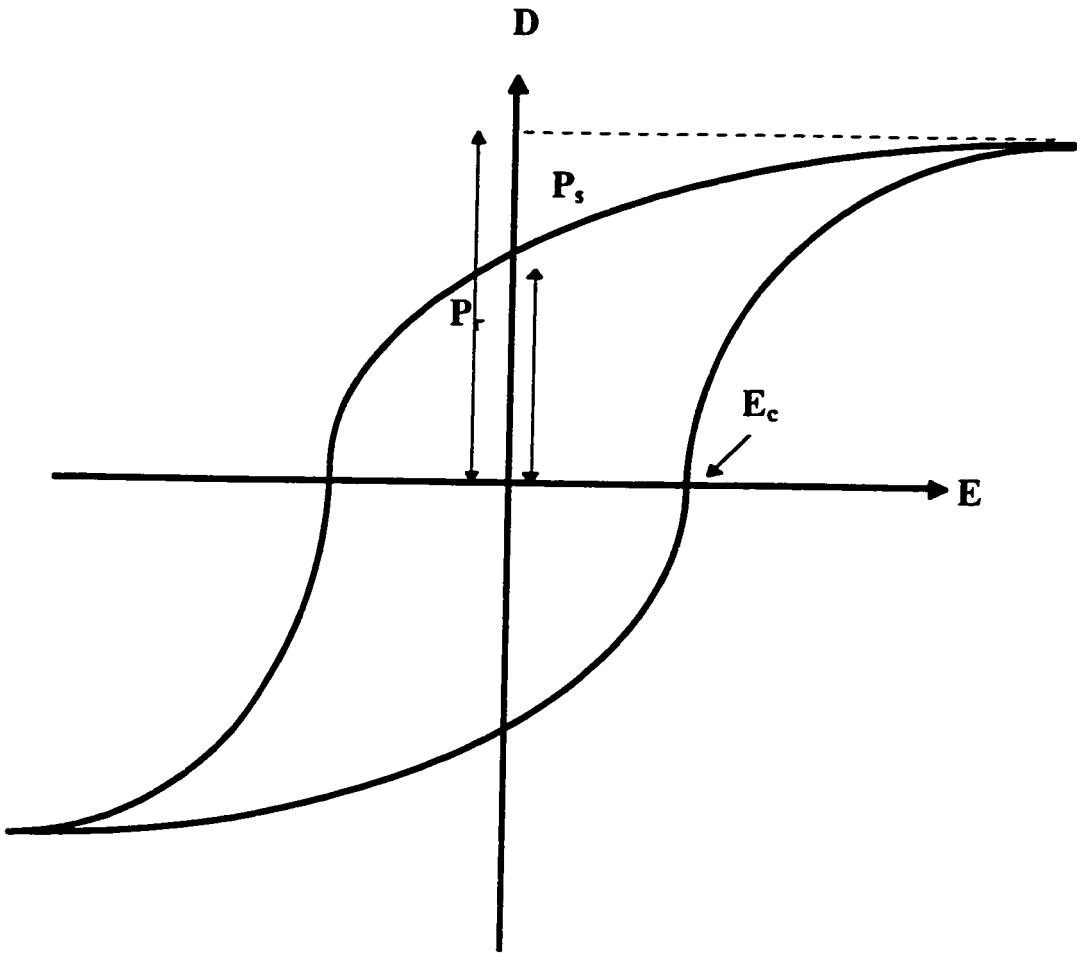

Fig. 1.3.1. A typical D vs. E hysteresis loop of a ferroelectric crystal illustrating the coercive field E_c, spontaneous polarization P_s, and the remanent polarization P_r.

E_c. The remanent polarization, P_r, is the polarization at zero field. [12, 13]

The hysteresis loop, which is a distinguishing sign of a ferroelectric state, can be measured using a Sawyer-Tower circuit as shown in Fig. 1.3.2.[14] In this measurement circuit, the horizontal channel of the oscilloscope is fed with the exciting electric field, and the voltage across the reference capacitor with known capacitance is sent to the vertical channel of the oscilloscope. Since the test sample and the reference capacitor are connected in series, the amount of charge on them are the same, and can be determined by:

$$Q = C_s V \qquad (1.3.2)$$

where C_s is the capacitance of the reference capacitor and V is the voltage across it. So the D vs. E plot, or hysteresis loop can be obtained by simply converting the scales of the display on the scope in the Sawyer-Tower circuit.

The highly temperature dependent spontaneous polarization of ferroelectrics make them a suitable class of material for infrared detectors.[2, 3, 5, 15] The definition of a pyroelectric coefficient is given in Eq.1.1.1. However, a pyroelectric detector can also be operated as a dielectric bolometer with an applied bias field, in this case, an induced pyroelectric coefficient is defined as:

$$p' \equiv \frac{dD}{dT} \equiv \frac{dP_s}{dT} + E\frac{d\varepsilon}{dT} \qquad (1.3.3)$$

and it is obvious that when there is no field, equation (1.3.3) becomes:

$$p = \frac{dP_s}{dT} \qquad (1.3.4)$$

which is the original definition of the pyroelectric coefficient. In both cases, as shown in Fig. 1.3.3, a change in temperature causes a change in surface charge, which is readily

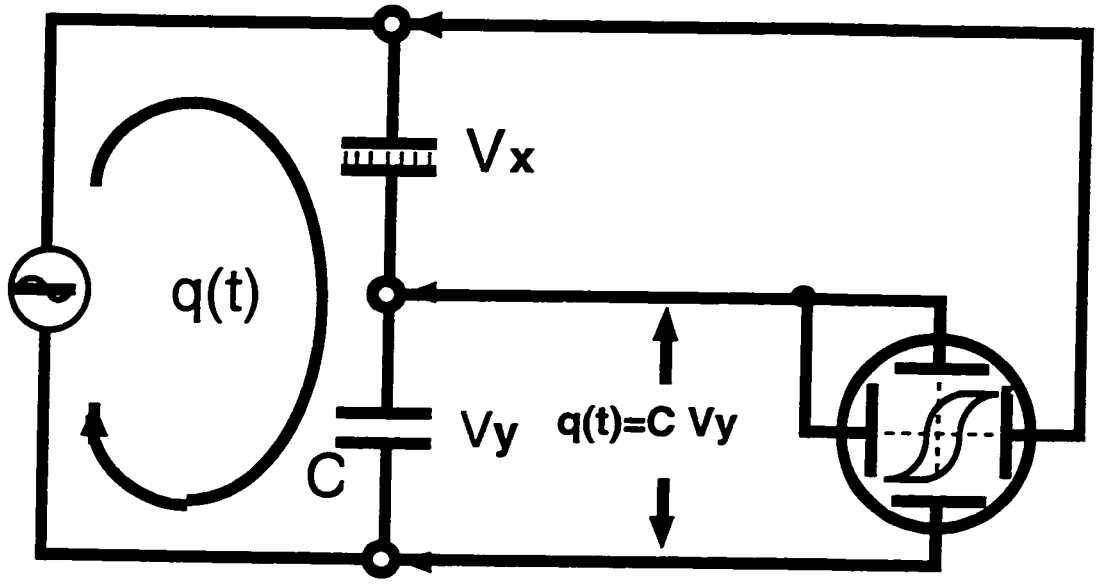

Fig. 1.3.2. The Sawyer-Tower circuit which is used to measure the D vs. E hysteresis loop of the ferroelectric materials.

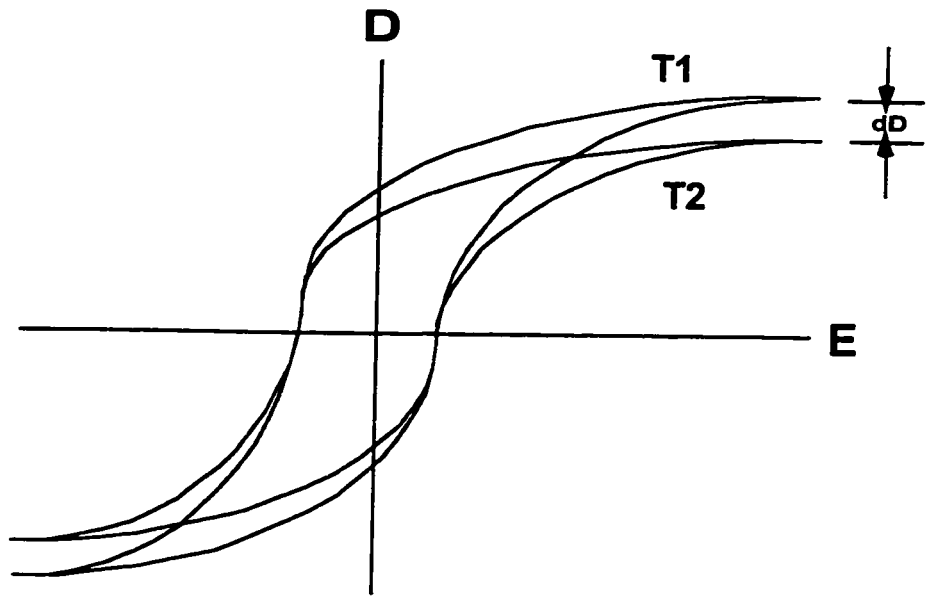

Fig. 1.3.3. The change in spontaneous polarization or D-E hysteresis loop of ferroelectric materials with temperature.

detected.

The ferroelectric character of a material usually disappears above a certain temperature called the phase transition temperature or Curie temperature. At the phase transition temperature, the crystal structure of the material translates from a polar low-symmetry ferroelectric phase to a non-polar high-symmetry paraelectric phase or so called prototype phase, and the spontaneous polarization of the material disappears.[3, 5, 13, 16] Fig. 1.3.4 is a schematic of a typical P_s versus T plot for a high quality crystal material. The pyroelectric coefficient, or the rate of change of P_s with respect to temperature, is usually high at near phase transition temperatures as illustrated in Fig. 1.3.4. It is at this temperature region that a pyroelectric detector has its maximum sensitivity. In additional to the disappearance of the spontaneous polarization, the change in crystal structure at the phase transition temperature also causes dramatic changes in the dielectric properties of the material. A rapid change in dielectric constant ε is often observed and this can be understood by the Curie-Weiss law which describes the dielectric constant ε at above T_c as:

$$\varepsilon = \varepsilon_0 + \frac{C}{T\text{-}T_c} \qquad (1.3.5)$$

where C is a constant, and T and T_c are temperature and phase transition temperature, respectively.

The change in crystal structure from ferroelectric phase to paraelectric phase can be described phenomenologically by the Landau theory of phase transition.[13, 16, 17, 18] Landau theory of phase transition says that the Gibbs free energy of a system can be

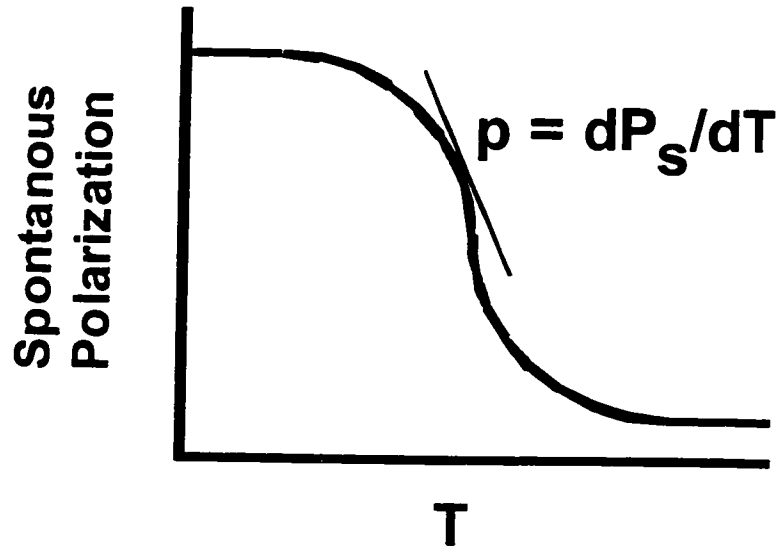

Fig. 1.3.4. A schematic showing the temperature dependency of spontaneous polarization of ferroelectric materials.

expanded in terms of field E, and a local order parameter δ, and we can write this in mathematical form as:

$$G = G0 + E\delta + \alpha\delta^2 + \beta\delta^3 + \gamma\delta^4 + ... \qquad (1.3.6)$$

where G_0 is the free energy at high symmetry phase, E is the field, δ is the local order parameter, and α , β and γ are material and temperature dependent coefficients. In particularly, for the ferroelectric to paraelectric phase transition in a ferroelectric crystal, the local order parameter δ, is the charge displacement or electric polarization, P. Also, as the two polarization states of a ferroelectric crystal, P and -P, are identical, every characteristic in the material system including free energy G is the same at P and -P polarization states, so the coefficients for the odd power terms in the above equation must be zero and can be discarded.[12, 13, 16] We let G_0 be zero to further simplify the analysis, and we can rewrite the equation as:

$$G = \alpha P^2 + \gamma P^4 + ... \qquad (1.3.7)$$

Landau chose the simplest form for α at near phase transition temperature[13, 16]:

$$\alpha = \lambda (T - T_c) \qquad (1.3.8)$$

so the sign of α changes from negative to positive as temperature passes through the phase transition temperature. We can find the spontaneous polarization, or the value of P, where the system has minimum G by solving the following equation:

$$E \equiv \frac{\partial G}{\partial P} = 2\alpha P + 4\gamma P^3 = 0 \qquad (1.3.9)$$

So, when $\alpha > 0$, or $T > T_c$, the system has minimum free energy G at P = 0, hence it is in

the paraelectric phase and has no spontaneous polarization. When $\alpha < 0$, or $T < T_c$, the system has a minimum free energy G at $P = (\alpha/2\gamma)^{1/2}$ and $-(\alpha/2\gamma)^{1/2}$. This is spontaneous polarization by definition since the field is zero in this case. Hence the material is in ferroelectric phase and has a net spontaneous polarization. We see that as the system approaches the phase transition temperature, or α approaches zero, the spontaneous polarization reduces and eventually disappears. This is illustrated in Fig. 1.3.5. By plugging the values of P back into Eq.1.3.8, we can find the depth of the well $G_{min} \equiv \alpha^2/\gamma$. The coefficients α and γ are temperature dependent so as temperature approaches the Curie temperature the depth of the double well decreases as illustrated in Fig. 1.3.5.

1.4 THE BARIUM STRONTIUM TITANATE MATERIAL SYSTEM

There is a very important group of ferroelectrics called perovskites. The general formula of this class of oxygen octahedra ferroelectrics is ABO_3.[19] As shown in Fig.1.4.1, the structure of perovskites can be described as a set of corner sharing BO_6 octahedras arranged in a simple cubic pattern, with in which the A cations occupy the central 12-fold coordinated sites. The A and B can be a variety of cations.

Among many perovskites, barium titanate ($BaTiO_3$) and strontium titanate ($SrTiO_3$), are most studied.[19, 20, 21, 22, 23, 24, 25, 26, 27, 28, 29] These two materials, as well as their solid solution barium strontium titanate ($Ba_xSr_{1-x}TiO_3$), have important applications in many different areas, such as dynamic random-access memories (DRAMs) because of their high dielectric constant.[30, 31, 32, 33, 34, 35, 36] Barium strontium titanate ($Ba_xSr_{1-x}TiO_3$) is also one

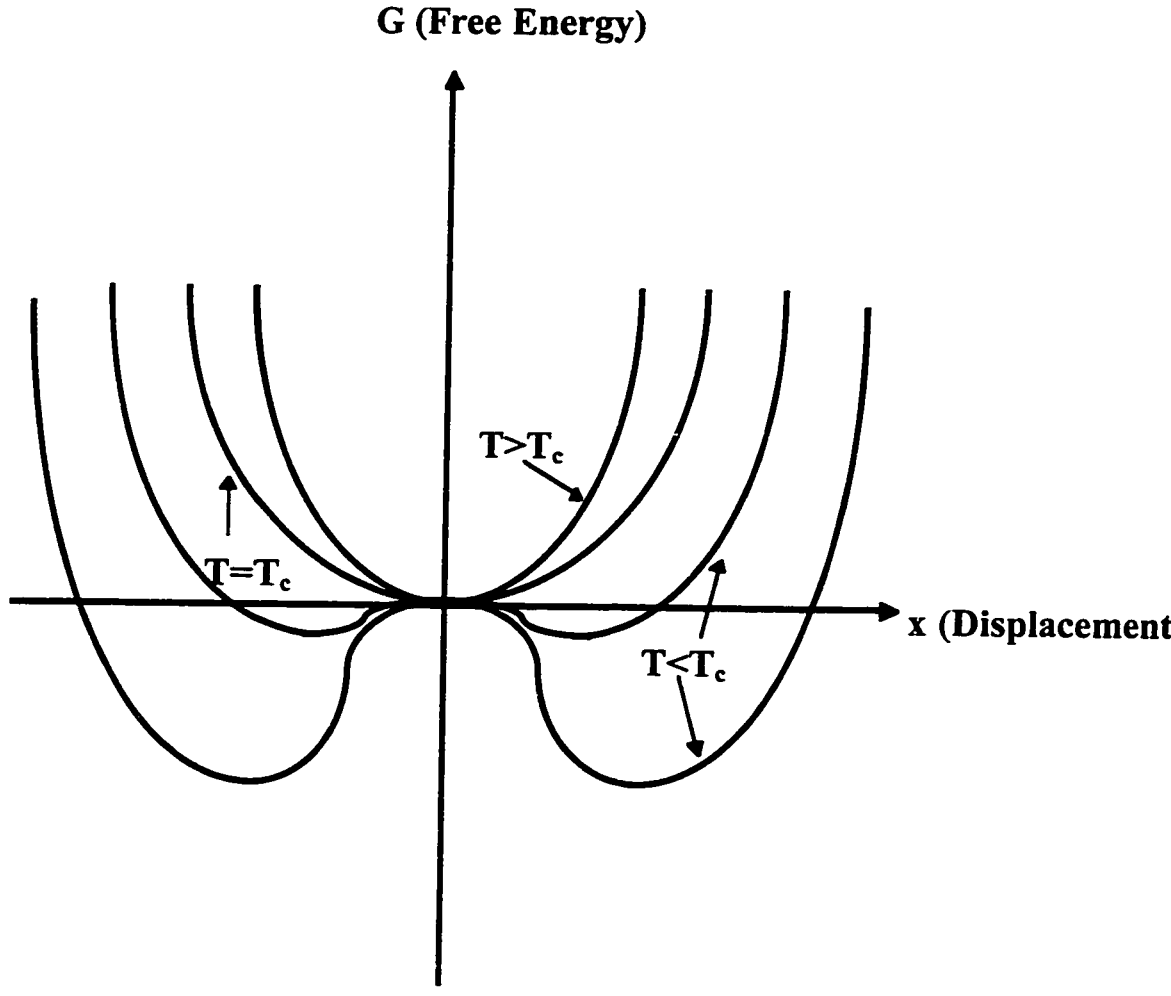

Fig. 1.3.5. Free energy of the ferroelectric materials as function of displacement of charge or polarization at various temperatures

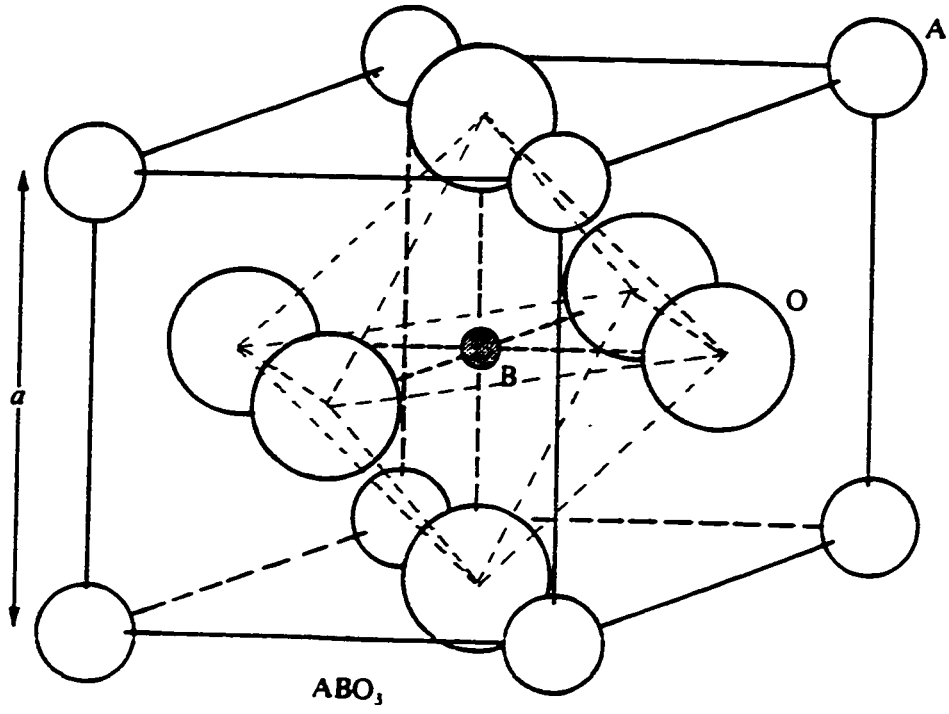

Fig.1.4.1. The ABO_3 perovskite structure. (from Ref. 19)

of the major candidates for pyroelectric infrared detector materials.[8, 37, 38, 39] Barium titanate ($BaTiO_3$) has three ferroelectric phases and one paraelectric phase, as shown in Fig. 1.4.2. At above 120 °C, it is in paraelectric phase, and has a prototype cubic perovskite structure. Below 120 °C, it transforms successively to: a tetragonal structure, then to a orthorhombic structure at about 5 °C, and finally to a trigonal structure at about -90 °C. For infrared detector applications, we are mainly interested in the phase transition from tetragonal structure (ferroelectric phase) to cubic structure (paraelectric phase). Dramatic changes in material properties were observed at ferroelectric to paraelectric phase transition temperatures.[4] As shown in Fig. 1.4.2, and also described by Curie-Weiss law (equation 1.3.5), the dielectric constants of the material changes rapidly at the phase transition region. Dielectric constants as high as 10,000 have been observed near the phase transition region. Also notice the anisotropic characteristic of barium titanate of the ferroelectric phases as indicated by the difference in dielectric constant along the a axis, ε_a, and the c axis, ε_c. The spontaneous polarization of barium titanate decreases as temperature increases and disappears as the temperature of the material reaches a transition temperature near 120 °C. The temperature dependency of the spontaneous polarization of barium titanate is sketched in Fig. 1.4.3.

Although barium titanate has a high pyroelectric coefficient and a high dielectric constant at near 120 °C, where the ferroelectric phase transition takes place, this temperature is too high for room temperature infrared detection. An alternative approach is to use barium strontium titanate $Ba_xSr_{1-x}TiO_3$, a solid solutions of $BaTiO_3$ and $SrTiO_3$.

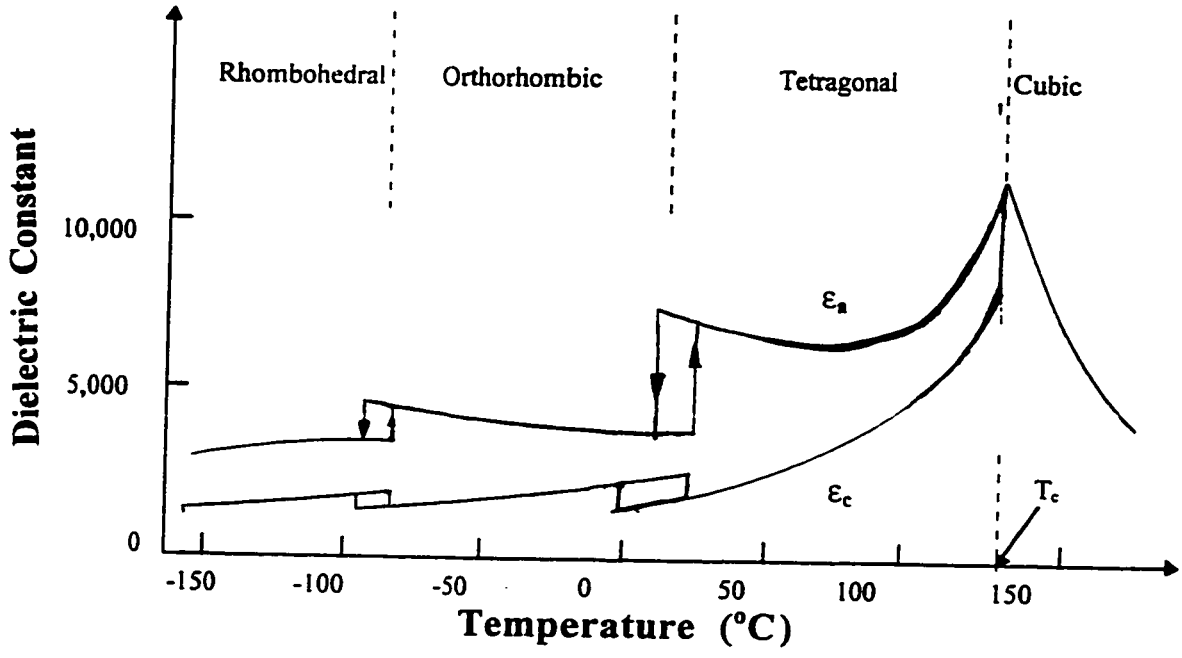

Fig. 1.4.2. The phase transitions for the barium titanate material system.

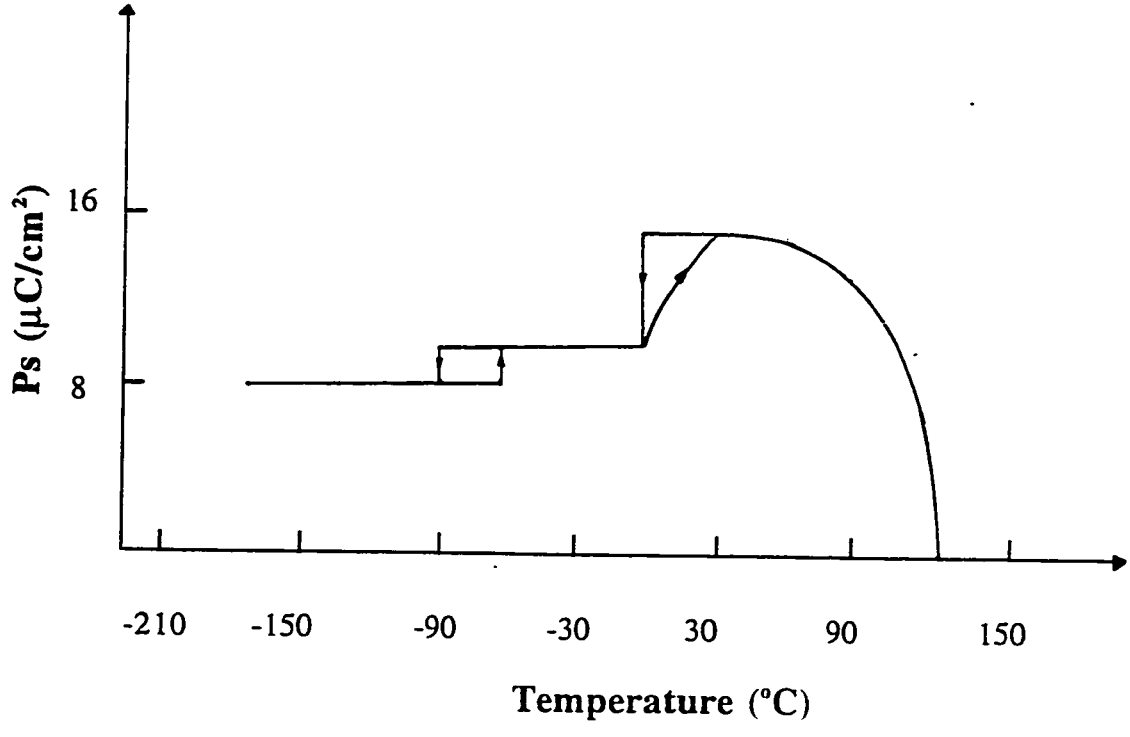

Fig. 1.4.3. Change in spontaneous polarization of barium titanate with temperature. (From Ref. 4)

Strontium titanate has a much lower tetragonal to cubic phase transition temperature at about -240 °C. By substituting some of the barium ions with strontium ions (some other cations as well) to form a barium strontium titanate solid solution, the Curie temperature can be lowered. When the Ba/Sr ratio equals 0.7/0.3, the tetragonal to cubic phase transition temperature is approximately room temperature. The effect of strontium and other substituting cations on Curie temperature of the solid solution is shown in Fig. 1.4.4.[1]

Barium strontium titanate (BST) single crystals or ceramics have high pyroelectric coefficients. The highest pyroelectric coefficient from BST, which is also the highest pyroelectric coefficient ever obtained from pyroelectric materials, is 23 $\mu C/cm^2$-°C.[38] But BST materials in single crystal and ceramic forms are difficult and expensive to fabricate. In modern microelectronics and opto-electronics, it is generally desired to have materials in thin film form so they can be mass produced inexpensively and incorporated into silicon chips. This is also true in the area of infrared image sensors, and many efforts have been directed in this direction.[40, 41, 42, 43, 44] Unfortunately, the material properties, such as pyroelectric coefficients for BST, are severely degraded in thin film form. BST thin films have pyroelectric coefficients usually only about 0.05 $\mu C/cm^2$-°C.[45] However, as we will briefly discuss in the next section, innovative structures of compositional graded ferroelectric devices exhibit new pyroelectric phenomena such as giant effective pyroelectric coefficients.

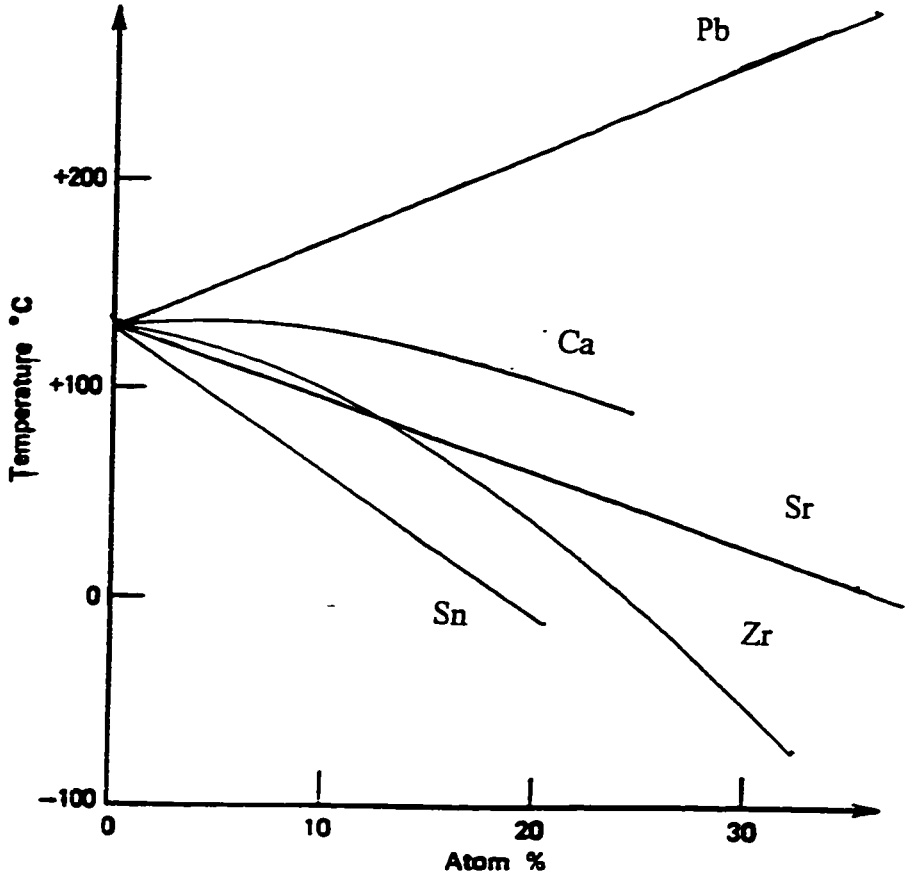

Fig. 1.4.4. Effect of Sr and other cations on the phase transition temperature.

1.5 GRADED FERROELECTRIC THIN FILMS AND DEVICES

Graded ferroelectric devices are not the only graded structures that exit. Before they were invented, other compositional graded structures, such as graded-index (GRIN) materials and functional graded materials had been studied.[46, 47] Graded-index materials or structures are mostly used in optical waveguides or semiconductor lasers, where spatial variation in refractive index helps confine light in certain narrow region. Functional graded materials combine different materials in a way to make maximum use of their proprieties. For example, a better aircraft coating material can be made by mixing a high heat resistive/less mechanic strength material with another high mechanic strength/less heat resistive material in a way that the former is facing outside, and the later inside, with the composition of the coating changing gradually in between, so the coating can make maximum use of the heat resistive and mechanic properties from these two different materials. It should be pointed out that both these two structures do not actually change the intrinsic properties of the materials, they only modify the intrinsic material properties spatially.

Graded ferroelectric thin film structures or devices, however, exhibit whole new pyroelectric properties which can be used to fabricate a new kind of highly sensitive pyroelectric infrared detector.[48, 49, 50] The first graded ferroelectric thin film structure created in General Motors R & D laboratories was a potassium tantalum niobate (KTN) thin film, in which there is a potassium concentration gradient normal to the films surface.[48] Compared to conventional thin films, as illustrated in Fig. 1.5.1, this film exhibited interesting new pyroelectric phenomena which was never observed in

conventional thin films. When excited with strong periodic electric field, the center of the ferroelectric hysteresis loop shifted from its original positions, showing a large unidirectional dc offset indicating a buildup dc voltage inside of the film. The dc offset of the hysteresis loops was field dependent, and increased with the periodic exciting electric field. It was also found that the dc offset, ΔD as shown in Fig. 1.5.1, was highly temperature dependent. An effective pyroelectric coefficient was defined as:[48, 49, 50]

$$p_{eff} \equiv \frac{d(\Delta D)}{d(\Delta T)} \qquad (1.5.1)$$

The film exhibited a giant effective pyroelectric coefficient orders of magnitudes higher than that normally observed in conventional ferroelectric thin films at near room temperature. This phenomenon may make it possible to use this effect to fabricate a new type of inexpensive thin film based uncooled IR detectors. Various experiments were performed by GM researchers which verified that this was indeed a new phenomenon, instead of surface rectification effects or instrumentation artifacts, etc..[48, 49]

Potassium tantalum niobate (KTN) is not an easy material system to work with, mainly because potassium is a very volatile species. Followed by the creation of compositional graded KTN films, a more stabled material system of compositional graded BST films with Ba and Sr compositional gradient normal to the films' surfaces were also made.[49] The films exhibited similar phenomena observed in KTN films such as dc offsets of the ferroelectric hysteresis loops when excited with periodic alternating electric field. The dc offsets were found to increase with the magnitude of the alternating electric excitation field. Graded BST films with different directions in compositional gradient

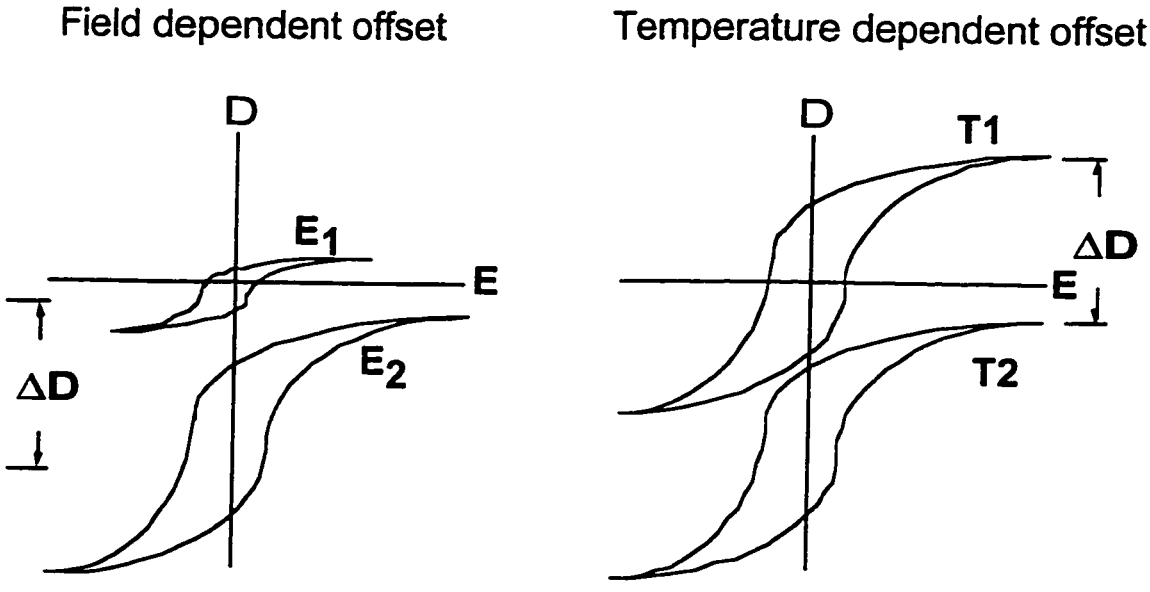

Fig. 1.5.1. Illustration of the new pyroelectric phenomena observed in GFD's. a) Field dependent offset of hysteresis loops. b) Temperature dependent offset of hysteresis loops.

were made, and the directions of the dc offset of the hysteresis loops were found to be determined by the directions of the compositional gradients of Ba and Sr.[49]

The compositional graded ferroelectric films mentioned above were all fabricated using the metalorganic decomposition (MOD) method.[48, 49] In the MOD fabrication process of graded BST thin films, layers of BST with different compositions were spin coated on platinum foil substrates and pyrolyzed progressively. The films were then annealed above 1000 °C which through the diffusion process to create the desired compositional gradient in the films. Although MOD is an easy and reliable way to form films, the major short comings are that it is hard to precisely control the compositional gradients using a thermal diffusion process and, more importantly, the high annealing temperature tends to create a lot of structural defects such as pin holes in the films formed. This has a tendency to degrade the properties of the graded thin films/structures. Furthermore, such high process temperatures are not compatible with IC or silicon processing. Hence a more controllable and advanced silicon compatible fabrication method for graded ferroelectric thin films was needed. Magnetron sputtering was adopted to fabricate graded BST thin films in this dissertation research.

1.6 Magnetron sputtering deposition method

Sputtering is a well developed deposition method which can be used in depositing nearly all kinds of materials.[51, 52] While sputtering involves many interrelated physical and chemical processes, and our understanding of this complex subject is still incomplete, the basic operational principle of sputtering is quite simple. Sputtering processes are

always carried out in a vacuum chamber, where a plasma is initiated and sustained by applying dc or rf power to the sputter sources (or cathodes). The sputter sources, with attached targets are negatively biased and are under constant bombardment of positive ions extracted from the plasmas. Some of the sputtered atoms from the target eventually condense on the substrates and form thin films.

Magnetron sputter sources are one of many types of different sputter sources.[51, 52] In a magnetron sputter source, magnets are incorporated, and are configured in a way to create a 50 to 500 gauss magnetic field in parallel with the target surface. The combination of the electric field from the external power suppliers and the magnetic field, cause the secondary electrons in the plasmas to drift in a closed circuit, or "magnetron tunnel", in front of the target surface. The confinement of electrons in this way significantly increases their distance of travel, and enhances the probability of ionizing more atoms before they reach the chamber wall. Magnetron sputter sources have plasmas that are more easy to initiate and sustain, and also, there is less e^- interaction with the substrate compared to non-magnetron sputter sources.

Both dc and rf power can be used in magnetron sputter sources. In this study, rf power was required because the targets (barium titanate and strontium titanate) are insulators. When a periodic rf power is applied to the sputter sources, the electrons and positive ions are attracted to the source target alternately. Since electrons are much lighter and response to high frequency fields much faster, they buildup near the surface of the source target, and induce a negative bias when in equilibrium. Hence the target source is a cathode.

1.7 OBJECTIVES

As discussed previously, the new pyroelectric phenomena exhibited in compositional graded ferroelectric thin films have great potential in application for room temperature infrared detection. The giant effective pyroelectric coefficients obtained from graded ferroelectric thin films structures are compatible with these observed in single crystals or ceramics, and as thin films are much easier and cheaper to make, thus opening the possibility of fabricating inexpensive highly sensitive infrared imaging sensors.

There are, however, major obstacles to overcome. First, the graded ferroelectric devices need to be reliably produced with a silicon compatible method, so it can be later adopted by the industry and incorporated into silicon IC chip manufacturing process and mass produced inexpensively. Second, the materials processing procedure needs to be optimized so the properties of the materials, mainly the effective pyroelectric coefficients, can be further improved to achieve maximum sensitivity in future detectors. Of equal importance is to understand the physics governing the new pyroelectric phenomena. This is a fundamentally new area which has not been fully explored, and there is a great possibility that more innovative applications other than infrared detectors will merge once the physics of this structure is clearly understood. It is therefore important to carry out a systematic structure and properties characterizations on graded ferroelectric thin films devices, and to correlate their microstructure and properties to theoretical understanding of the phenomena.

So, the objectives of this research work are:

- To develop a silicon compatible fabrication method for graded ferroelectric thin films.
- To improve the effective pyroelectric coefficients of graded BST thin films devices.
- To characterize the graded BST materials, and to correlate the structure and properties, and develop a phenomenological theory explaining the new pyroelectric phenomena.

In chapter II, "Growth and characterization of graded ferroelectric BST thin films", we will discuss the development of a rf magnetron sputtering method, which is silicon compatible, for fabricating graded ferroelectric BST thin films. We will also present results of basic structure and properties characterization of the graded ferroelectric BST thin films fabricated.

Chapter III, "Giant effective pyroelectric coefficients from graded ferroelectric BST thin films", is devoted to discuss the most important property from graded ferroelectric devices, the giant effective pyroelectric coefficients. We will show that giant effective pyroelectric coefficients two orders of magnitude higher than that of conventional BST thin films were obtained.

In chapter IV, "A phenomenological model of graded ferroelectric thin film devices", we will present a phenomenological model of graded ferroelectric thin film structures and explain the new phenomena observed from graded ferroelectric thin film structure qualitatively. Experimental evidence will be provided to support this model.

Finally in chapter V, "Summary", we will summarize our work and show that based on our model and understanding on the graded ferroelectric thin films devices, more improvements can be made.

CHAPTER II

GROWTH AND CHARACTERIZATION OF GRADED FERROELECTRIC BST THIN FILMS

In this chapter, details of the growth of compositional graded ferroelectric BST thin films is examined. Magnetron sputtering was adopted for growth of graded $Ba_xSr_{1-x}TiO_3$ thin films. Films with different directions of compositional gradients (x varies from 1 to 0.7, and x varies from 0.7 to 1) were grown using this method. Magnetron sputtering showed great control for fabricating graded thin films. Depth profile x-ray photoelectron spectroscopy (XPS) was used to verify the compositional gradient of the films, and the results revealed that they had almost uniform compositional gradients. The films were also characterized by x-ray diffraction, SEM, AFM, and dielectric constant and dielectric loss measurements. Wafer bow measurements were used to analyze the strain in the films formed.

2.1 INTRODUCTION

BST thin films have been grown successfully by nearly every major growth method, such as magnetron sputtering,[53, 54, 55, 56] pulse laser deposition,[57, 58, 59, 60] MBE,[61, 62] MOCVD,[63, 64] CVD,[65] sol-gel,[66, 67, 68] and MOD,[36, 45, 69, 70, 71, 72, 73] etc.. Graded ferroelectric BST thin films, however, have only been grown using metalorganic decomposition method (MOD).[49] MOD is a simple, low cost and easily controlled deposition method, and has generally been successfully utilized to create graded

ferroelectric thin films which were used to demonstrate the basic properties of this new structure.[48, 49] But the big disadvantage of this method is that it requires high anneal temperature to create a compositional gradient. Such high process temperatures are incompatible with silicon processing. It also creates a lot of structural defects such as pin holes in the graded BST thin films that degrade the properties of the film.

Magnetron sputtering is a widely used thin film deposition method in the semiconductor industry. In this study, a customized rf magnetron sputter deposition system was developed to fabricate graded ferroelectric BST thin films. Graded BST thin films with different compositional gradients were fabricated at about 500 °C, using rf magnetron sputtering.

As described in the previous chapter, the new pyroelectric phenomenon from graded ferroelectric devices is not only practically useful but also of fundamental theoretical interest. In order to understand the fundamental physics of this new structure, and develop a model to predict the properties of this new structure, detailed characterization of structure and properties of graded ferroelectric devices is necessary. In this chapter, we study and compare the structural, dielectric and electrical characteristics of the graded BST thin films with different directions of compositional gradient (up and down) and the homogenous BST thin films. X-ray diffraction was used to analyze the microstructure of the films. The strain in the films formed was analyzed using wafer bow measurements. The surface morphology of the films was examined using SEM and AFM. The dielectric properties of the films were also studied, the dielectric constant and the dielectric loss of the films at various temperatures were measured. The D-E hysteresis loops of the films

were obtained using the Sawyer-Tower circuit.

2.2 EXPERIMENTAL

2.2.1 The deposition system

A schematic of the dual-source rf magnetron sputter deposition system built for this study is shown in Fig. 2.2.2.1. Vacuum for the deposition system is provided by a diffusion pump combined with a rough mechanic pump. The diffusion pump is capable of working in an oxygen environment. The base pressure of the chamber is usually lower than 5×10^{-6} torr. The process gases are ultra high purity Ar and O_2, which are fed to the chamber to maintain the dynamic pressure of the chamber during film deposition. The dynamic pressure during deposition is controlled by a gate valve and can be adjusted. The flow rates of these two gases are controlled independently by two mass flow controllers. The O_2 is injected directly above the substrate via a gas ring, as shown in Fig. 2.2.1.1. This configuration makes efficient use of O_2 and allows a much lower O_2 relative concentration in the chamber during growth. This reduces the poisoning of the targets. The N_2 gas line is also connected to the chamber to provide an N_2 purge. The pressure of the chamber is measured by an ion gauge, a capacitance monometer gauge and a few thermocouple gauges, which cover a pressure range from atmosphere to 10^{-12} Torr. The substrate holder is placed right above a ceramic heater. The substrate temperature is controlled by the power applied to the heater and is measured by a thermocouple during growth. The substrate holder is also connected to a dc bias power supply to provide bias to the substrates. A quartz crystal thickness sensor is installed near the substrate holder

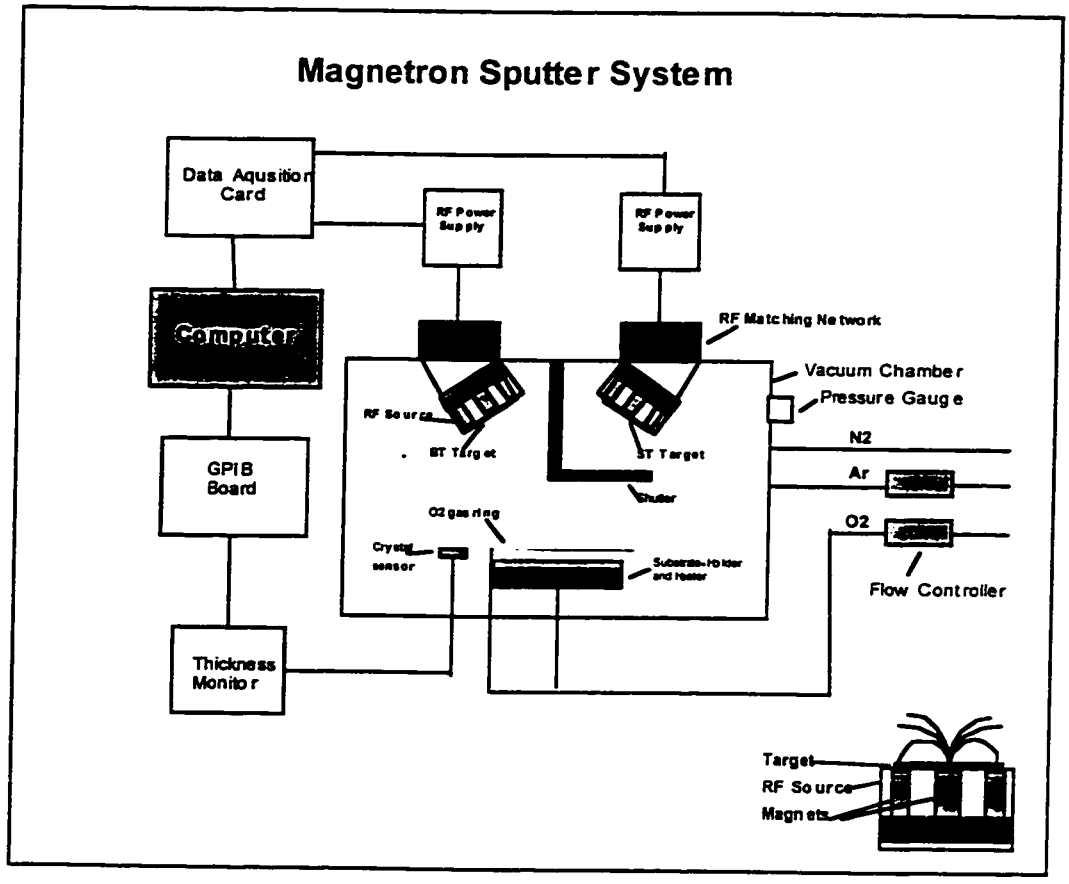

Fig. 2.2.1.1 The dual-source magnetron sputter deposition system built for this study.

to monitor the film thickness during deposition. The system consists of two magnetron sputter sources where $BaTiO_3$ and $SrTiO_3$ targets are attached. The magnetic field strength on the surface of the targets is around 300 gauss at center and 150 gauss at the rim. Details of the sources are also shown in Fig. 2.2.1.1. These two sputter sources are connected to two separate 13.6 MHz radio frequency power supplies, which are controlled independently by a computer. The sputtering rates of the $BaTiO_3$ and $SrTiO_3$ targets depend on the rf power supplied to the magnetron sputter sources. By adjusting the power levels sent to the two sources, the composition as well as the compositional gradient of the films can be precisely controlled.

The deposition process is controlled by a computer. The computer control program was developed using visual basic. A flow chart of the program is shown in Fig.2.2.1.2. During the deposition process, power sent to the two sputter sources is adjusted properly based on the increase in thickness of the film. The computer interfaces the thickness monitor through a GPIB board, and communicates with the two rf power suppliers through a multifunction data acquisition card which consists of I/O ports, A/D, and D/A converters. The computer reads the thickness of the film every few seconds, and according to the thickness, calculates the desired sputtering rates of the two targets, then converts them into power levels to the two sputter sources. The computer program also displays the progress of the deposition process on the screen and saves the data collected during the deposition into an Excel file at the end of the deposition run.

The sputter rate vs. power calibration curves for both $BaTiO_3$ and $SrTiO_3$ targets obtained by recording the sputter rates of the two targets at various power levels, and

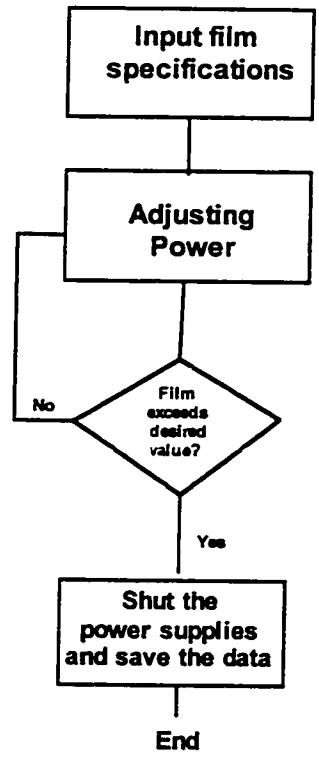

Fig. 2.2.1.2 The flow chart for the deposition control program.

plotting the rate vs. power curves. The change of sputter rate due to the power for the two targets were then empirically fitted into two mathematical formulas, which were stored in the control programs. Fig.2.2.1.3 shows the two rate vs. power curves obtained and the fitting formulas for these two curves.

2.2.2 EXPERIMENTAL PROCEDURE

The substrates used were platinum coated silicon. The substrates were cleaned in an ultra sonic cleaner using methanol, trichloroethylene, and isopropanol before loading into the deposition chamber. The chamber was pumped down to below 5×10^{-6} Torr before the deposition was initiated. The targets were pre-sputtered with the target shutter closed for half an hour before the actual depositions took place. The dynamic pressure was kept at about 2 mtorr, with an O_2 to Ar ratio equal to 1:100 during the deposition. The flow rates of Ar and O_2 were maintained at 70 SCCM and 0.7 SCCM, respectively. The substrates were heated to 500 °C during the deposition. The deposition parameters are summarized in tab. 2.2.2.1. The desired film specifications, such as total film thickness and compositional gradient, were input into the computer program before each deposition

Table 2.2.2.1 Film deposition parameters

Temperature (°C)	Base pressure (torr)	Dynamic pressure (torr)	Flow rate (SCCM)	O_2/Ar ratio
500	5×10^{-6}	2×10^{-3}	70 (Ar), 0.7 (O_2)	1:100

process started. The film thickness was monitored constantly by a quartz crystal thickness sensor, and the signal was fed to the computer during the deposition. According to the film thickness and the desired film specifications, the computer adjusts the power

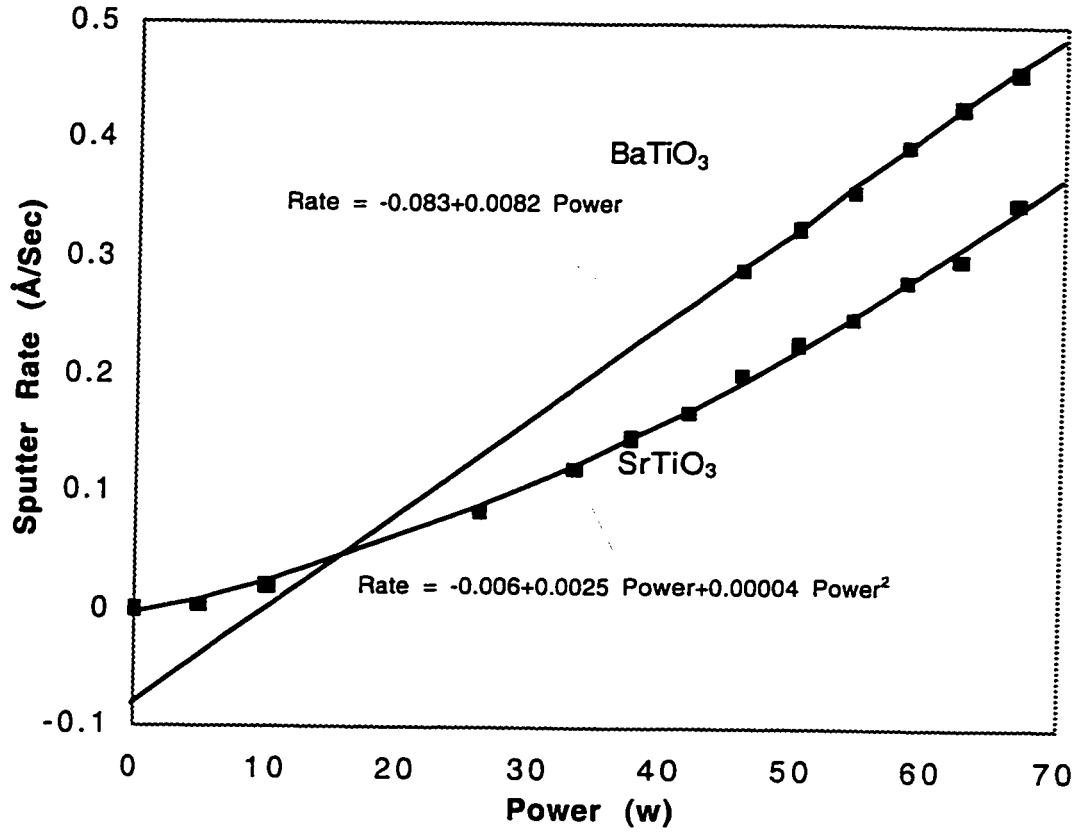

Fig. 2.2.1.3 The sputter rate vs. power relation for the $BaTiO_3$ and $SrTiO_3$ targets.

sent to the two targets tuning the sputtering rates of the two targets throughout the deposition process in order to achieved the desired compositional gradient in the film.

X-ray photoelectron spectroscopy (XPS) was used to verify the compositional gradients of the films. The microstructure of the films was analyzed using x-ray diffraction. A Cu K_α line ($\lambda = 1.5412$ Å) was used. . The strain in the films formed was analyzed by wafer bow measurements, which was performed using a profile meter. Scanning electron microscopy (SEM) and atomic force microscopy (AFM) were used to examine the surface topology of the films.

In order to perform the electric measurements, gold/chromium electrodes were deposited on the top of the films using e-beam evaporation. The area of each electrode was 0.02 cm^2. It consisted of a 600 Å chromium bottom layer and a 3000 Å gold top layer. These contacts served as top electrodes, while platinum on the bottom served as the bottom electrode for the electric measurements.

Dielectric properties of the films, such as low-field permittivity and dissipation factor at various temperatures, were characterized using a 4192A Hewlett Parkard impedance analyzer with an MMR temperature microprobe station. The latter instrument was used to regulate the temperature to within 0.05 °C. A modified Sawyer - Tower circuit was used to measure large-field excitation D vs. E hysteresis loops for the films[14]. The circuit is shown in Fig. 1.3.2. The value of the reference capacitor C_s in the circuit was 1 uF for this study.

2.3 RESULTS

Compositional graded BST thin films with different directions of compositional gradient, as well as homogenous BST thin films were deposited on platinum coated silicon substrates by rf magnetron sputtering. The films were characterized by different techniques as being discussed below.

2.3.1 Compositional Gradients of the films

The compositional gradient of two types of graded films were examined. The first film type was designed to be a 200 nm graded $Ba_xSr_{1-x}TiO_3$ thin film with uniform compositional gradient down (from $BaTiO_3$ (bottom) to $Ba_{0.7}Sr_{0.3}TiO_3$ (top)). The second film type was designed to be a 200 nm graded $Ba_xSr_{1-x}TiO_3$ thin film with uniform compositional gradient up (from $Ba_{0.7}Sr_{0.3}TiO_3$ (bottom) to $BaTiO_3$(top)). The powers to the two sputter sources/targets during these two deposition processes are shown in Fig.2.3.1.1a and Fig. 2.3.1.2a. For the first film, we can see that the power to the $BaTiO_3$ target decreased, and power to the $SrTiO_3$ target increased as the deposition process proceeded. As the result of this continuous change in power levels to the two targets, a 200 nm compositional graded $Ba_xSr_{1-x}TiO_3$ thin film with continuous composition change from $BaTiO_3$ (bottom) to $Ba_{0.7}Sr_{0.3}TiO_3$ (top) was made, as shown in the XPS depth profile in Fig. 2.3.1.1 b. The continuous tuning of the relative power levels by the computer, via a 12 bit digital to analog converter, gave a graded BST thin film with almost uniform compositional gradient. Similar results were obtained the second film, as shown in Figure 2.3.1.2. The XPS result for this film also indicates the formation of a 200 nm

compositional graded $Ba_xSr_{1-x}TiO_3$ thin film with continuos composition change from $Ba_{0.7}Sr_{0.3}TiO_3$ (bottom) to $BaTiO_3$ (top).

From the above discussion, we see that this newly developed computer controlled rf magnetron co-sputter deposition system has the capability to fabricate graded thin films with great precision. Of equal importance in this particular application is that this is a relatively low temperature process (at about 500 °C), and is silicon compatible. It is also important to note that, as rf magnetron sputter is a widely used deposition method, and virtually all types of materials can be deposited by this method, this graded thin film fabrication technique is very flexible and is not limited in fabricating ferroelectric BST thin films, it can be extended to fabricated other kinds of graded thin films as well.

2.3.2 X-ray diffraction and wafer bow measurement results

X-ray diffraction results show that all of the films were polycrystalline. Fig.2.3.2.1, Fig. 2.3.2.2, and Fig. 2.3.2.3 are the x-ray diffraction results from the graded (down) BST film, the graded (up) BST film, and the homogenous BST film, respectively. Multiple BST diffraction peaks, (001), (011), (111), (211) as well as the Pt (111) diffraction peak, were observed from these films. The graded films appeared to be partially oriented as evidenced by the relative intensities of the diffraction lines from the films. For the graded(down) film, the dominant diffraction line observed was (111), which indicates the films were partially oriented along the (111) direction. For the graded (up) film, the dominant diffraction line observed was (001), which indicates the films were partially

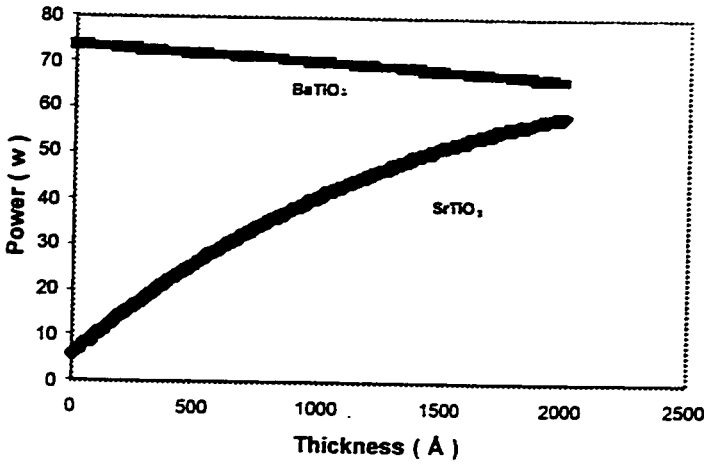

(a)

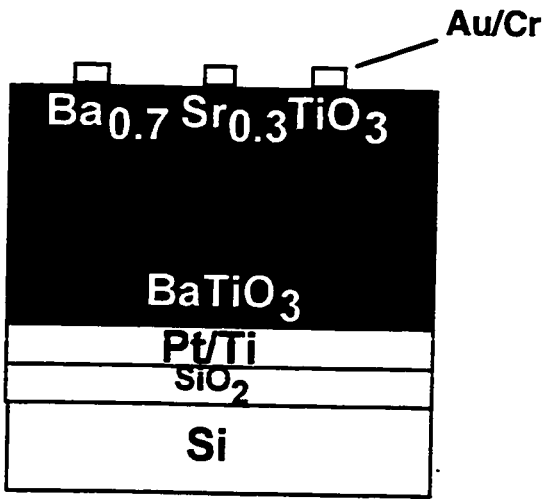

(b)

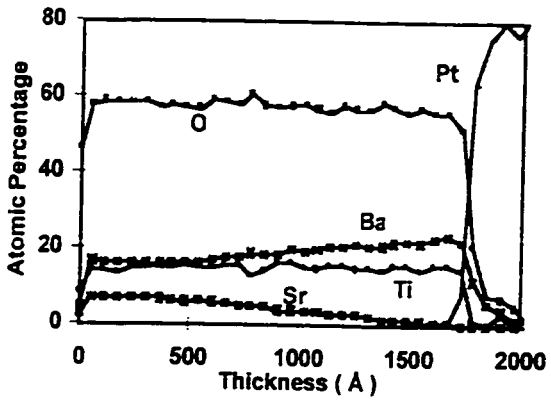

(c)

Fig. 2.3.1.1 Formation of graded down BST film. a) The change of the powers sent to the two targets during the deposition.
b) The schematic of graded down BST thin film structure.
c) The depth profile XPS showing the compositional gradient of the film.

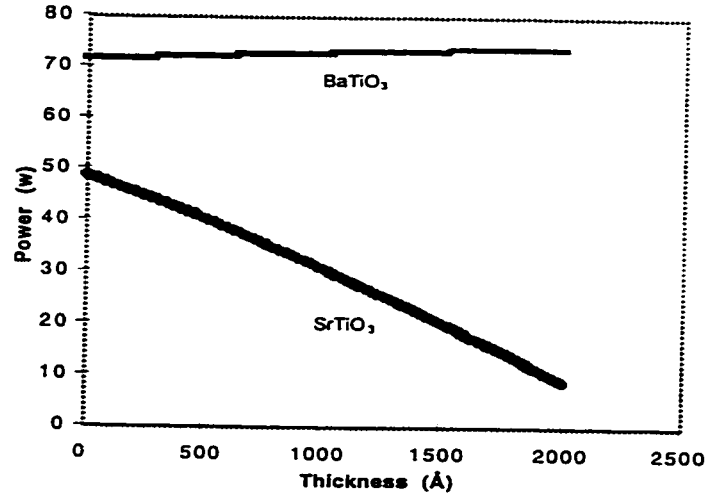

(a)

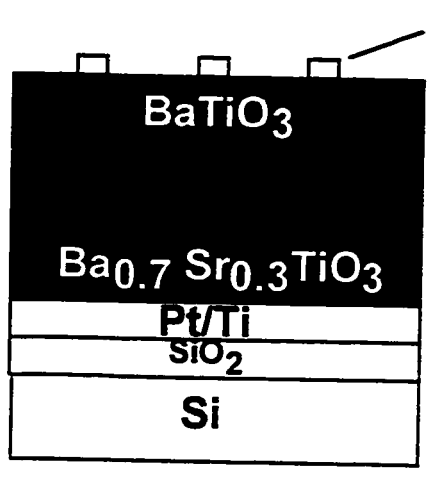

(b)

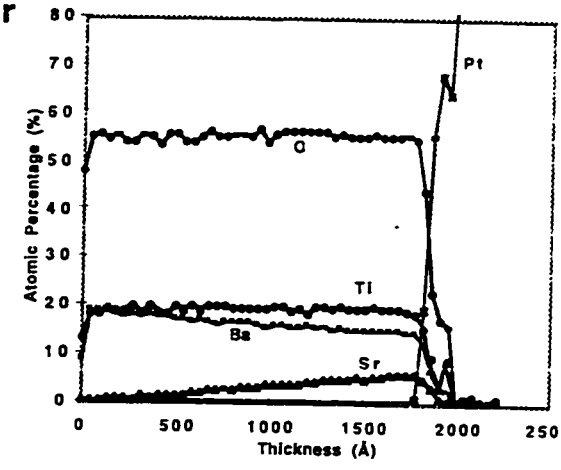

(c)

Fig. 2.3.1.2 Formation of graded up BST film. a) The change of the powers sent to the two targets during the deposition.
b) The schematic of graded up BST thin film structure.
c) The depth profile XPS showing the compositional gradient of the film.

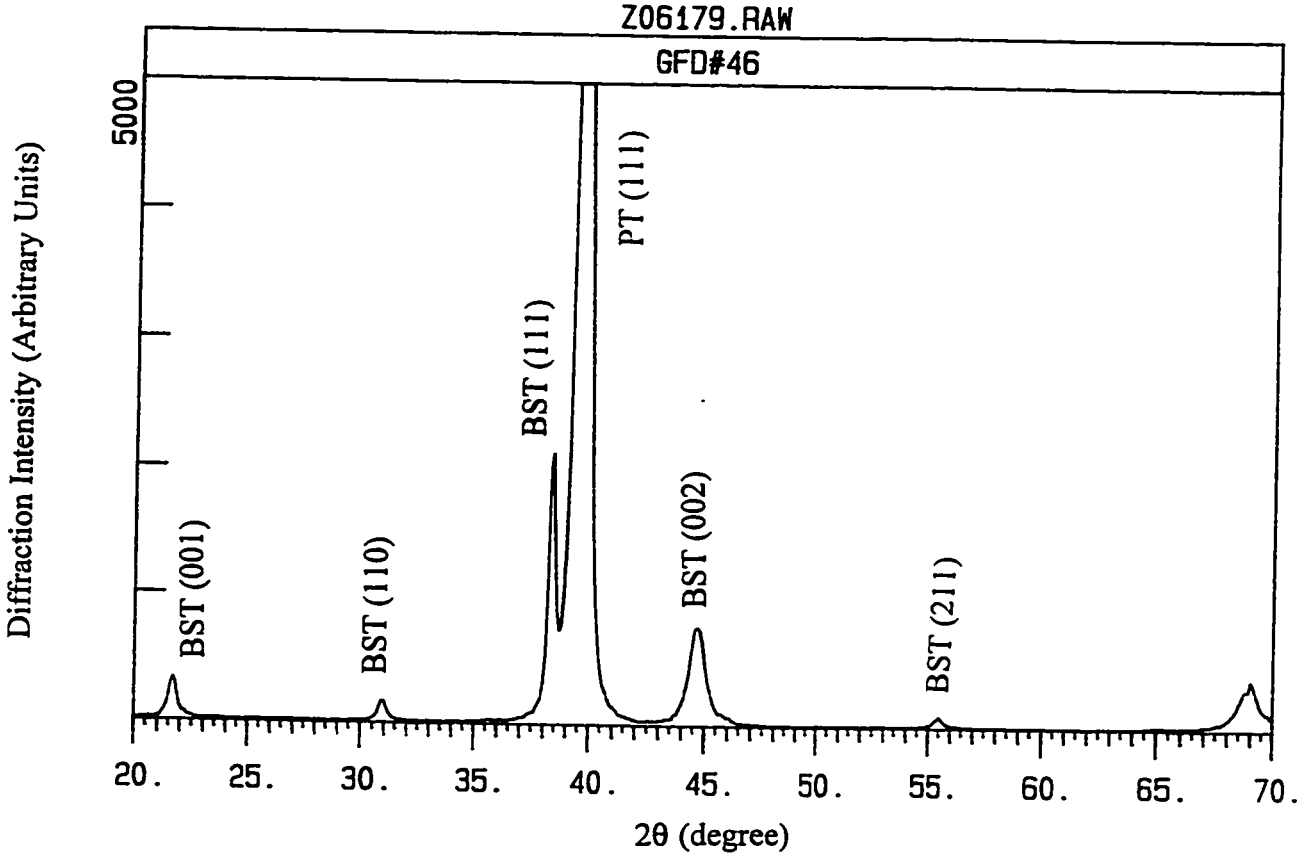

Fig. 2.3.2.1 The x-ray diffraction of the graded down film.

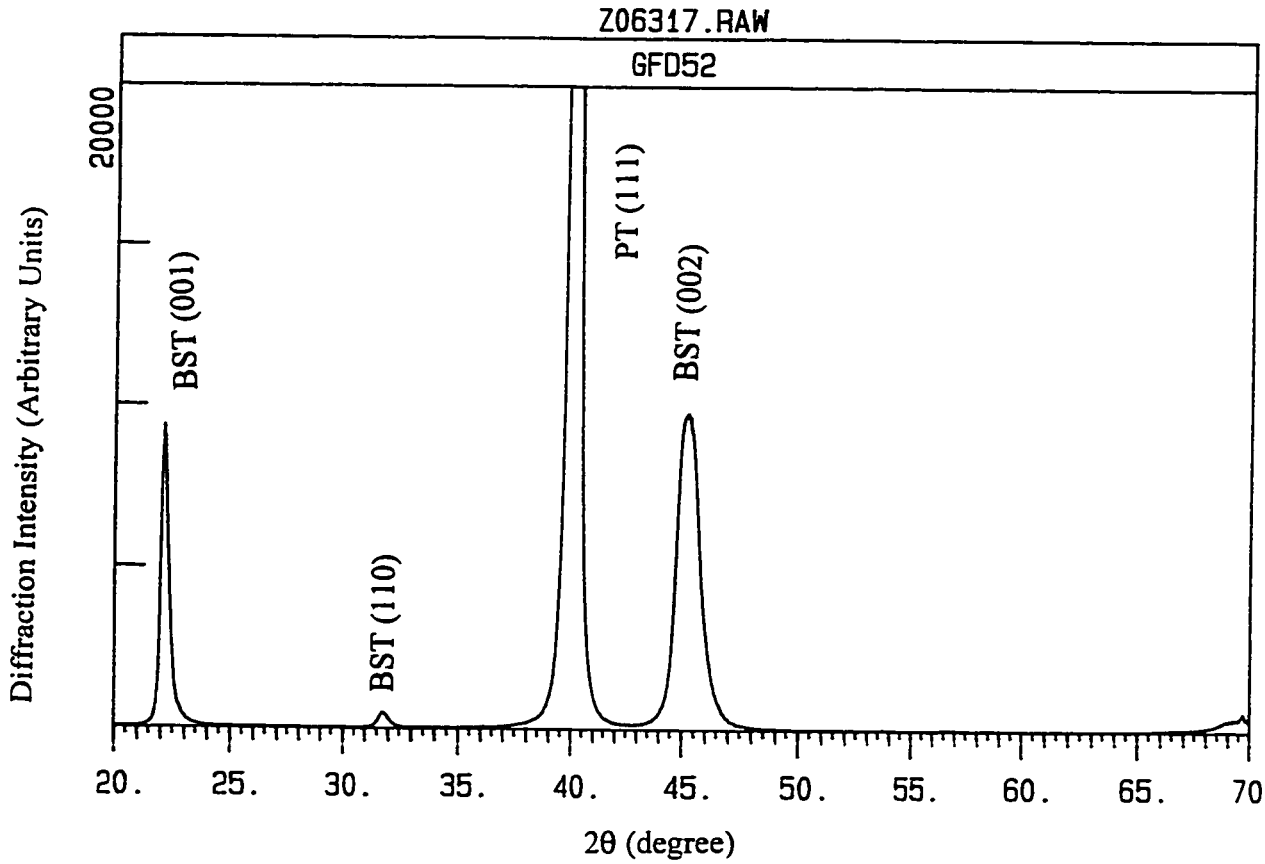

Fig. 2.3.2.2. The x-ray diffraction of the graded up film.

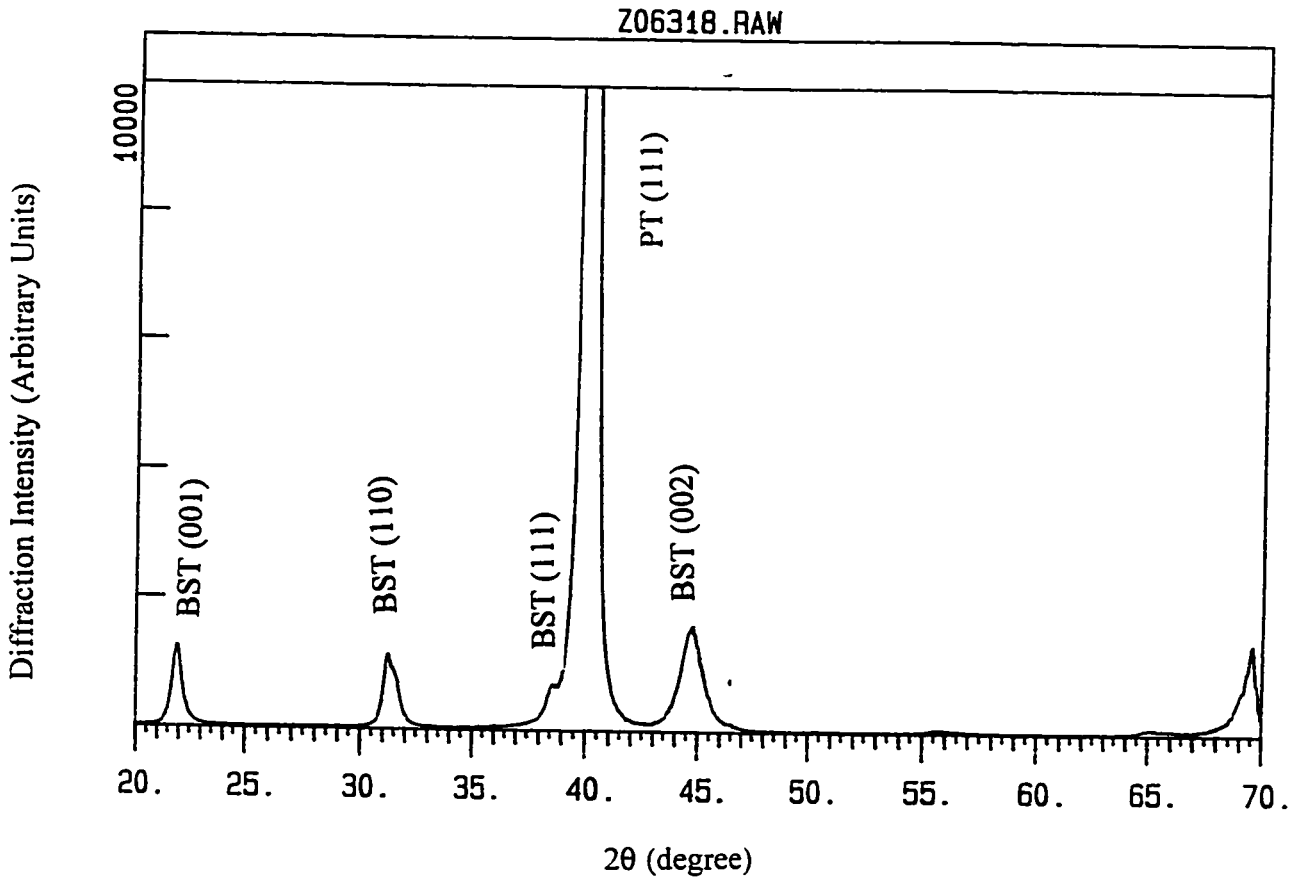

Fig. 2.3.2.3. The x-ray diffraction of the homogenous film

oriented along the (001) direction. The homogenous BST films appeared to be more randomly orientated, as no dominant diffraction peaks were observed. The d spaces for these diffraction lines were calculated from their positions in θ-2θ scans using Bragg law:

$$\lambda = 2d \sin\theta \qquad (4.3.1)$$

where λ is the Cu k_α line and equals 1.5412 Å , for the tetragonal structure[74]:

$$\frac{1}{d^2} = \frac{h^2 + k^2}{a^2} + \frac{l^2}{c^2} \qquad (4.3.2)$$

where a and c are the lattice parameters, and h, k, and l are Miller indices. Using these formulas, the lattice parameters a and c were obtained from the positions of the multi-diffraction lines, and the c/a ratios were calculated. The results were summarized in Tab.2.3.2.1. The c/a ratios were larger than 1 for the films, indicating that the films were of tetragonal structure or in a ferroelectric phase. There were some interesting tendencies in the change of c/a ratio and lattice parameters a, and c worth noting: the c/a ratio for the graded (down) film was the highest, and that for the graded (up) film was the lowest. The homogenous film was in between the two. The lattice parameter, c, for the films was elongated, the graded (down) film had the highest c, the graded (up) had the lowest c, and the homogenous film was in between the two. The elongation of the lattice parameter, c was observed by other research groups. Such elongation were believed to be caused by the strain induced by thermal and lattice mismatch between the substrate and the film, and by the epitaxial growth effect.[54, 58, 75]

The x-ray diffraction results indicate that the films were strained. This was further verified by wafer bow measurements. Wafer bows were measured before and after film

Table 2.3.2.1. Summary of x-ray diffraction results.

Lattice parameters	Tetragonal $BaTiO_3$ standard	Graded BST thin film (down)	Homogenous BST thin film	Graded BST thin film (up)
a, b (Å)	3.990	3.965	3.972	3.977
c (Å)	4.036	4.075	4.039	4.003
c/a	1.012	1.028	1.017	1.007
Film orientation		Mostly (111)	(111), (001) & (011)	Mostly (001)

verified by wafer bow measurements. Wafer bows were measured before and after film depositions. The results for graded (down), graded (up), and homogenous BST thin films are shown in Fig.2.3.2.4, Fig.2.3.2.5, and Fig.2.3.2.6, respectively. The results show that all the films were in tensile stress.

2.3.3. SEM micrographs and AFM images

Figure 2.3.3.1, Fig. 2.3.3.2 and Fig. 2.3.3.3 are the SEM micrographs for the graded down and up films, and the homogenous film respectively. They show the surface topology as well as the microstructure of the films. All three films, as shown, were polycrystalline, and crack-free. The AFM images of the films, which are shown in Fig.2.3.3.4, Fig.2.3.3.5, and Fig.2.3.3.6 also revealed the surface morphology of the films. AFM and SEM results were consistent with each other. From AFM and SEM images, the grain size of the films were estimated, and all three films showed a grain size in the submicron range near the films' surface.

2.3.4. Ferroelectric hysteresis loops

Ferroelectric hysteresis loops were observed for the graded BST films and the homogeneous BST film, indicating that the films had ferroelectric phases. This was consistent with the x-ray diffraction results, where the value of the c/a ratio revealed a tetragonal structure for the films. The hysteresis loops of the films are shown in Fig.2.3.4.1. Bulk barium titanate ($BaTiO_3$) undergoes a phase transition from tetragonal (ferroelectric) to cubic (paraelectric) at about 120 °C, and strontium titanate ($SrTiO_3$) at

Before deposition

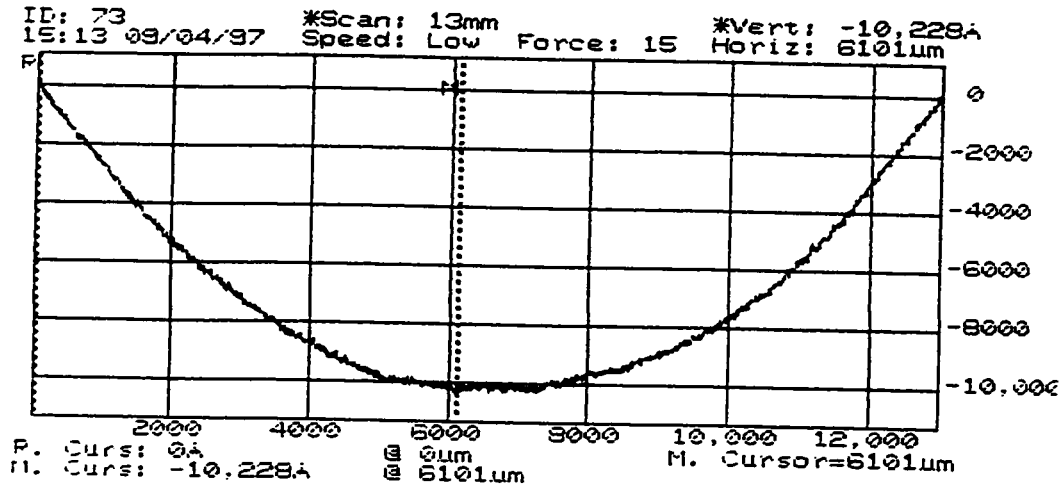

Sloan DEKTAK 3030 Rev. 1.5/1.9

After deposition

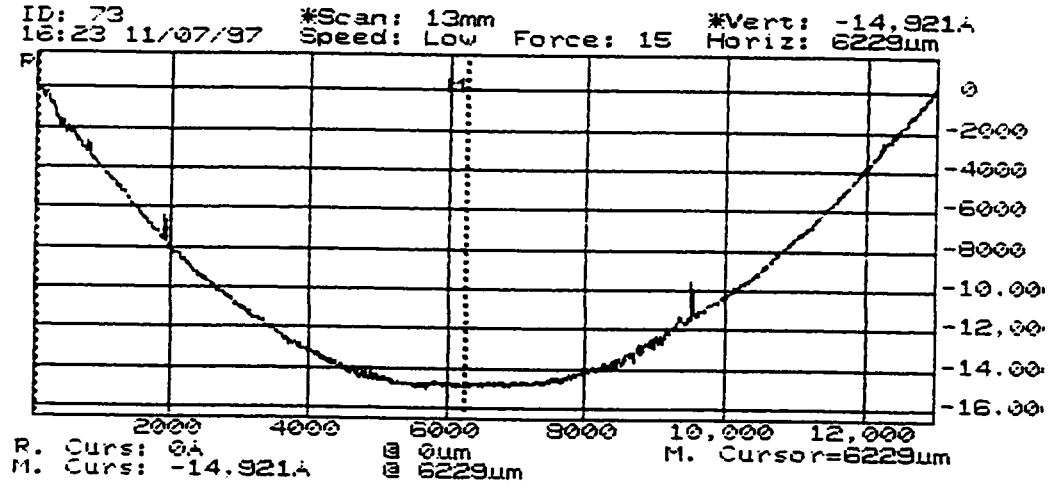

Sloan DEKTAK 3030 Rev. 1.5/1.9

Fig. 2.3.2.4 The wafer bows before and after the deposition of the graded down film.

Before deposition

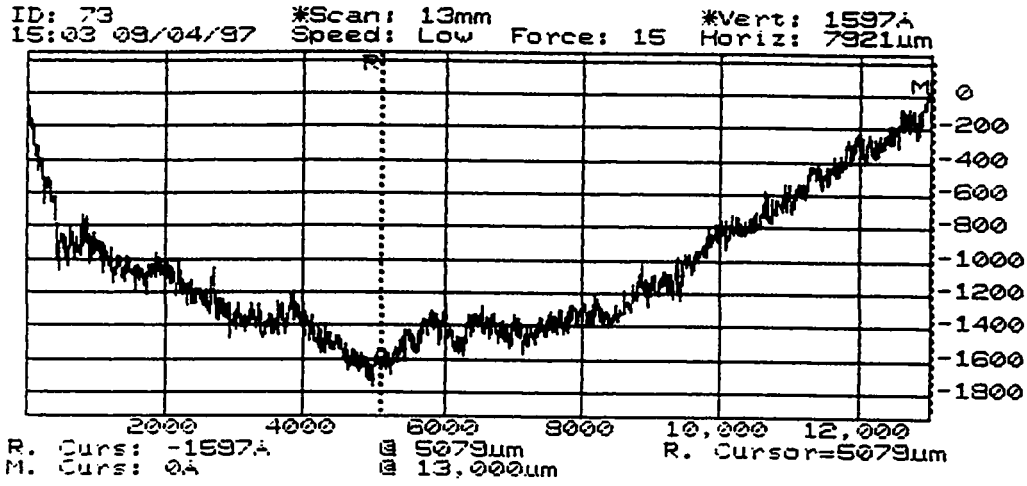

Sloan DEKTAK 3030 Rev. 1.5/1.9

After deposition

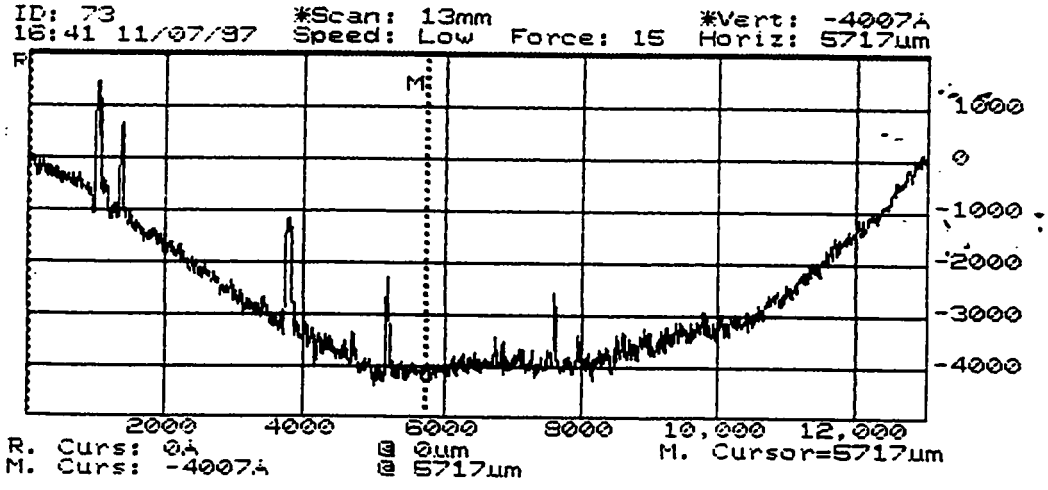

Sloan DEKTAK 3030 Rev. 1.5/1.9

Fig. 2.3.2.5. The wafer bows before and after the deposition of the graded up film.

Before deposition

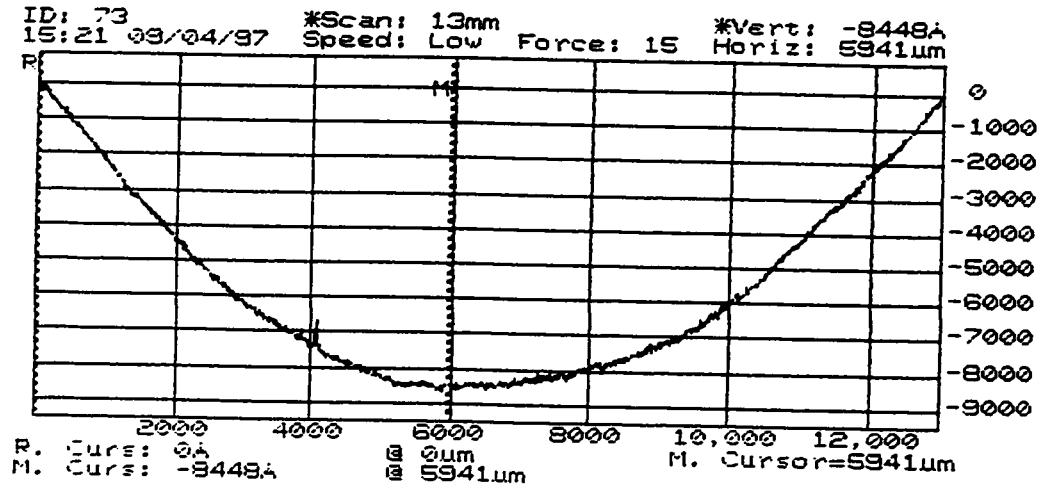

Sloan DEKTAK 3030 Rev. 1.5/1.9

After deposition

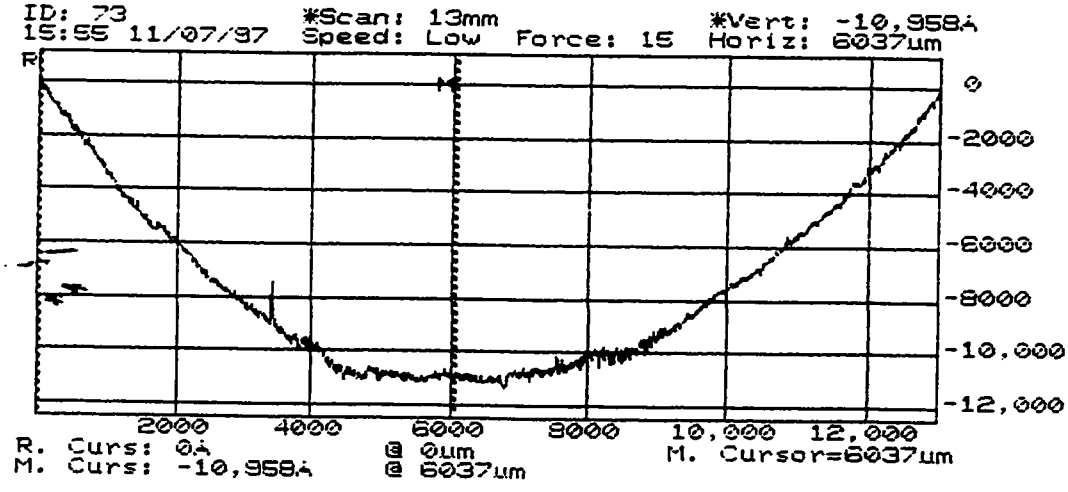

Sloan DEKTAK 3030 Rev. 1.5/1.9

Fig. 2.3.2.6. The wafer bows before and after the deposition of the homogenous film.

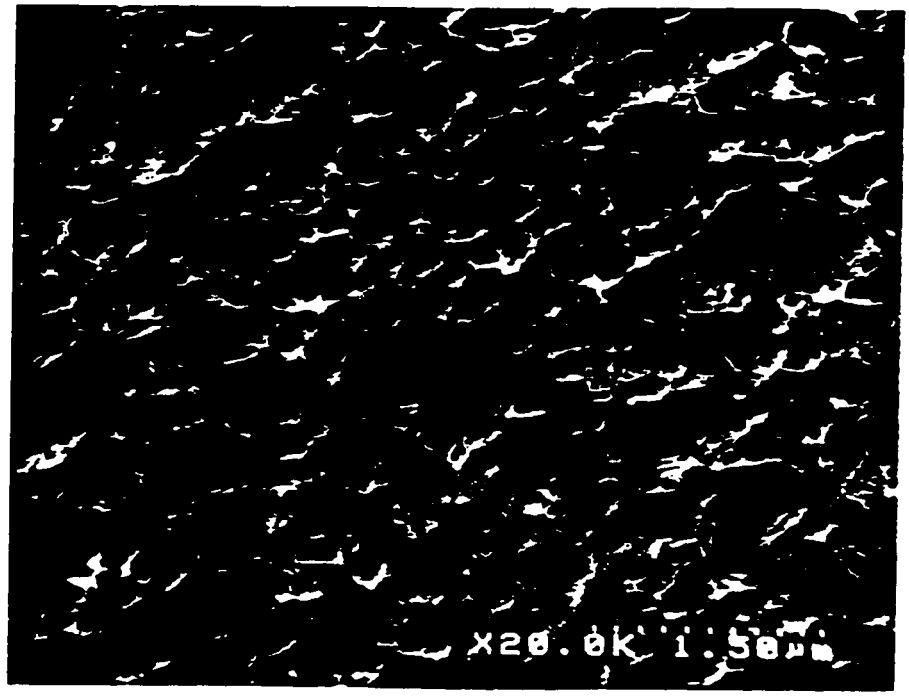

Fig. 2.3.3.1 The SEM micrograph of the graded down film.

Fig. 2.3.3.2 The SEM micrograph of the graded up film.

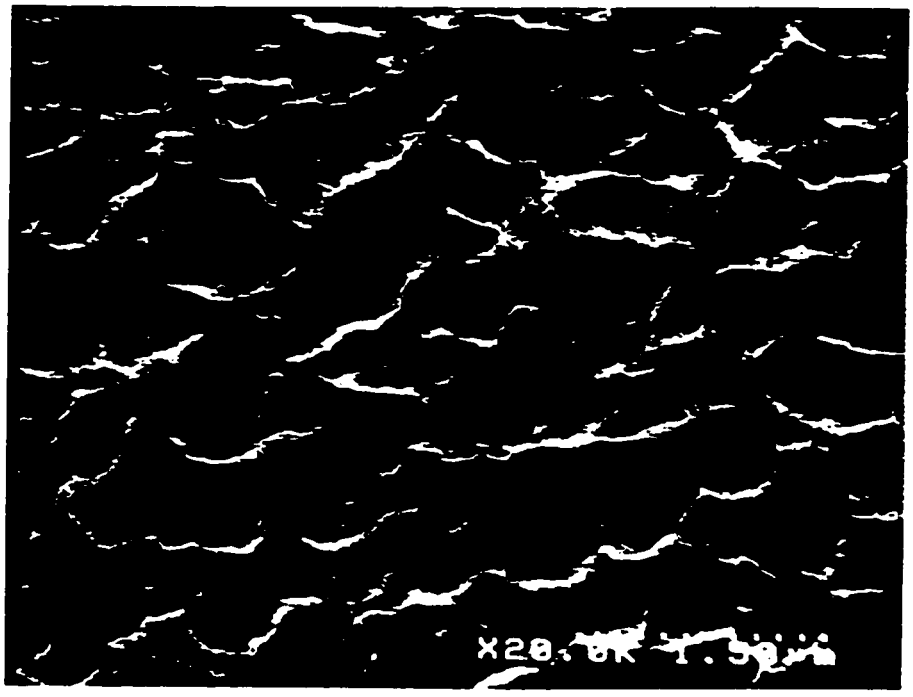

Fig. 2.3.3.3. The SEM micrograph of the homogenous film

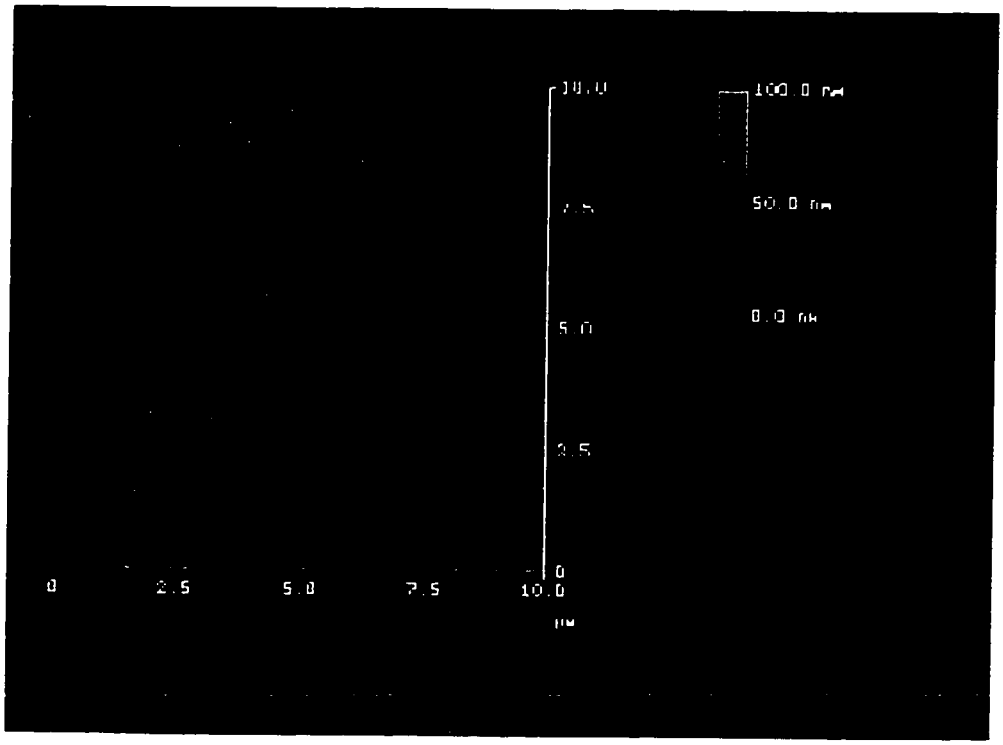

Fig. 2.3.3.4 The AFM image of the graded down film.

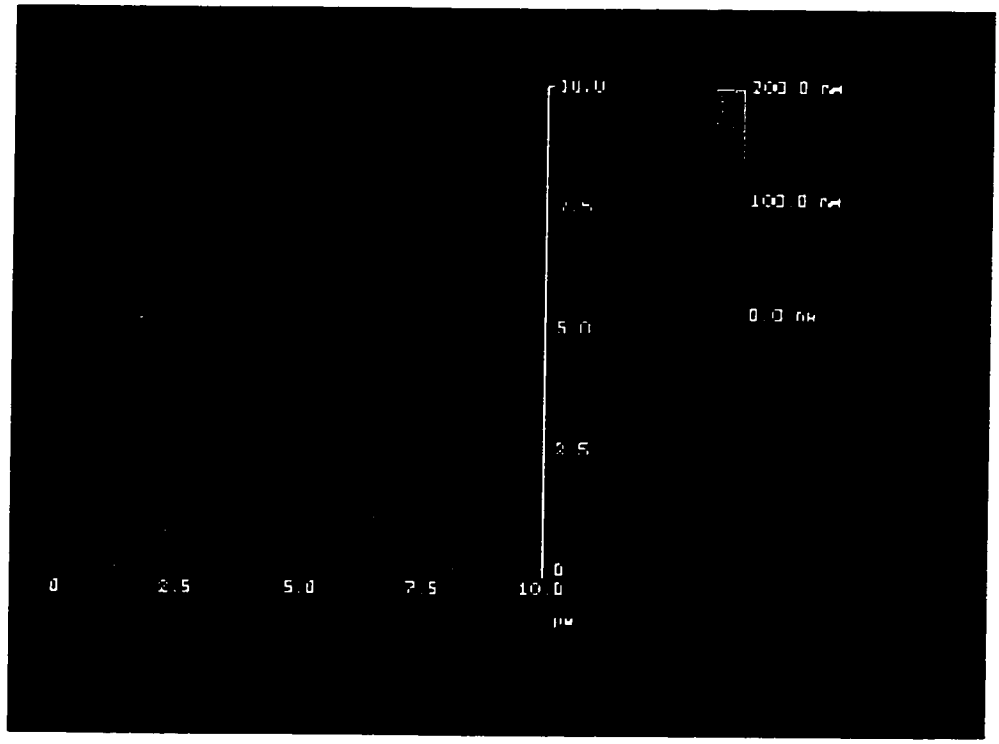

Fig. 2.3.3.5 The AFM image of the graded up film.

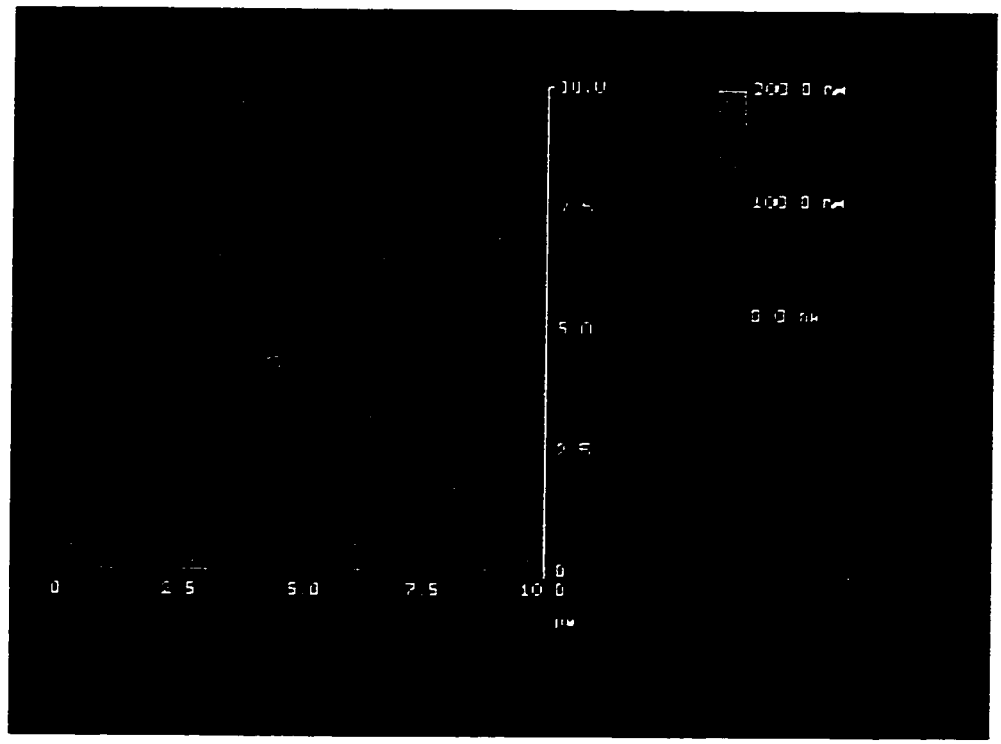

Fig. 2.3.3.6 The AFM image of the homogenous film

($SrTiO_3$) at about -200 °C. The phase transition temperature for barium strontium titanate solid solutions vary as the Ba/Sr ratio varies. In particular, $Ba_{0.7}Sr_{0.3}TiO_3$ has a phase transition temperature at around room temperature. However, in this study, all the films exhibited ferroelectric phase at wide temperature ranges, even at temperatures as high as 200 °C. The higher phase transition temperatures for thin films were observed by other groups as well.[54, 58, 75, 76] The interpretation given was that the strain helped stabilize the ferroelectric phase. We also believe that it was the strain in the films that made the ferroelectric phase persistent, well above the bulk phase transition temperature. The hysteresis loops of the films were generally narrow, which is typical for thin films. The homogenous BST film had relatively wider loops compared to graded films, as shown in Fig. 2.3.4.1.

2.3.5. Dielectric properties of the films

The relative permittivity (dielectric constant) of the graded BST films and the homogenous BST film at various temperatures is shown in Fig. 2.3.5.1. The permittivity of the compositional graded films (both up and down) increased slightly as the temperature changed from -20 °C to 100 °C. The permittivity of the graded films was about 140, which was relatively low compared to that normally observed in BST films.[36, 45, 64] This was probably because the films grown in this study were thinner (2000 Å) than the others. The permittivity of the homogenous film was a little higher than the graded films, as shown in Fig. 2.3.5.1. It decreased slightly as the temperature changed from -20 °C to 100 °C. The permittivity vs. temperature curves for all three films were

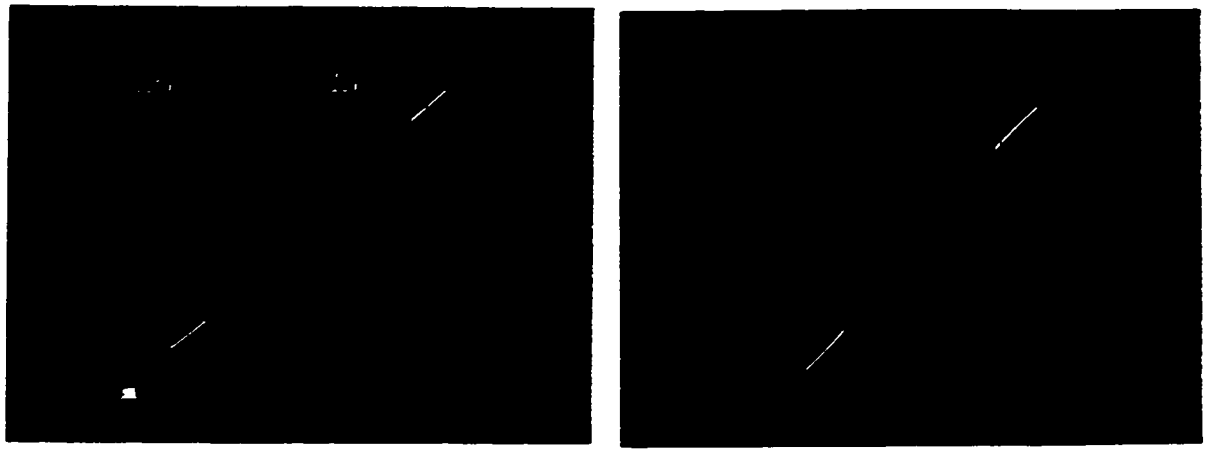

(a) (b)

(c)

Fig. 2.3.4.1. The hysteresis loops of the films. a) Graded down film. b) Graded up film. c) Homogenous film.

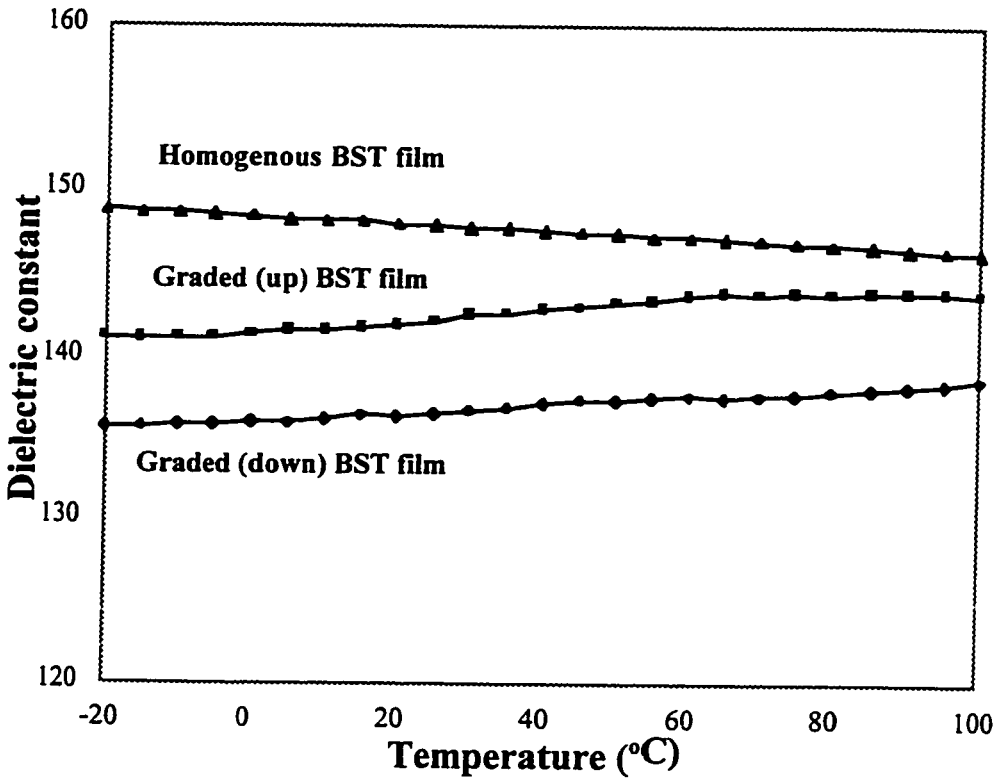

Fig. 2.3.5.1. The dielectric constants of the films at various temperatures. a) Graded down film. b) Graded up film. c) Homogenous film

relatively flat and showed no dramatic changes. No phase transition was observed in the temperature range from -20 °C to 100 °C. Figure 2.3.5.2 is a plot of the dissipation factors (tan δ) versus temperature for the graded (both up and down) films and the homogenous BST films. The dissipation factors of the films were relatively small (varying from 0.009 to 0.017). All three dissipation factor vs. temperature curves were similar, as shown in Fig.2.3.5.2, and the dissipation factors for the films increased with increasing temperature.

2.4 CONCLUSION

A new fabrication method of compositional graded ferroelectric films has been developed. This method, rf magnetron sputtering, is a silicon compatible fabrication method, and has greater control compared to the previously used GFD fabrication methods (MOD). Graded ferroelectric BST thin films with uniform compositional gradients were fabricated using this method at relatively low temperatures (500 °C). Also, we have characterized the structure and properties of the graded and homogenous BST thin films with various techniques. The films were polycrystalline, the homogenous BST thin films appeared to be randomly oriented while the graded films were partially oriented. The orientations of the films were dependent on the directions of the gradient. The films were strained, and the lattice parameter, c, was elongated. The films were dense and free of cracks. The grain size of the films was in submicron region. The films were in the ferroelectric phase at room temperature and at temperatures well above 120 °C, the

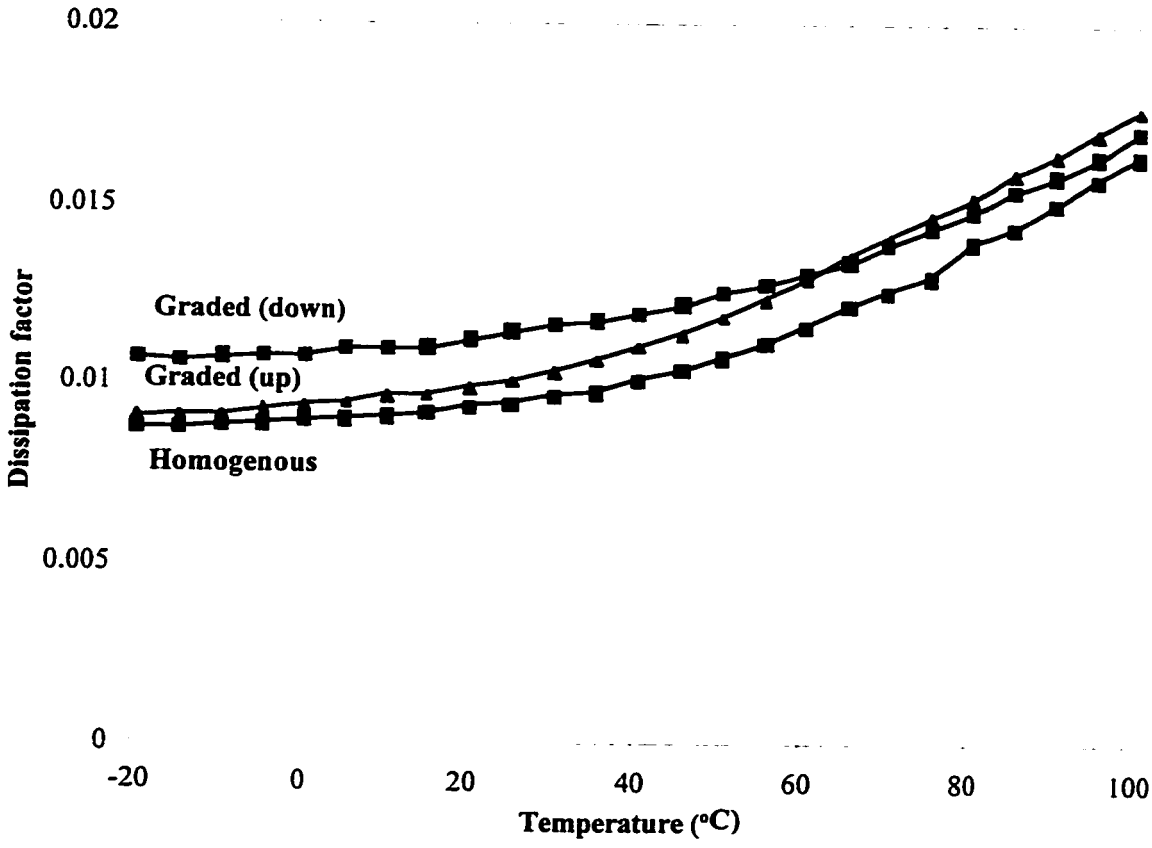

Fig. 2.3.5.2 The dissipation factors of the films at various temperatures. a) Graded down film. b) Graded up film. c) Homogenous film.

phase transition temperature for bulk barium titanate. The dielectric constant of the films was insensitive to temperature, and was lower than normally observed for BST thin films, as the films in this study were very thin. The dielectric loss of the films was low, and increased with temperature.

CHAPTER III

GIANT EFFECTIVE PYROELECTRIC COEFFICIENTS FROM GRADED FERROELECTRIC DEVICES

This chapter presents the most important property of graded ferroelectric devices, giant effective pyroelectric coefficients. Giant effective pyroelectric coefficients as large as 5 $\mu C/cm^2$-°C, with peak responsivity at approximately 50 °C, were obtained from $Ba_{1-x}Sr_xTiO_3$ graded ferroelectric devices (GFD). The 0.2 μm compositional graded structures were formed on platinum coated silicon substrates at 500 °C using magnetron sputtering and had a compositional variation of x = 0 to x = 0.3 normal to the growth surface.

3.1 INTRODUCTION

The most sensitive pyroelectric infrared detectors available to the date are hybrid structures made from ferroelectric ceramics or single crystals of $Ba_{1-x}Sr_xTiO_3$ (BST), which have pyroelectric coefficients as large as 23 $\mu C/cm^2$-°C.[38, 39] Unfortunately, because such structures are fashioned from bulk ferroelectric materials rather than thin films, the device yield is often quite low, resulting in high fabrication costs. Therefore, efforts have been devoted to developing monolithic pyroelectric thin film detectors.[40, 41, 42, 43] However, compared to bulk ceramics, thin film materials almost universally have severely reduced pyroelectric coefficients. In particular, it is usually observed that ferroelectric thin films have pyroelectric coefficients on the order of 0.05 $\mu C/cm^2$-°C,[45]

which is almost three orders of magnitude smaller than the best bulk ceramic materials. Thus, while modern thin film processing techniques offer the means for low cost fabrication of focal plane arrays, these materials presently do not possess the necessary thermal response to achieve high performance devices.

Compositional graded ferroelectric films, however, demonstrated giant effective pyroelectric coefficients.[48, 49, 50] Prior graded ferroelectric devices have been fabricated by the metallo-organic decomposition (MOD) method.[48, 49] In this study, rf magnetron sputter deposition was adopted to fabricate compositional graded BST ferroelectric thin film structures. The films formed exhibited a large field and a temperature dependent offset in hysteresis loops when under strong field excitation. Giant effective pyroelectric coefficients with a peak value of 5 μC/cm2-°C were obtained at 50 °C, a value nearly two orders of magnitude higher than the pyroelectric coefficients commonly observed in conventional BST thin films.

3.2 EXPERIMENTAL

Magnetron sputtering was used to deposit the graded BST thin films. The BST graded ferroelectric devices formed in this study consist of (as shown in Fig. 2.3.1.1) : a bottom Pt/Ti electrode deposited on an oxidized silicon substrate; a BST thin film with a continuous composition change from $BaTiO_3$ to $Ba_{0.7}Sr_{0.3}TiO_3$; and top Au/Cr electrodes. Details of the deposition process is given in chapter 2.

As discussed in chapter 2, various techniques, such as XPS, x-ray diffraction, SEM,

AFM, dielectric measurements, and wafer bow measurement, were used to characterize the structure and properties of the films.

3.3 BASIC STRUCTURE AND ELECTRIC PROPERTIES OF THE FILMS

As discussed in detail in chapter 2, the films formed had a polycrystalline structure and were strained. The films had grain sizes mostly in the submicron range, were dense and relatively free of cracks and pin holes. The dissipation factor of the films was low and showed a slight temperature dependence varying from 0.01 to 0.017 as the temperature was increased from -20 °C to 100 °C. The permittivity of the graded films increased slightly from 136 to 138 as the temperature was increased from -20 °C to 100 °C. No dramatic changes in permittivity due to phase transformations were observed. The films were in the ferroelectric phase as evidenced by the hysteresis loops observed.

3.4 GIANT PYROELECTRIC COEFFICIENTS

Ferroelectric hysteresis loops of the films were narrow, as shown in Fig. 2.3.4.1 in chapter 2. The D-E hysteresis loops of the films showed a large field and a strong temperature dependent vertical shift along the displacement axis, ΔD, when excited with a periodic electric field, as shown in Fig. 3.4.1 and Fig.3.4.2.

The field dependent offset, ΔD, as shown in Fig.3.4.1, increased in absolute magnitude as the excitation field was increased. The offset never saturated before the films electrically broke down. The offset ΔD was also strongly temperature dependent.

Small temperature perturbations created noticeable variances in the positions of the ferroelectric hysteresis loops of the graded BST films. An effective pyroelectric coefficient,[48, 49, 50] has been defined for GFD's as: [48, 49, 50]

$$p_{eff} \equiv \frac{d(\Delta D)}{d(\Delta T)} \qquad (3.4.1)$$

Fig. 3.4.2b shows the hysteresis loops of the graded BST film at various temperatures. The hysteresis loops appear as single lines in this figure because the vertical gain of the scope has been reduced in order to show the large translations, ΔD. The effective pyroelectric coefficients of the films at temperatures from -20 °C to 120 °C were calculated as a derivative of the shift with temperature and is plotted in Fig. 3.4.3. The maximum value of the effective pyroelectric coefficient was approximately 5 $\mu C/cm^2$ -°C at 50 °C. This is a value more than two orders of magnitude greater than the conventional pyroelectric coefficients observed in BST thin films and close to the highest pyroelectric coefficients ever obtained.[38]

The effective pyroelectric coefficients of the devices were often not monotonic functions of temperature as indicated in Fig. 3.4.4. Multiple devices were examined and all showed a primary peak in p_{eff} around 50 °C, though some showed a secondary peak at approximately 80 °C. Such complexity in p_{eff} with temperatures is not totally surprising. Both the polarization and Curie temperature of ferroelectric materials are well- known to be highly sensitive to both composition and strain, it follows that even small variations in any of these quantities (in our highly graded devices) could easily add to the functional complexity of p_{eff}. More discussion about the temperature dependency of

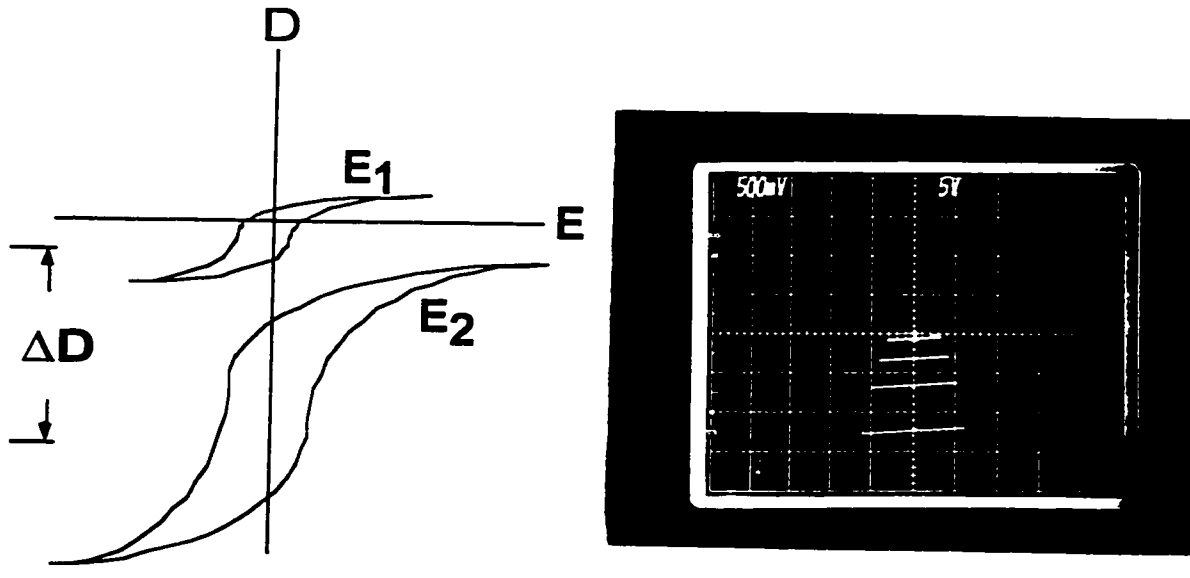

(a) (b)

Fig. 3.4.1 The field dependent offset of the hysteresis loops observed.

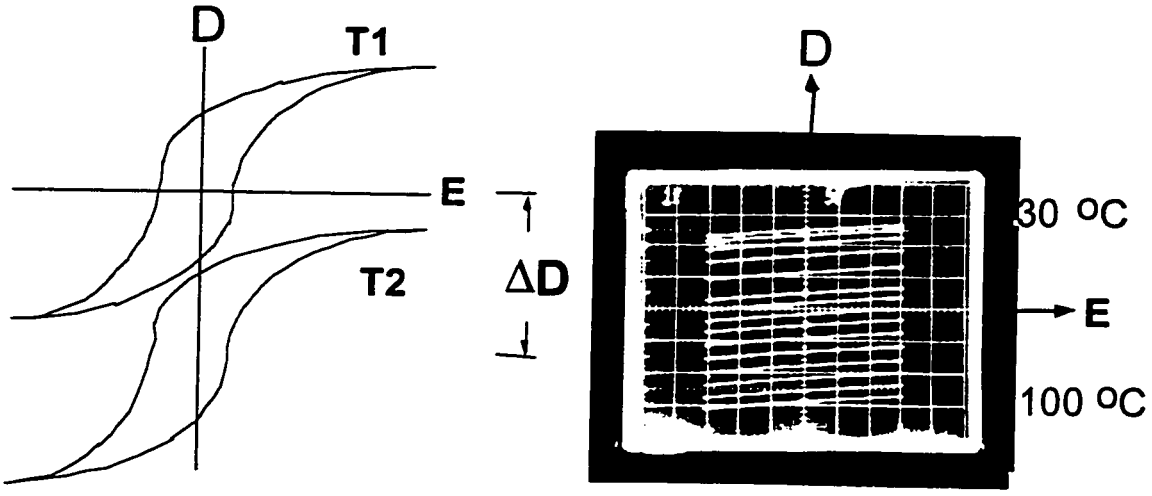

Fig. 3.4.2 The temperature dependent offset of the hysteresis loops observed.

effective pyroelectric coefficients will be given in chapter 4.

Variations in wave form, such as sine wave or triangular wave, of the periodic excitation electric field over a wide range of frequencies (50 Hz to 100 KHz) resulted in shifts of the hysteresis loops which were relatively insensitive to excitation frequency.

The pyroelectric response, p_{eff}, depended not only on the temperature change of the film, but also on the exciting electric field - the " pumping force" applied to the film. The stronger the exciting electric field the larger the effective pyroelectric coefficient, p_{eff}. Fig. 3.4.3 was obtained when the film was under an excitation electric field of 30 V_{pp}. By improving the break-down strength of the films (i.e., further reduction of structural defects in the films), even higher pyroelectric coefficients of graded ferroelectric BST thin films should be obtainable.

The excitation field was the only dominant factor that determined the effective pyroelectric coefficients of the films. The effective pyroelectric coefficients of the films were largely dependent on the maximum field that could be applied (electrical breakdown strength of the films). All other factors affecting pyroelectric coefficients were minors compared to the exciting field. Graded BST films with different gradients were examined. as anticipated the D-E hysteresis loops of these films all showed large field, and temperature dependent vertical shifts along the displacement axis, ΔD, when excited with a periodic electric field. However, the values of effective pyroelectric coefficients from different films highly fluctuated. No clear correlation between the effective pyroelectric coefficients and the compositional gradients could be determined from those highly

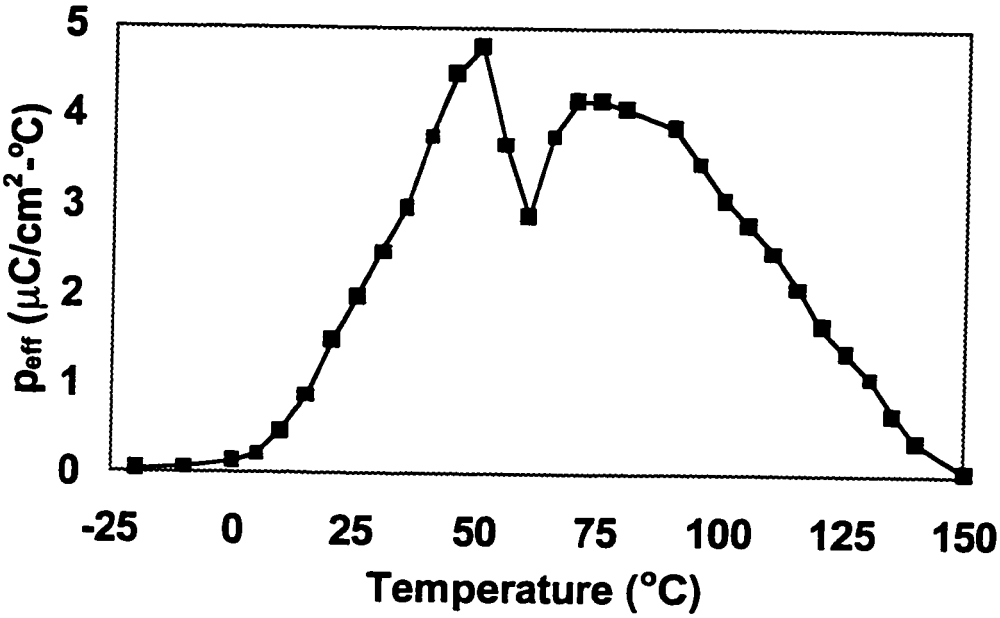

Fig. 3.4.3 Effective pyroelectric coefficients Vs. temperatures for the graded film.

fluctuated results. This suggests that the compositional gradients, compared to the exciting field, was not the key factor in determining the effective pyroelectric coefficients of the graded films.

3.5 COMPARISON OF CONVENTIONAL AND NEW PYROELECTRIC DETECTORS

We have graded ferroelectric devices exhibiting giant pyroelectric coefficients more than two orders of magnitude larger than that from conventional homogenous ferroelectric thin films. Highly sensitive pyroelectric infrared detectors can be fabricated base on this innovative structure. As illustrated in Fig. 3.5.1, unlike the conventional pyroelectric detectors, the operation of the new pyroelectric detectors would depend on detecting the temperature dependent offset of the D-E hysteresis loops, ΔD. Therefore, the detectors would have superior performance in terms of sensitivity as compared to conventional pyroelectric infrared detectors.

3.6 CONCLUSION

We have shown that the graded ferroelectric BST thin films, which were fabricated using the silicon compatible rf magnetron sputtering method, exhibited giant pyroelectric coefficients two orders of magnitude higher than that of the conventional homogenous ferroelectric BST thin films. This effective pyroelectric coefficient was also highly dependent on the exciting field applied. Therefore, by improving the breakdown strength of the films, higher excitation fields could be applied, and even higher pyroelectric

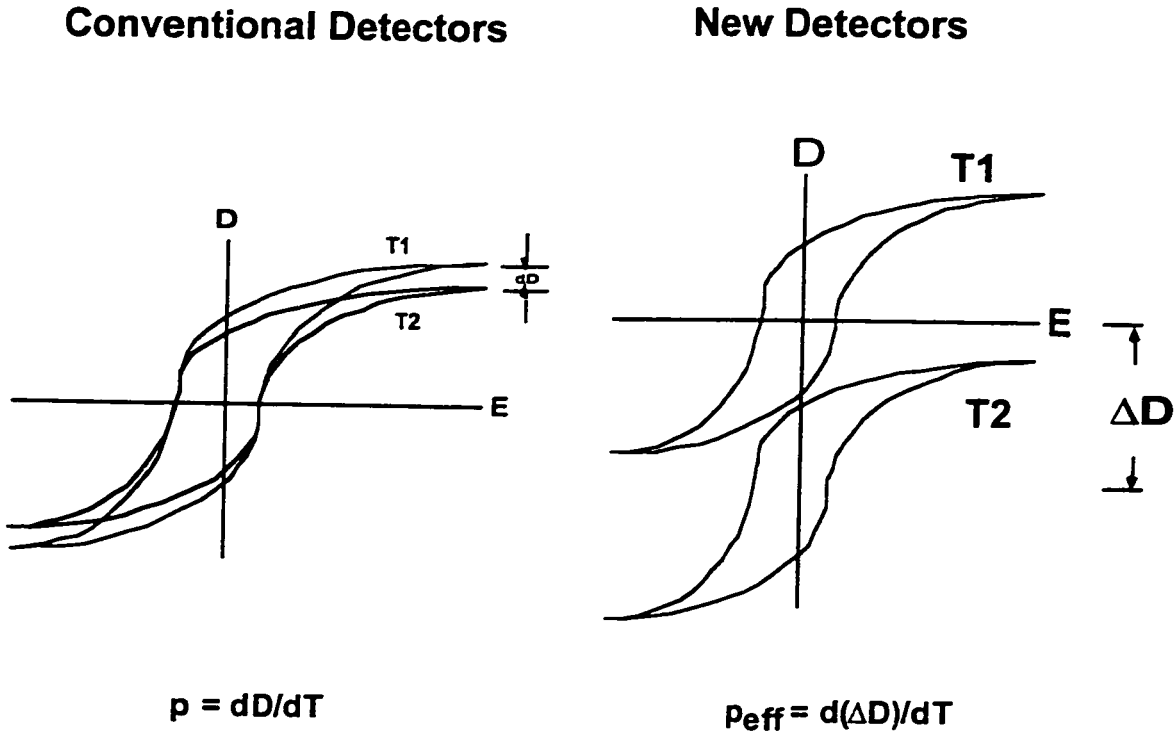

Fig. 3.5.1 Comparison of the detecting method between conventional pyroelectric detectors and the new type of pyroelectric detectors

coefficients of graded ferroelectric BST thin films could be obtainable. The giant effective pyroelectric coefficients obtained from graded ferroelectric devices opens the way for fabricating a new type of high sensitive pyroelectric infrared detector.

CHAPTER IV

A PHENOMENOLOGICAL MODEL FOR GRADED FERROELECTRIC DEVICES

In this chapter, we present a phenomenological model for graded ferroelectric devices (GFD's). This model qualitatively explains all of the new phenomena associated with graded ferroelectric devices namely: i) a dc offset in ferroelectric D-E hysteresis loops when excited with a strong periodic electric field, and the field dependency of this offset; ii) a threshold exciting field required in creating the offset of the hysteresis loops; iii) the temperature dependency of the offset of the hysteresis loops. The model suggests that the strain built in the films, which altered the symmetrical nature of ferroelectric thin films, was the fundamental reason for the new pyroelectric effects. The strain built in the films were introduced by compositional gradients in the films and by lattice and thermal mismatches between the substrates and the films. The model also predicts some new experimental results.

4.1 INTRODUCTION

The pyroelectric response of ferroelectric thin films has been improved dramatically in a recently invented innovative structure, compositional graded ferroelectric thin film devices.[48, 49, 50] The graded ferroelectric thin film structures are interesting not only because of their potential application in infrared detectors, but also because of their fundamental theoretical importance - as the charge pumping effect observed in graded ferroelectric devices is essentially a new pyroelectric phenomenon. In this chapter, we

explore the basic physics of graded ferroelectric devices. Based on existing experimental evidences, a phenomenological model for graded ferroelectric devices (GFD's) was proposed. This model explains how strain in the films, introduced by compositional gradients and by lattice and thermal mismatch between the substrates and the films, alters the symmetrical nature of the ferroelectric thin films and caused the new pyroelectric effects. New experiments were designed and carried out to support the model.

4.2 EXPERIMENTAL EVIDENCE

The graded and homogenous ferroelectric BST thin films in this study were deposited on platinum coated silicon substrates using rf magnetron sputtering. Prior to this study, graded BST thin films were deposited on platinum foils using metallo-organic decomposition (MOD) method.[49]

New pyroelectric phenomena were observed from the graded films deposited by both methods. When the graded films were excited with a strong periodic electric field, and after the magnitude of the exciting field exceed a critical threshold field, E_{th}, a dc voltage was induced across the graded films, and the displacement (D)-electric vs. field (E) ferroelectric hysteresis loops showed large unidirectional shifts along the displacement axis.[48, 49] The dc offset of the hysteresis loops of the graded films was a function of the excitation field, and increased with the field, never saturated before the films were electrically broken down. This effect is illustrated in Fig. 4.2.1a. The dc offset of the hysteresis loops were also highly sensitive to temperature change. Small perturbations in temperature created noticeable shifts in the hysteresis loops and made this effect useful in

pyroelectric infrared detection. The temperature dependency of the dc offset in the hysteresis loops is illustrated in Fig. 4.2.1b. The basic characteristics of the new pyroelectric effects, or the dc offset of the hysteresis loops when excited with a periodic electric field, can be summarized as following:

- The offset starts when the exciting field exceeds a threshold value, E_{th}.
- The offset is field dependent and increases with the periodic exciting periodic field.
- The offset is highly temperature dependent and can be used to detect temperature change due to infrared radiation.

More experimental results came from the study of the direction of the offset. It was demonstrated from the MOD grown films on platinum foils that the direction of the offsets was dependent on the direction of the compositional gradients. Both up and down offsets of the hysteresis loops were obtained from gradient up and gradient down MOD grown graded films, respectively. This indicates that the compositional gradient the film was the cause of the offsets. However, the results from the graded films deposited on platinum coated silicon substrates using sputtering in this study were quite different. For both gradient up and gradient down sputtered graded films, the direction of the offsets of the hysteresis loops remained the same (down). Furthermore, unlike the MOD homogenous films on platinum foils, the sputtered homogenous films on platinum coated silicon substrates also exhibited a down shift in the hysteresis loops. At first glance, the results from the sputtered films in this study and the previous results from the MOD deposited films appear to contradict each other. However, what they are really telling us is that there was a common origin for the offset of the hysteresis loops. Both

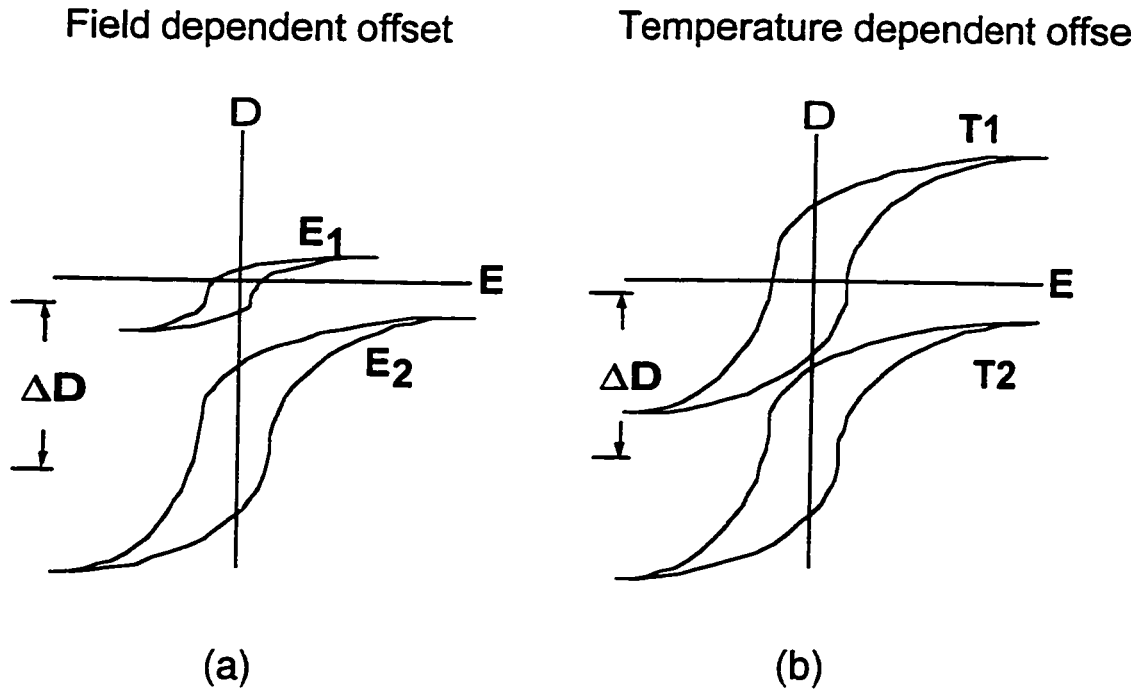

Fig. 4.2.1 Illustration of the new pyroelectric effect from the graded films - offset of hysteresis loop when excited with a periodic electric field. a) Field dependency. b) Temperature dependency

compositional gradient in the films, and substrate effect could attribute to this common phenomenon.

4.3 STRAIN INDUCED EFFECT

We now try to find the origin of this new pyroelectric effect or the induced dc voltage across the film. From a physics point of view, the existence of a dc voltage in the film in this case means that there must be a separation of the negative and the positive charges. For ferroelectric crystal thin films in particular, this could be caused by dipoles aligning together to create a macroscopic polarization in the films.

As we discussed in chapter 1, the free energy G of a ferroelectric crystal can be expressed as:

$$G=\alpha P^2+\gamma P^4+.... \qquad (4.3.1)$$

and the G-P curve (Fig. 1.3.5) is shown in Fig.4.3.1 again for convenience. The two stable polarization states in a ferroelectric crystal, P and -P, are equivalent, as shown in Fig.4.3.1 (except the direction). The direction of the polarization can be switched by a external electric field, and there is no preferred direction for dipoles to align. This is true for conventional ferroelectric thin film crystals. So now the question is: why do the graded BST thin films have a preferred polarization state for the dipoles to align at this preferred direction?

The experiments on the directions of the offset in the hysteresis loops provide important clues to the answer. As discussed earlier, the offset in the hysteresis loops

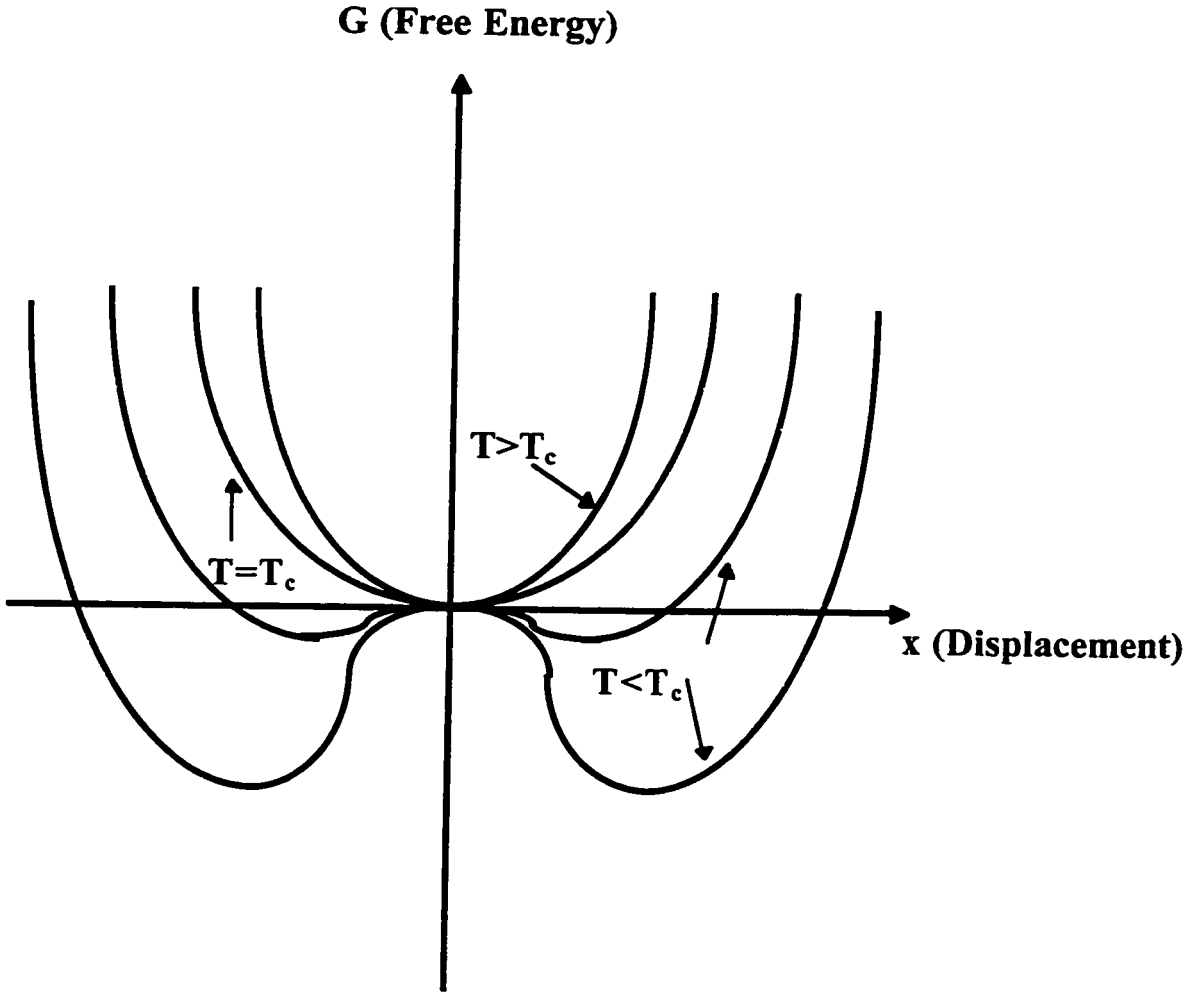

Fig. 4.3.1. Free energy of the ferroelectric materials as function of displacement of charge or polarization at various temperatures

were caused by the compositional gradient (for MOD films), and an unknown effect from the platinum coated silicon substrates had the same effect on the films as the compositional gradient (sputtered films). It is reasonable to deduce that the common origin for the offset in the hysteresis loops was the strain in the films. Strain could be introduced into the films by compositional gradient, as the Sr, and Ba have different size and $BaTiO_3$ and $SrTiO_3$ have different lattice parameters, or by thermal and lattice mismatch from the substrates. For MOD deposited films, the substrates were soft platinum foils, the films were probably relaxed and the dominant factor would be compositional gradient. The directional strain was introduced into the films by incorporating $SrTiO_3$ into $BaTiO_3$ directionally. Hence, the graded films exhibited both up and down offsets in the hysteresis loops, depending on the direction of the compositional gradient. On the other hand, for the sputtered films on platinum coated silicon substrates, strain caused by the substrates appeared to be the dominant factor and the offsets in the hysteresis loops of all the films were down.

The existence of strain was evident by x-ray diffraction results, where an elongation of the lattice parameter, c, was observed, and also by wafer bow measurement where the films were found in tensile stress. The details of these measurements and results were given in chapter 2.

Strain in the films alters the symmetrical nature of the films, which has a profound impact on their properties. For a strained film, the expression of the free energy, Eq.4.3.1, needs to be modified and an extra strain energy term should be added to the expression:

$$G = \alpha P^2 + \gamma P^4 + ... + x_i X_i \qquad (4.3.2)$$

where x_i is strain and X_i is stress. Now the G - P curve is no longer symmetrical, rather it is skewed as shown in Fig. 4.3.2. The two polarization states are also no longer equivalent. The one with lower energy is preferred and the dipoles would prefer to align at that direction to minimize the energy of the system. The direction in which the D - P double wells skew depend on the direction of the strain, as illustrated in Fig.4.3.2. For the MOD deposited films, the direction depended on the direction of the compositional gradients. For the sputtered films, the hysteresis shift was always in one direction because strain from the substrates was the dominant factor.

4.4 AN EXPLANATION FOR THE NEW PYROELECTRIC PHENOMENA

Based on the above discussions, the basic characteristics of the new pyroelectric effects, which were summarized in earlier sections, can be qualitatively understood.

The existence of a threshold value of the exciting field, E_{th}, is illustrated in Fig.4.3.2. This illustration shows that although one polarization state has lower energy than the other, there is an energy barrier between them. In order for the dipoles to overcome this energy barrier and align or occupy a lower energy polarization state, an exciting field larger than a threshold field, E_{th}, is required.

The field dependent offset in the hysteresis loops can be understood as the following. First, the ferroelectric BST thin films were polycrystalline and had multi domains oriented at various directions not always in parallel with the exciting periodic

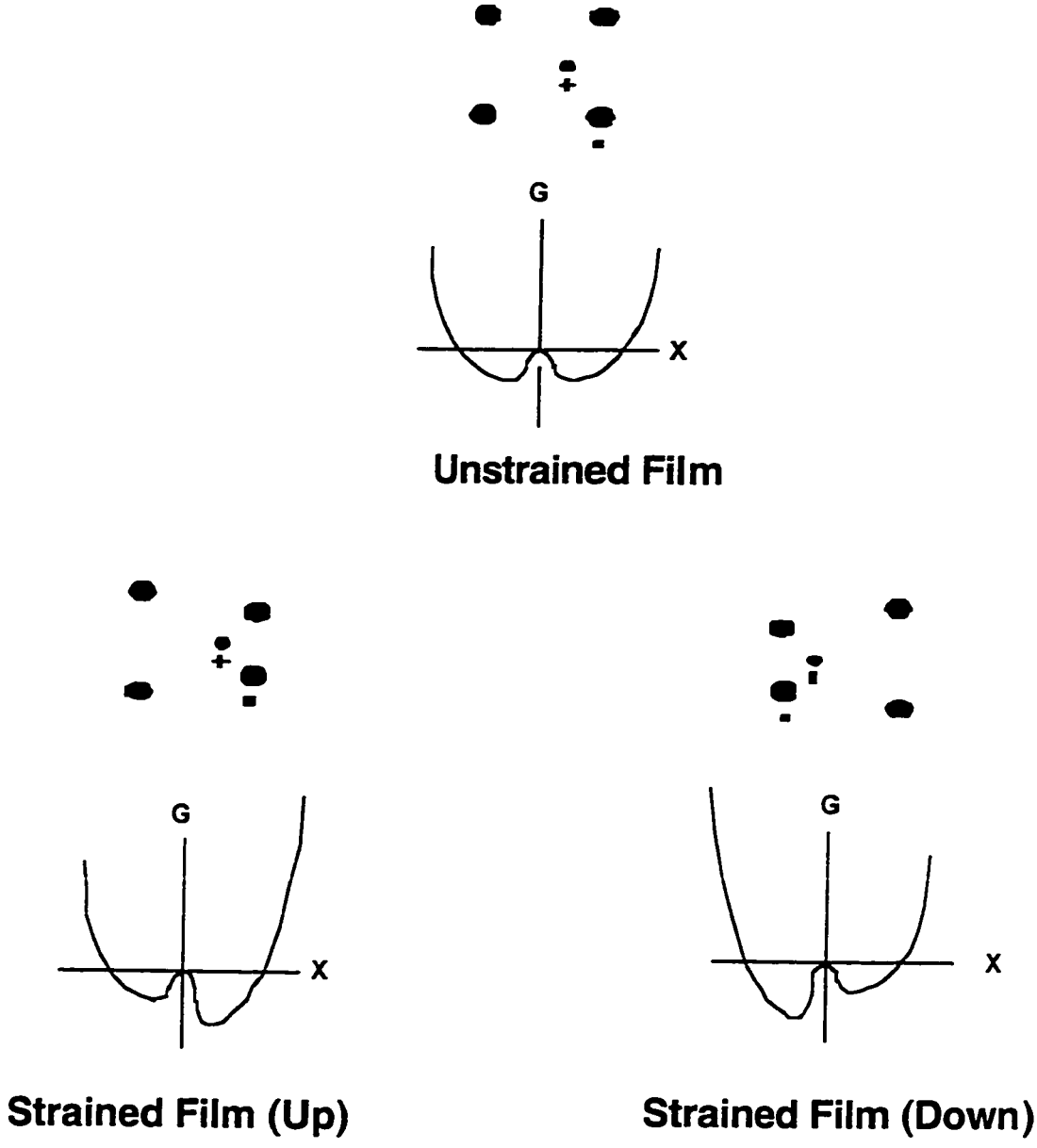

Fig. 4.3.2 Modified free energy G - polarization P double well for strained film. In MOD films, the direction of the strain is dependent on the compositional gradients, and for sputtered films, the strain is caused by substrate and is always at one direction-down.

electric field which was normal to the film's surface. Thus, when excited with a periodic electric field with a certain magnitude, only a portion of the domains experience a field stronger than the threshold field E_{th} in the crystal orientation, and the dipoles in those domains would be able to overcome the potential barrier and be aligned. Therefore, as the field increases, more and more domains will experience fields stronger than the threshold field - so more dipoles would be aligned. Second, the individual dipole, when excited with a field, would be stretched and increase in value with the exciting field. So we can write:

$$p \propto E^{\gamma} \qquad (4.4.1)$$

where p is a dipole, E is the field, and γ is a coefficient. Thus, the field dependent offset of the hysteresis loops is a combined result of these two effects.

The field dependent offset of the hysteresis loops, or the built-in potential in the graded ferroelectric thin films, was difficult to model. The two major difficulties were: i) the threshold field, E_{th}, was a material dependent value. For graded ferroelectric thin films, as the composition of the films varied, there would be a distribution of values of the threshold field, E_{th}, instead of a single valued threshold field, E_{th}; ii) the graded ferroelectric BST thin films were polycrystalline with multi-domains and were partially oriented as indicated by x-ray diffraction results discussed in chapter 2, and it's impossible to model it without information about the orientation of the films. However, sputtered homogenous BST thin films also showed field dependent offsets in the hysteresis loops, and it is much easier to model. In this case we can assume: i) a single valued threshold field, E_{th}, and ii) as indicated by the x-ray diffraction result discussed in

chapter 2, the polycrystalline films were approximately randomly oriented. When an electric excitation field E was applied to the film at a direction normal to the films surface, the domains which experienced a field larger than E_{th} along the crystal direction, were those with their directions between 0° to θ, where θ is determined by:

$$Cos\theta = \frac{E_{th}}{E} \qquad (4.4.2)$$

For a randomly oriented film with domains of various directions evenly distributed throughout the film, the portion of the domains with directions between 0° to θ is proportional to the volume of the cone within θ degree, and we can write it in mathematical form:

$$N \propto \frac{\int_0^{\theta} r^2 dr\, d\varphi \sin\theta\, d\theta}{\int_0^{180} r^2 dr\, d\varphi \sin\theta\, d\theta} = (1-\cos\theta) \qquad (4.4.3)$$

or substituting Cosθ with E_{th}/E, we have:

$$N \propto 1 - \frac{E_{th}}{E} \qquad (4.4.4)$$

So for the strained homogenous BST thin films, as the field increased the number of dipoles aligned would increase, as described in Eq. 4.4.4, and also the value of the individual dipole would also increase, as described in Eq. 4.4.1. Combining Eq. 4.4.1 and Eq. 4.4.4, we can get the expression of the field dependent offset of the hysteresis loop, or the built in dc potential of the films:

$$\Delta D \propto E^{\gamma}(1 - \frac{E_{th}}{E}) \qquad (4.4.5)$$

Using this formula, the experimental data for the field dependency of the offset for the sputtered homogenous film was fit. Fig. 4.4.1 shows both the experimental data and the fitting curve. In this particular case, E_{th} was 10 v/μm, and from the fitting result, γ was equal to 1.67. The E_{th} value observed was closed to the value of coercive field E_c, which is reasonable because coercive field E_c is field required to switch the polarization in a conventional ferroelectric crystal.

The temperature dependency of the offset can also be explained qualitatively by this model. From the illustration in Fig. 4.3.1, we can see that rising temperatures have two opposite effects on the offset of the hysteresis loops. One tends to decrease it while another tends to increase it. First, as the temperature rises, the individual dipole (or polarization) will become smaller since the distance in separation of charges decreases, as illustrated in Fig. 4.3.1 where the polarization (charge separation) value at equilibrium or minimum energy decreases with increasing temperatures. Second, also shown in Fig.4.3.1, as the temperature rises, the potential barrier between the two polarization states or the threshold field E_{th} will decrease. Thus, there will be more dipoles aligned when excited with an electric field. Furthermore, the thermal mismatch between the film and the substrate add more complicity to the phenomenon. The combination of these effects determine that the relation between temperature and offset of the hysteresis will be complicated, and likely will not be monotonic.

As discussed, the offset in the hysteresis loop or build-in potential in the films is caused by polarization. Once this polarization disappears, the offset should also

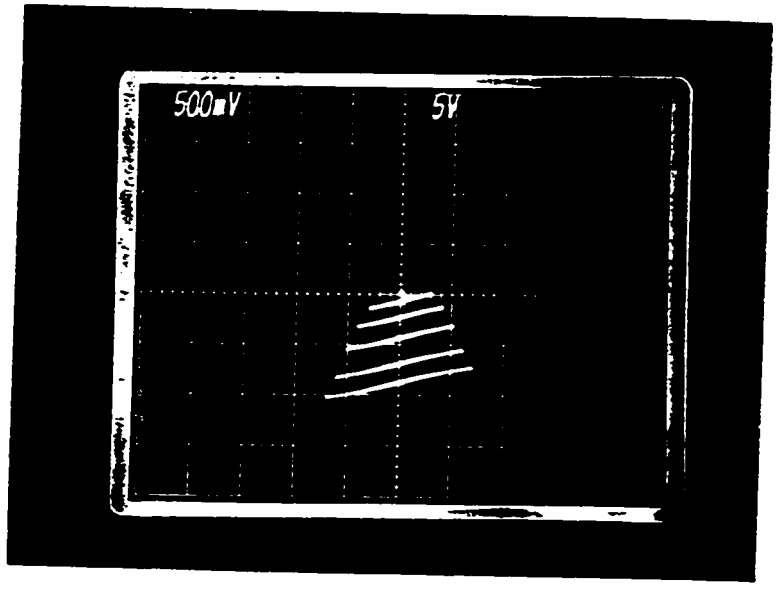

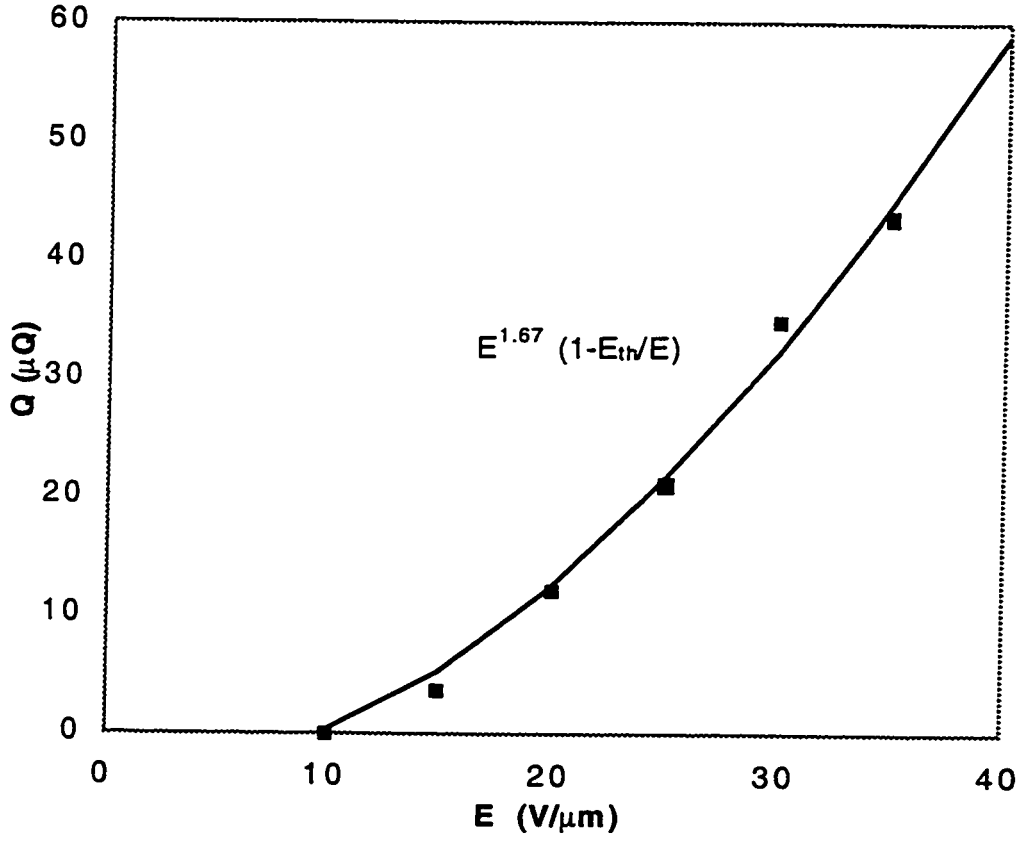

4.4.1 The field dependent offset of hysteresis loop for strained homogenous BST film and the fitting curve.

disappear. Based on this reasoning, we can predict that once the BST thin films translate from ferroelectric to paraelectric phase at some high temperature, the offset of hysteresis loops should disappear. This was tested by continuously raising the temperature and monitoring the hysteresis loops of the films. It was found that the films remained in the ferroelectric phase at very high temperatures (200 °C ~ 300 °C depending on the individual film). Fig. 4.4.2 shows the hysteresis loops of a graded film at various temperatures. We see that in this case, the film was clearly in the ferroelectric phase even at 160 °C, but the film became very lossy as the temperature was high. We also observed that the hysteresis loops of the film continuously shifted down as the temperature rose, but became unstable at high temperatures. When the temperature reached a certain point (300 °C for the particular film shown), a structure or phase transition appeared to have occurred. At this point, the hysteresis loops return to the original point as expected, and no further temperature or field dependent offset was observed after that. This is shown in Fig. 4.4.3, where the lossy hysteresis loops came back to the original point, and did not show any field dependent offset. The dielectric constant of the film was also examined at the highest temperature our measurement system could reach (about 320 °C). A rapid change appeared to start at about 300 °C, as shown in Fig. 4.4.4. This was consist with the observation of the dramatic change in hysteresis loops at this temperature, and also indicated a structure or phase transition. So, we see that the offset in the hysteresis loops does depend on the existence of the polarization in the ferroelectric phase. Also observed was that such structure or phase transitions were irreversible. No temperature or field dependent offset of hysteresis loops were observed after the films were cooled back to

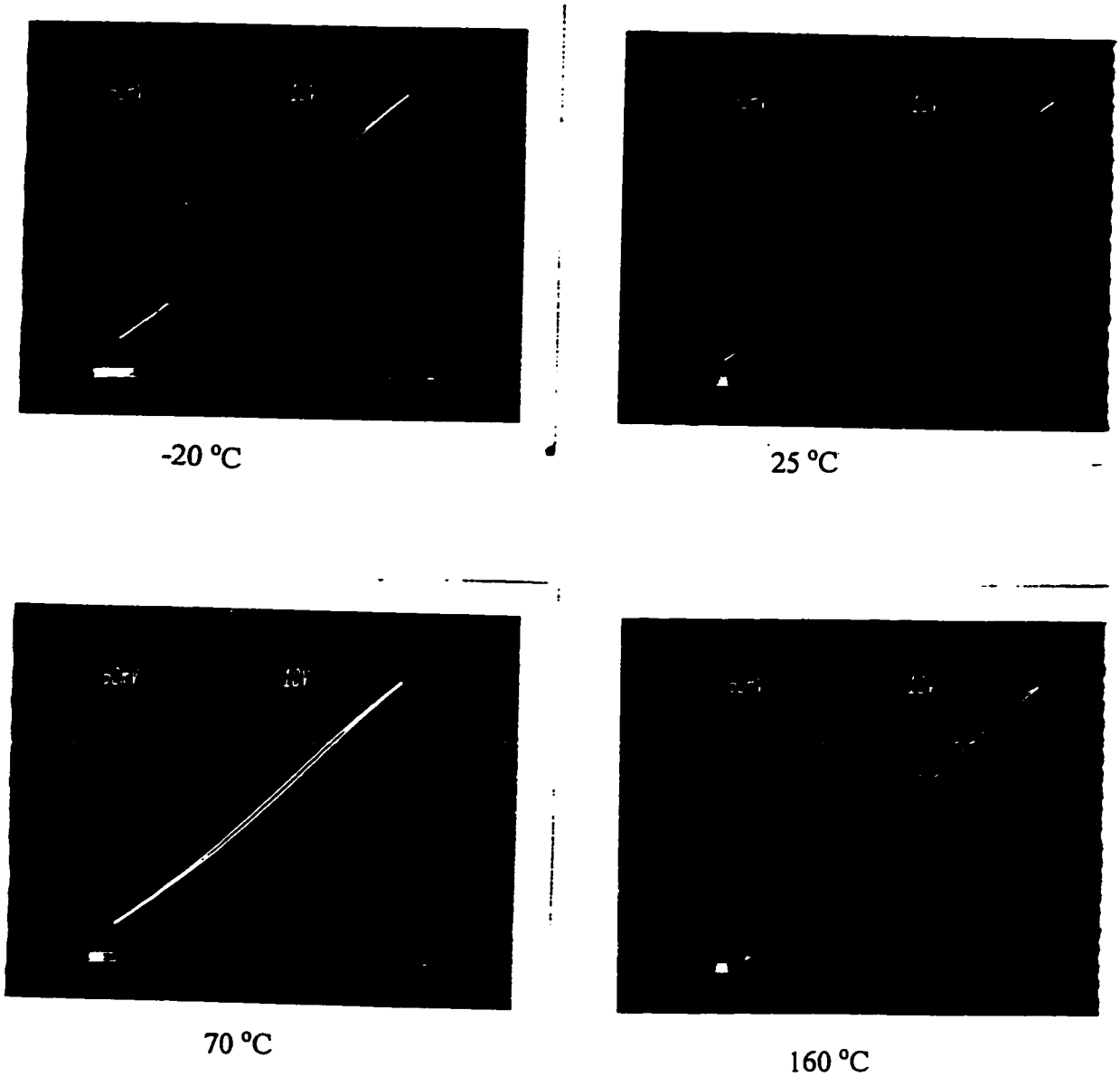

Fig. 4.4.2 The hysteresis loops of the graded film at various temperatures.

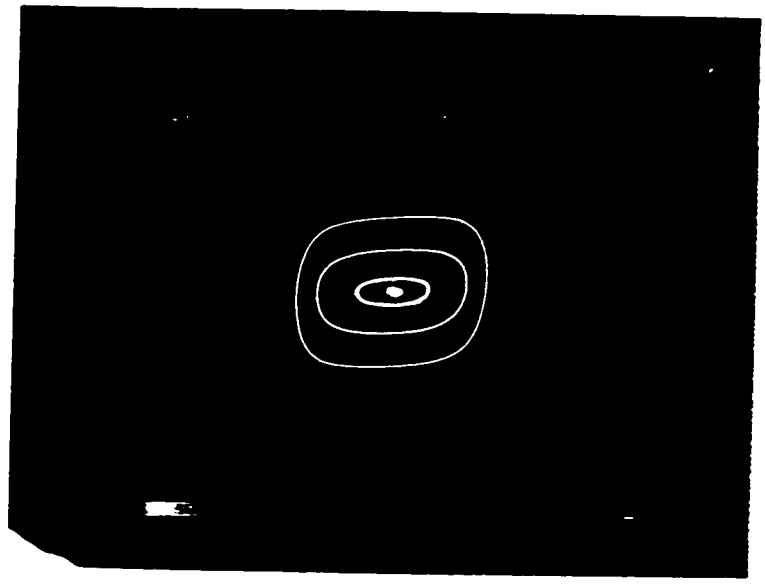

Fig. 4.4.3 The hysteresis loops of the graded BST film at 300 °C, show no offset effect.

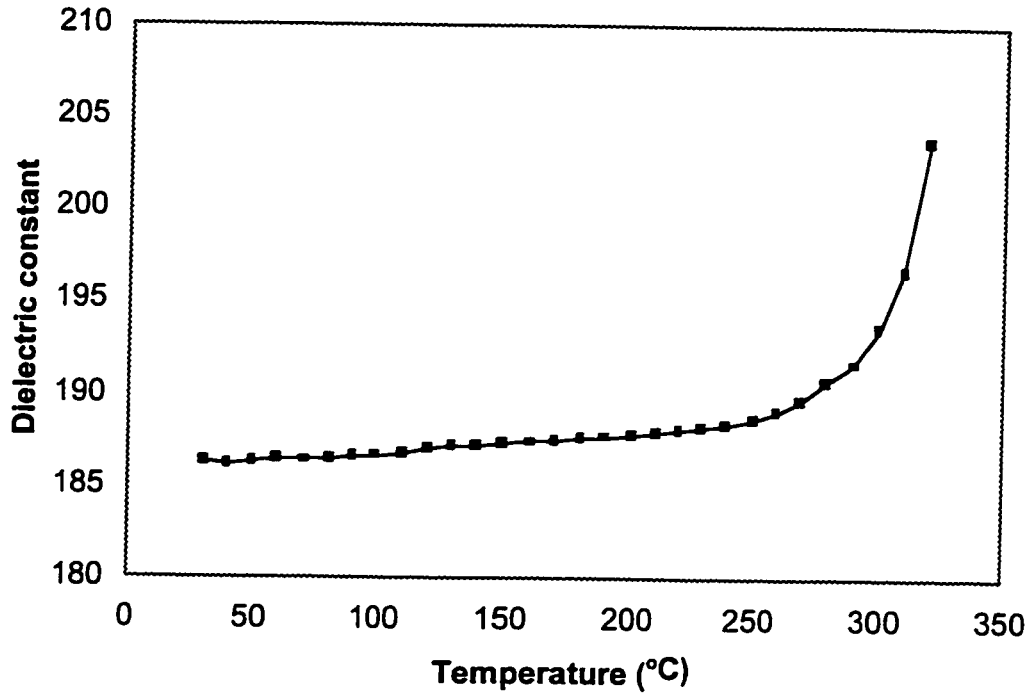

Fig. 4.4.4 The dielectric constant of the film at high temperature exhibited rapid change

room temperature. Bulk $BaTiO_3$ has a phase transition temperature at about 120 °C, and $Ba_{0.7}Sr_{0.3}TiO_3$ at about 25 °C. The phase transition temperature for the BST thin films in this study was much higher, and we believe that it was the strain in the films that helped hold the ferroelectric phase at such a high temperatures. The final relief of the strain at a high transition temperatures probably also caused severe structure damage to the films, hence the process was not reversible. The increase in transition temperature of ferroelectric thin films was also observed by many other researchers.[56, 70, 75,76] For example, it was reported that epitaxially grown BST thin films on Pt/MgO had phase transition temperatures as high as 200 °C.[75]

4.5 OFFSET OF HYSTERESIS LOOPS UNDER DC BIAS

So based on the model presented, we now understand that the offset in the hysteresis loops was the result of the asymmetrical nature of the graded films. The skewed G-P double wells created a preferred lower energy polarization state as shown in Fig. 5.3.1, and forced the dipoles to align. The skewed double wells were caused by strain in the films, which, in turn, was caused by compositional gradient or lattice and thermal mismatches from the substrate. Furthermore, it is not difficult to see that such skewed double wells can also be created by other means. For example, a dc electric bias field. The direction of the wells skew can be controlled by the direction of the bias field, as illustrated in Fig. 4.5.1. So, if the skewed double wells are the fundamental origin for the offset of the in hysteresis loops, then we should be able to further test this model by modifying such skewed wells electrically.

Up and down electric bias fields were superimposed with the electric excitation field and applied to the films. The hysteresis loops of the films behaved exactly as predicted: Up offset of the hysteresis loops were observed when the films were under up dc bias field. As shown in the Fig. 4.5.2 b, without a bias field, the sputtered BST film always exhibited a down shift in hysteresis loops when excited with an electric field. But as a dc bias field was applied, and the double wells switched direction they skew as illustrated in Fig.4.5.1, the direction of the offset was found switched correspondingly as shown in Fig.4.5.2 a.

Except for the switching of the direction of the offset from down to up when under an up bias field, all other behaves of the hysteresis loops including temperature dependency should remain the same. Temperature dependent studies confirmed this. As the temperature increased an up offset of the hysteresis loops was observed, in opposite to the down offset normally exhibited in unbiased films. The temperature dependent offset of the hysteresis loops was shown in Fig. 4.5.3.

The behave of the offset of the hysteresis loops under down bias field was also examined and was shown in Fig. 4.5.2 c. The threshold field, E_{th}, was found to decrease and a stronger dependency of the offset on the excitation field was also observed. The decrease in threshold field E_{th} can be easily understood from Fig. 4.5.1, where the barrier or E_{th} decreased as the double wells were further titled by a electric bias field. The decrease in threshold field E_{th} will make the dipole easier to be aligned when under field

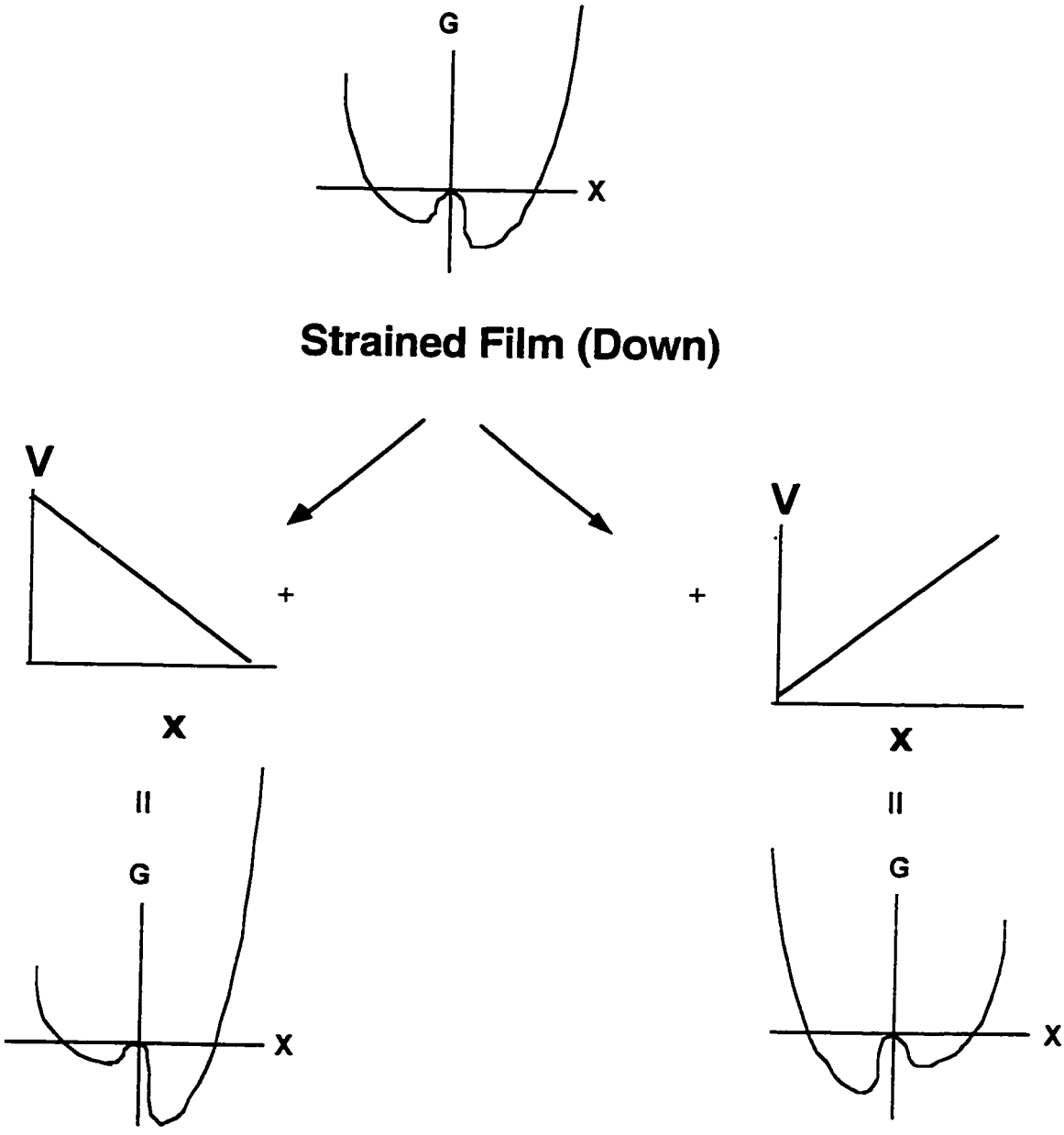

Fig. 4.5.1 Illustration of the dc bias field modified skewed P-G double wells. The direction of the wells skewed toward is determined by the direction of the bias field.

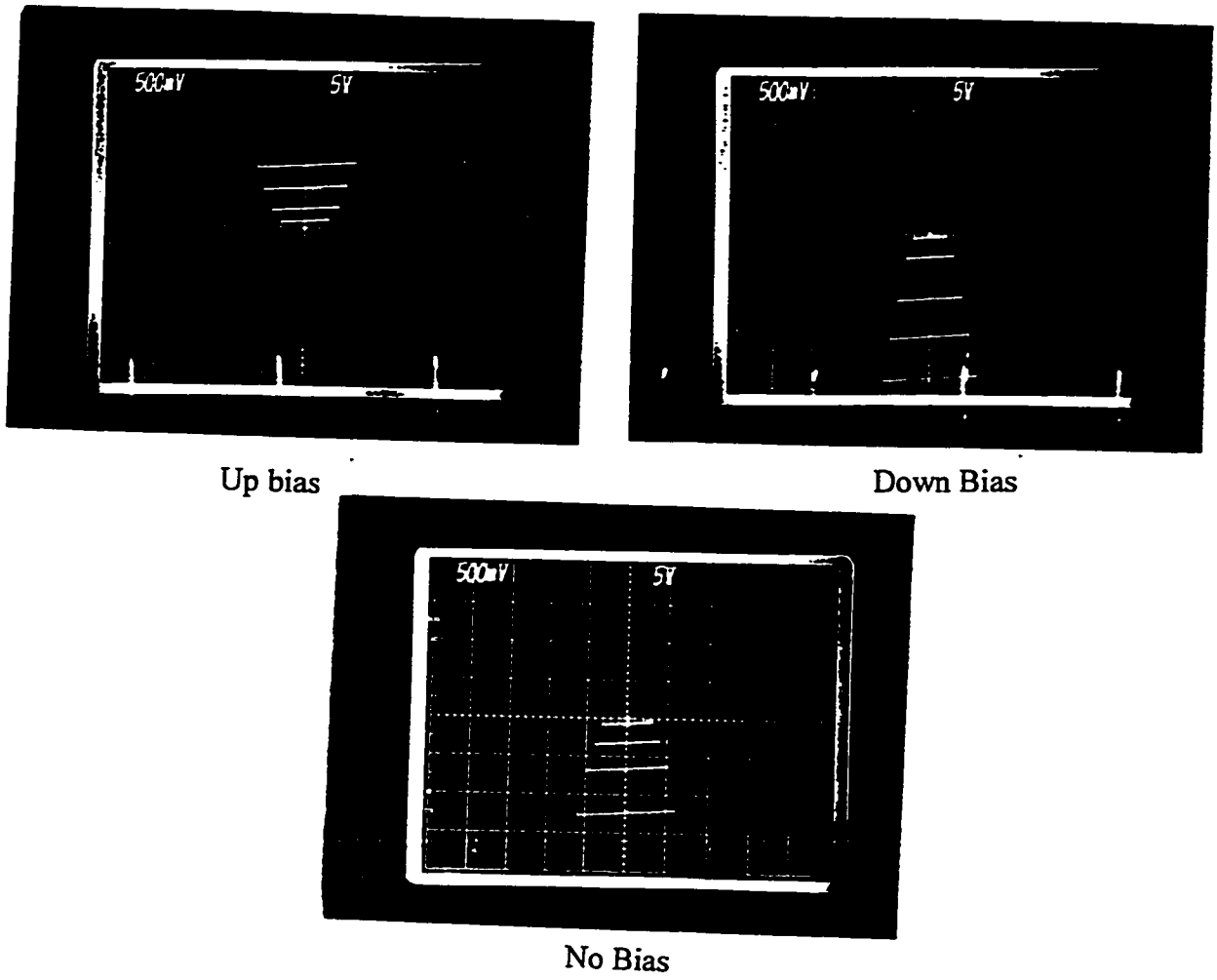

Fig. 4.5.2 The offsets of the hysteresis loops of the graded film under different bias conditions.

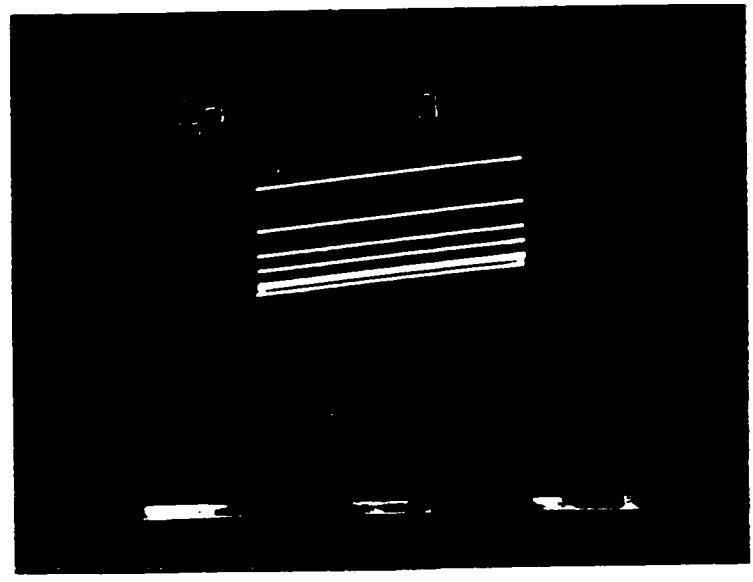

Fig. 4.5.3 The temperature dependent offset of the hysteresis loops of the film under up bias field.

excitation, hence a stronger field dependency of the offset was exhibited.

4.6 EFFECTIVE PYROELECTRIC COEFFICIENTS OF THE FILMS UNDER ELECTRIC BIAS FIELD

The difference between a conventional homogenous ferroelectric thin film and a graded ferroelectric thin film is that one is symmetric and the other is asymmetric in crystal structure, and the asymmetrical skewed G-P double wells in graded films are the origins of the observed new pyroelectric phenomena. And we showed that the skewed double were caused by strain in the films, and they could also be deliberately created by applying a dc bias field on the film. As discussed in previous sections, the more titled double well under bias created a larger field dependent offset in the hysteresis loops. The dc bias field is easy to control, and therefore the usefulness of using a dc bias field in engineering the skewed double well is worth further exploration. Based on the field dependent offset study, it is reasonable to guess that by further titling the double well using a dc bias field, larger temperature dependent offsets might be obtained, and hence an enhancement of the effective pyroelectric coefficient might be obtainable. Experiments were carried out to test this idea. The temperature dependency of the offset in the hysteresis loops of a graded film were examined under various bias conditions, and the effective pyroelectric coefficients as a function of temperature were calculated. The result is shown in Fig. 4.6.1. A general trend can be seen from these curves. The effective pyroelectric coefficients were largest under a down bias field, and smallest under up bias

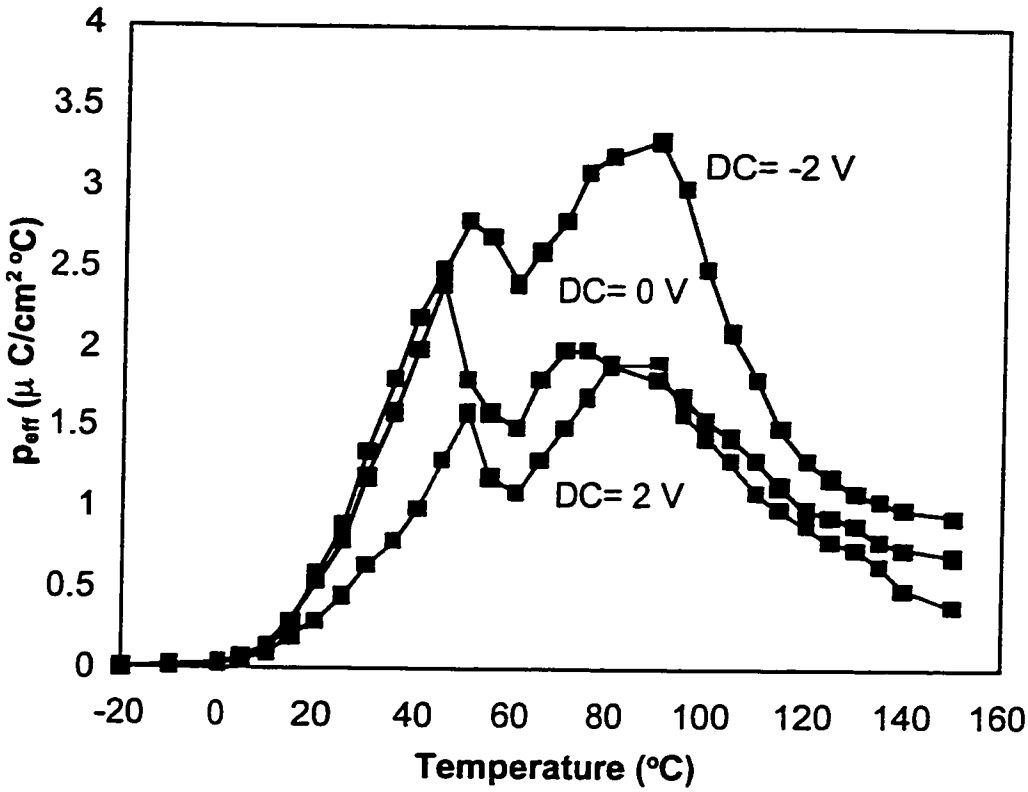

Fig. 4.6.1 Effective pyroelectric coefficients of a graded down film under different bias conditions.

field. They were in between without a bias field. So we see that the presence of a bias field can indeed enhance the effective pyroelectric coefficients of the films.

4.7 A NEW OPERATIONAL MODEL FOR FUTURE PYROELECTRIC INFRARED DETECTORS

The application of a bias field enhances the effective pyroelectric coefficients of the BST thin films, which is very important to infrared detection applications. But the real significance of application of a bias field to the ferroelectric thin films is probably its ability to create skewed G-P double wells. The new pyroelectric phenomena discussed in this study was first observed in graded ferroelectric thin films, and were later observed in strained homogenous ferroelectric BST thin films sputtered on platinum coated silicon substrates. Now based on our understanding of the mechanism of this phenomena, by applying a dc bias field, such pyroelectric effects should be obtainable from conventional ferroelectric thin films as well. This simple concept only require a new electrical operational mode (dc bias field + ac exciting field, or a asymmetric excitation field) to create a new type of highly sensitive pyroelectric infrared detector made from conventional homogenous ferroelectric thin films. This hypothesis has not been verified yet, since all the films formed in this study were sputter deposited and were strained. Strain free homogenous ferroelectric thin films are needed to completely test this hypothesis.

4.8 CONCLUSION

We have developed a model that successfully explains all of the new pyroelectric phenomena observed. The model suggests that the built in strain in the films, which altered the symmetrical nature of ferroelectric thin films, was the fundamental reason for the new pyroelectric effects. The built in strain in the films was introduced by compositional gradient in the films, and by lattice and thermal mismatch between the substrates and the films. Equivalently, a dc bias field was also used to alter and modify the symmetrical nature of ferroelectric thin films, and created similar pyroelectric effects as predicted. Finally, a new type of high sensitive pyroelectric infrared detector with a simple conventional thin film structure operated by the application of a dc bias field combined with a strong ac exciting field or a asymmetric periodic excitation field is proposed.

CHAPTER V

SUMMARY AND FUTURE WORK

This study explored the potential application of graded ferroelectric thin films in uncooled pyroelectric detectors. We built a magnetron sputter system, and developed a method for depositing compositional graded ferroelectric thin films using rf magnetron sputtering - a silicon compatible thin film fabrication process. This technique showed great control in fabricating graded ferroelectric thin films, nearly linear graded ferroelectric BST thin films with various compositional gradients were formed. The films fabricated with this method exhibited superior pyroelectric properties. By obtaining giant effective pyroelectric coefficients from graded ferroelectric BST thin films, we demonstrated their potential in fabricating low cost high sensitivity uncooled pyroelectric infrared detectors. Structural and other properties of the graded ferroelectric BST thin films were characterized using various techniques, and were correlated with each other. The films were found to be strained polycrystalline, dense and crack free. The basic physics of the new pyroelectric effects from the graded thin film devices were investigated, and a phenomenological model was proposed to explain the experimental observations. The model suggests that the strain built in the films, which altered the symmetrical nature of the ferroelectric thin films, was the fundamental reason for the new pyroelectric effects. The strain built in the films was introduced by compositional gradient in the films, and by lattice and thermal mismatch between substrates and the films. The model not only successfully explains the experimental results previously observed, but also correctly

predicted the results of some newly designed experiments. It predicted that a dc bias field could also be used to alter and modify the symmetrical nature of ferroelectric thin films equivalently as strain, and created similar pyroelectric effects. The effect of a bias field on the films was verified experimentally.

From our current understanding of the origin and the mechanism of the new pyroelectric phenomena discussed in this study, it is possible to extend such phenomena even in a conventional thin film. When a DC bias field is applied, a conventional thin film may become equivalent to a graded film in term of asymmetric D-E double well described earlier. Thus, the film structure of future pyroelectric infrared detectors can be significantly simplified. The films (both graded and homogenous) formed by sputtering in this study were all strained, hence could not be used to verified this hypothesis. This idea need to be tested and explored in future. We proposed to create unstained homogenous thin films using other deposition methods, such as MOD on various substrates in future study, and also test various operational modes, such as application of both a dc bias field and an ac excitation field or a asymmetric excitation field to the films.

APPENDIX

SUPPLEMENTAL DATA

As mentioned earlier in the dissertation, pyroelectric properties of graded films with various gradients were compared. The original propose was try to optimize the effective pyroelectric coefficients of the films. Although the correlation between the compositional gradients and the effective pyroelectric coefficients of the films was not able to be determined because of the high fluctuation of the data obtained, we present some typical data obtained from films with various gradients for the achieve propose.

The data presented in this appendix include effective pyroelectric coefficients Vs. temperature curves for graded down $Ba_xSr_{1-x}TiO_3$ films with four different compositional gradients ((1) x from 1 to 0.8, (2) x from 1 to 0.7, (3) x from 1 to 0.6, and (4) x from 0.9 to 0.4). The effective pyroelectric coefficients Vs. temperature curves for graded up $Ba_xSr_{1-x}TiO_3$ films (x from 0.7 to 1), and for homogenous $Ba_xSr_{1-x}TiO_3$ films (x= 0.7, and x = 0.6) are also presented. All the films are 200 nm thick.

In additional to the effective pyroelectric coefficients data, the x-ray diffraction results for the homogenous $Ba_xSr_{1-x}TiO_3$ film (x=0.6), $BaTiO_3$ film, and the graded down $Ba_xSr_{1-x}TiO_3$ film (x from 1 to 0.6) are also included.

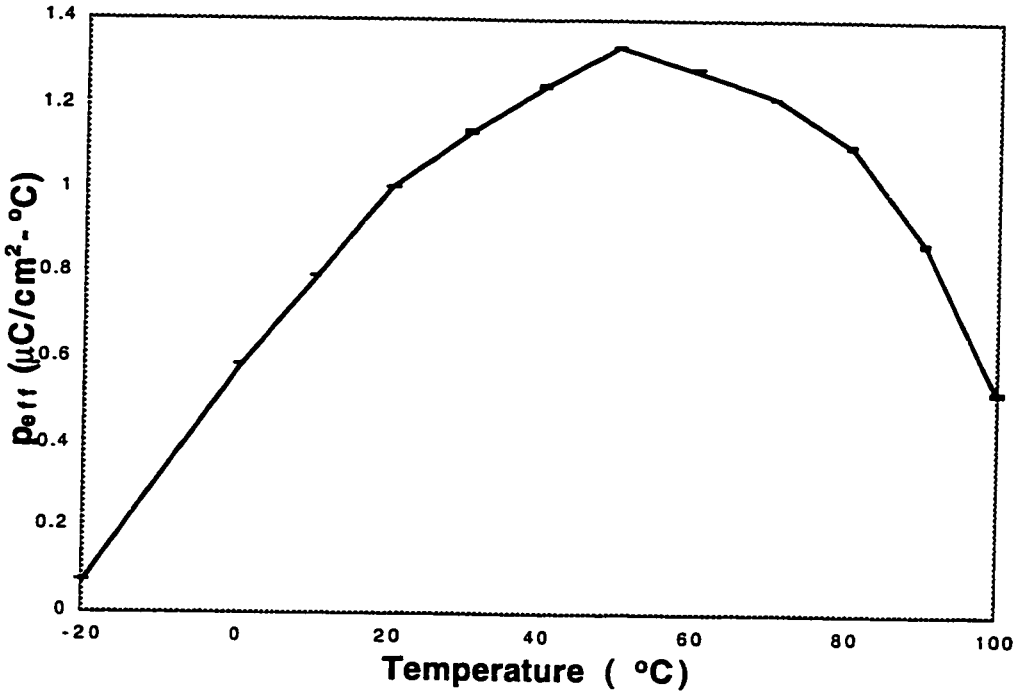

Fig. p.1. Another example of the p_{eff} vs. temperature curve of graded down $Ba_xSr_{1-x}TiO_3$ films (x from 1 to 0.7). The excitation field was Sine wave with 35 V/μm peak value.

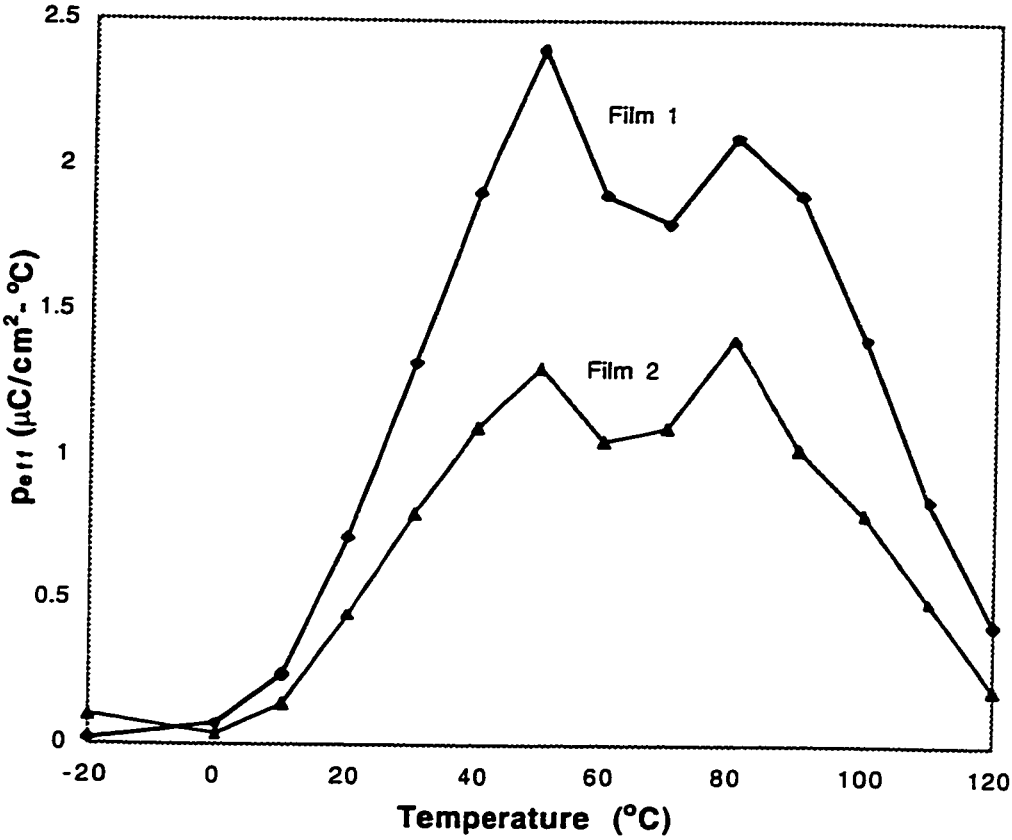

Fig. p.2. The p_{eff} vs. temperature curves of typical graded down $Ba_xSr_{1-x}TiO_3$ films (x from 1 to 0.8). The excitation field was Sine wave with 55 V/μm and 40 V/μm peak values for film1 and film2 respectively.

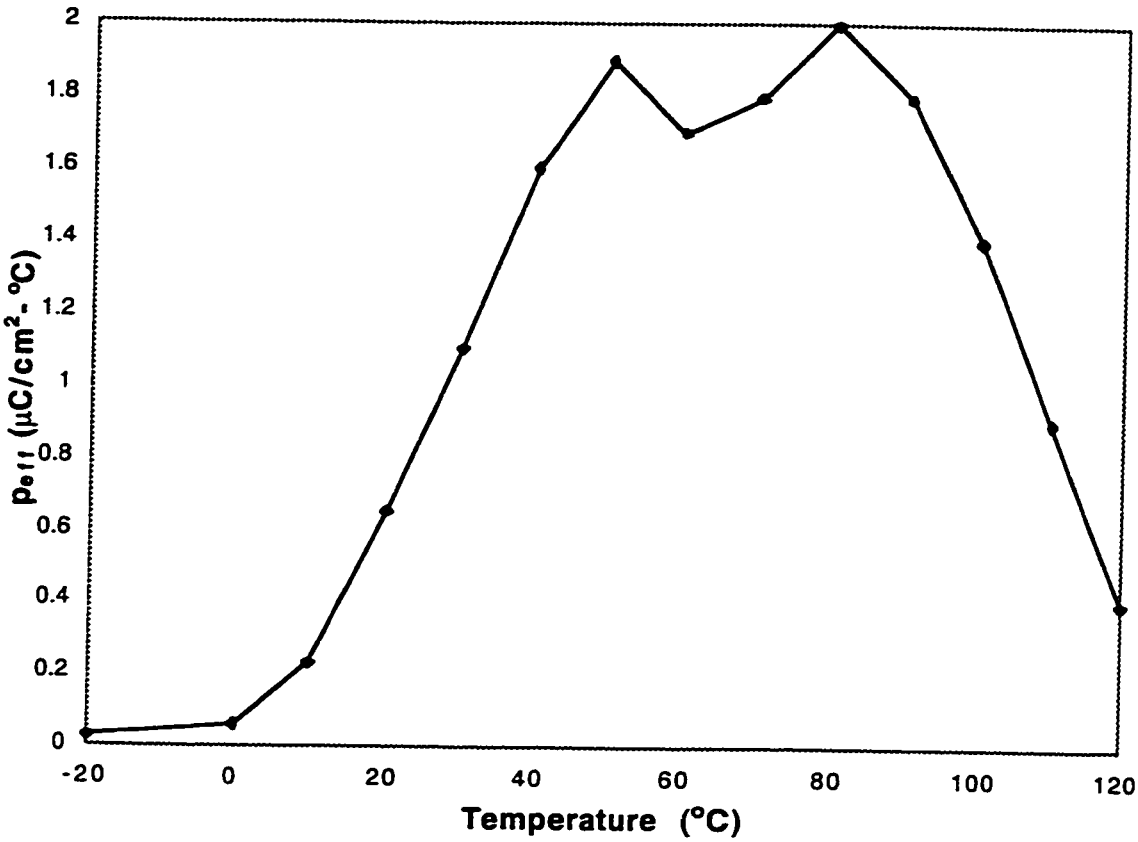

Fig. p3. The p_{eff} vs. temperature curve of a typical graded down $Ba_xSr_{1-x}TiO_3$ films (x from 1 to 0.6). The excitation field was Sine wave with 55 V/μm peak value.

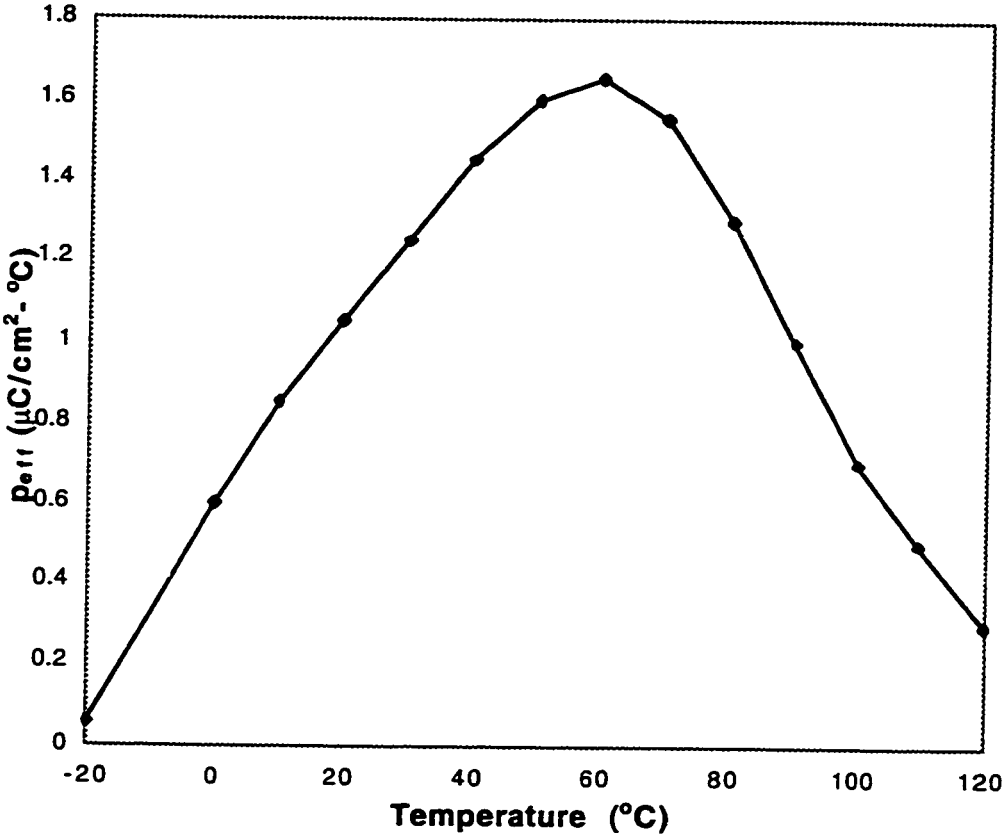

Fig. p.4. The p_{eff} vs. temperature curve of a typical graded down $Ba_xSr_{1-x}TiO_3$ films (x from 0.9 to 0.6). The excitation field was Sine wave with 45 V/μm peak value.

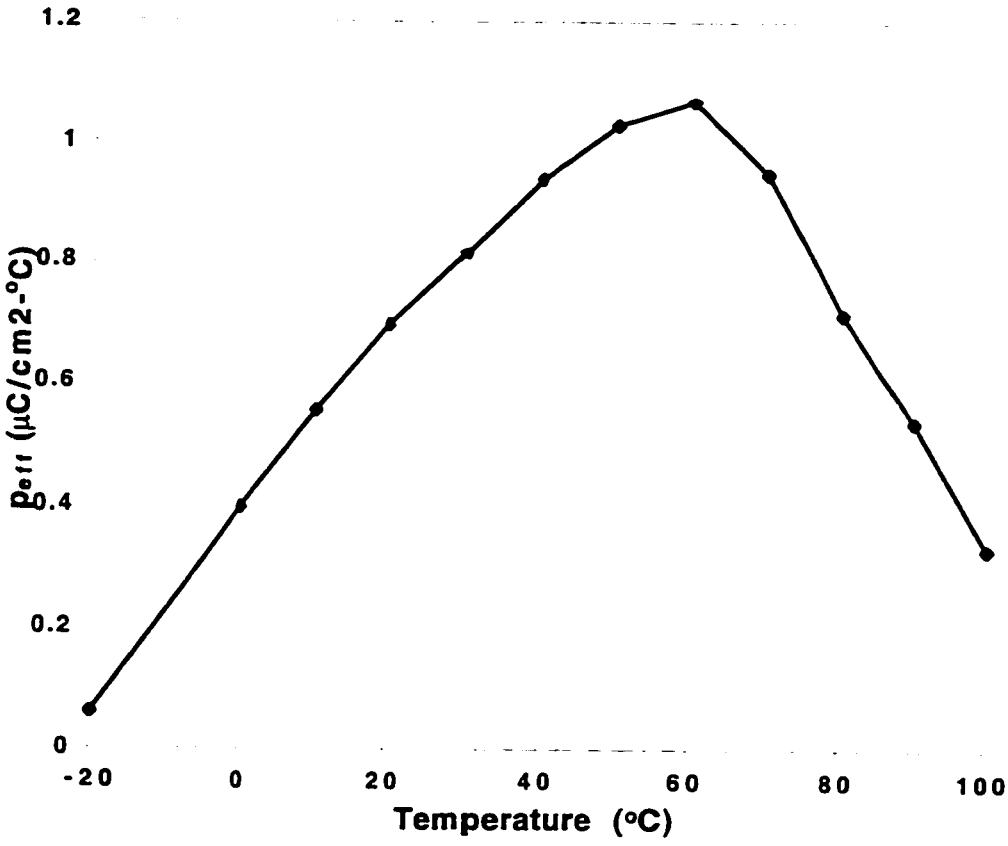

Fig. p.5. The p_{eff} vs. temperature curve of a typical graded up $Ba_xSr_{1-x}TiO_3$ film (x from 0.7 to 1). The excitation field was Sine wave with 40 V/μm peak value.

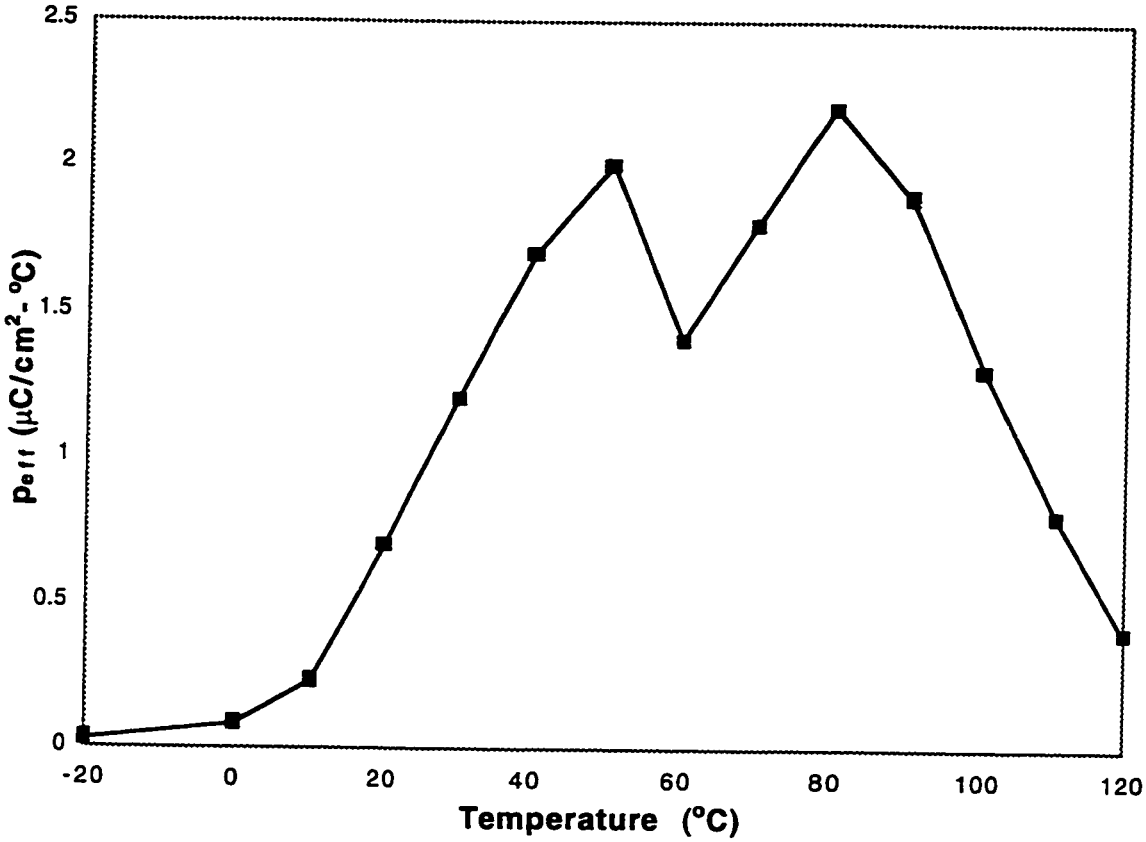

Fig. p.6. The p_{eff} vs. temperature curve of a typical graded up $Ba_xSr_{1-x}TiO_3$ film (x from 0.7 to 1). The excitation field was Sine wave with 50 V/μm peak value.

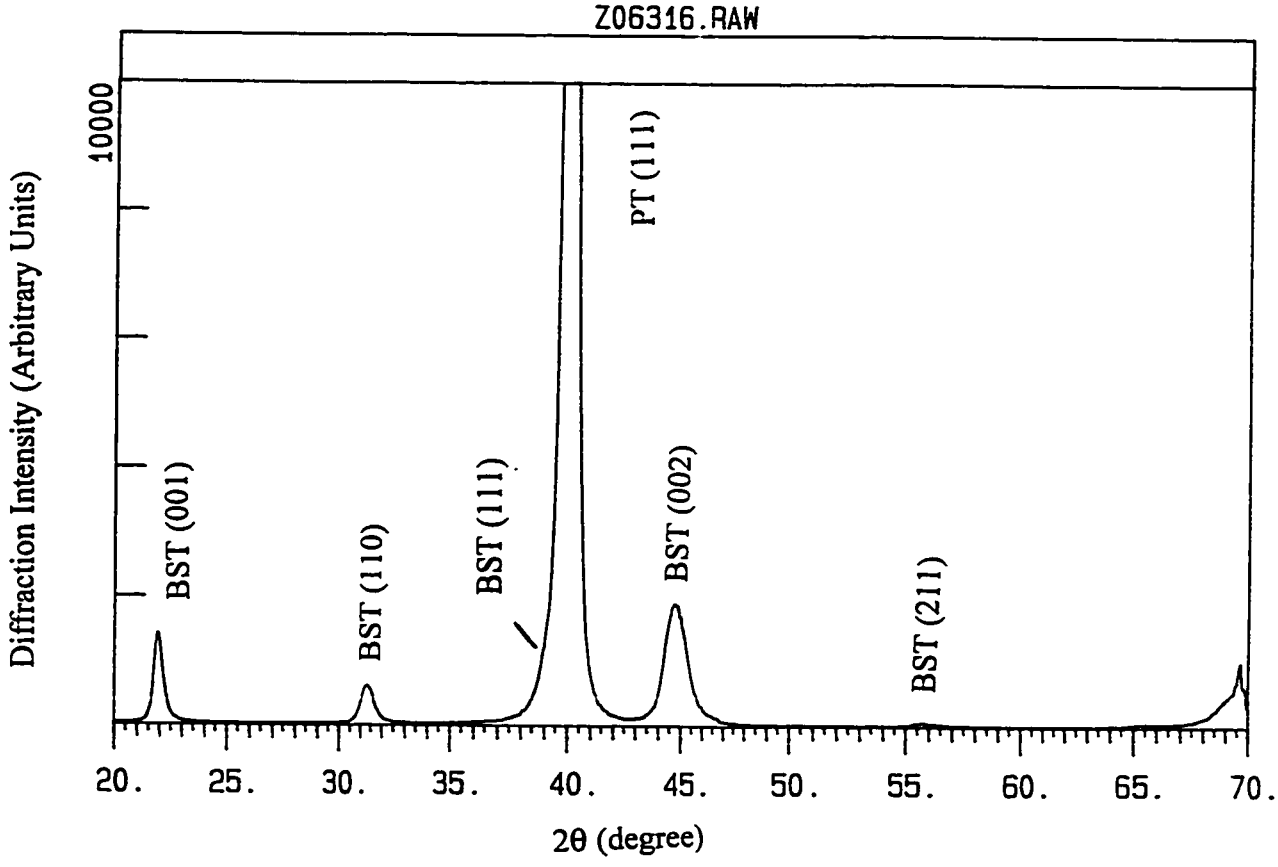

Fig. p.7. The x-ray diffraction result for the homogenous $Ba_xSr_{1-x}TiO_3$ film (x=0.6).

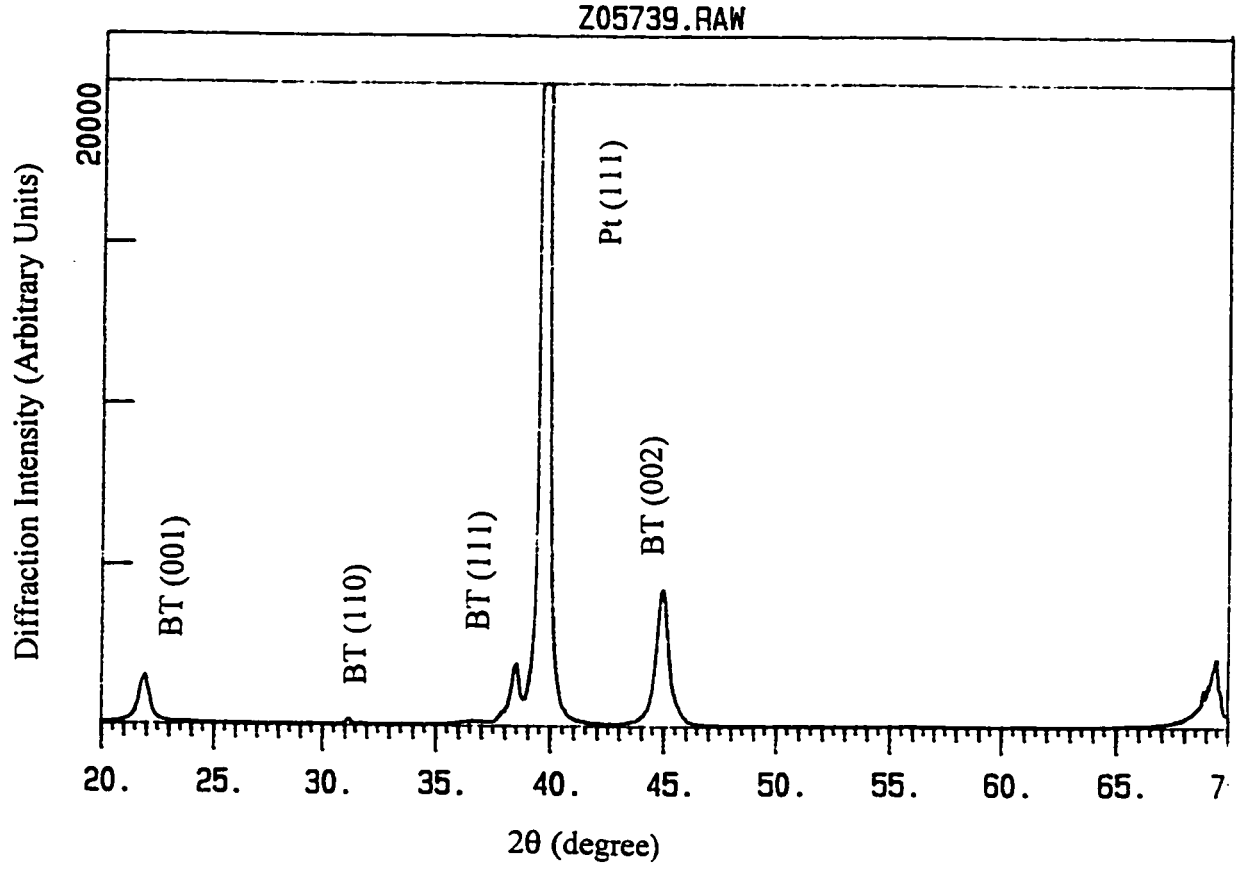

Fig. p.8. The x-ray diffraction result for the $BaTiO_3$ film.

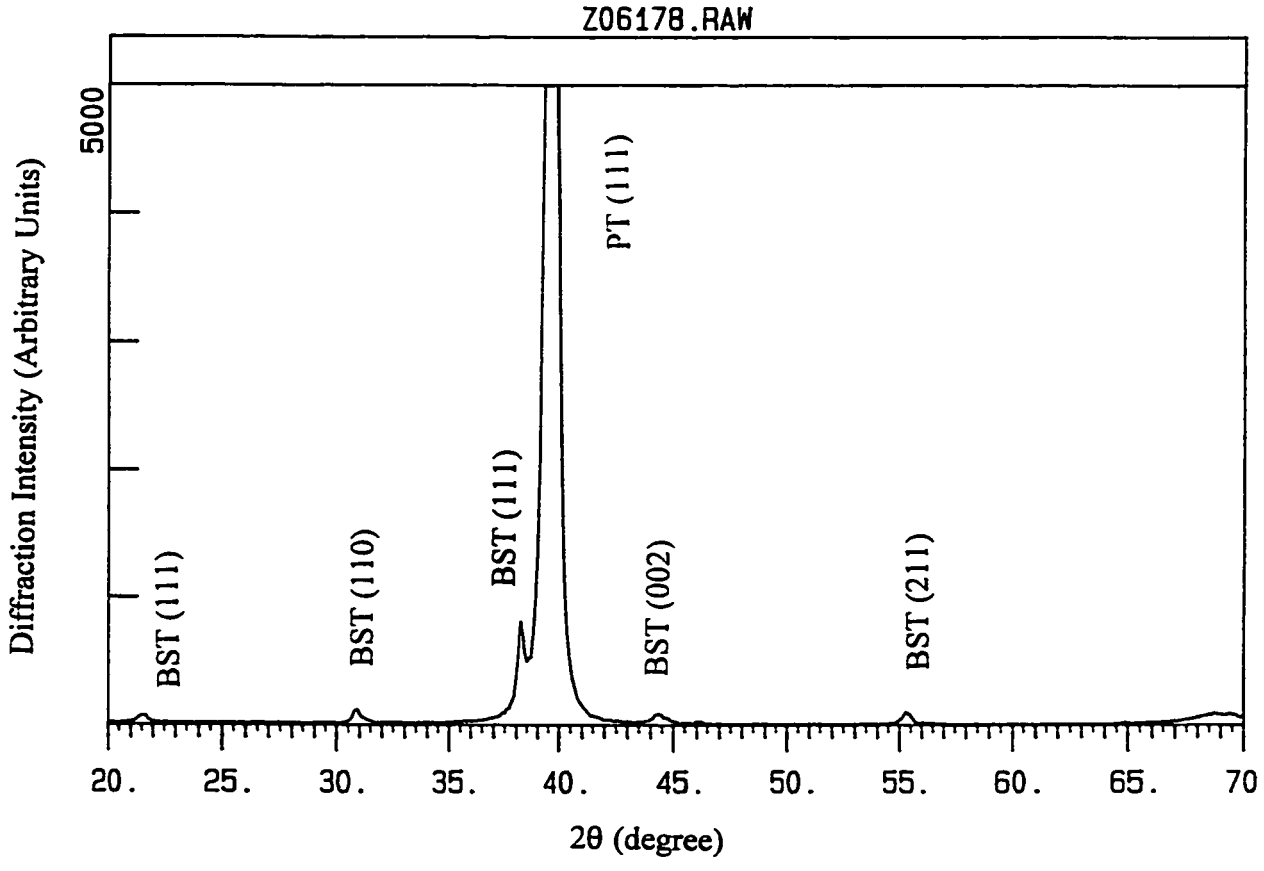

Fig. p.9. The x-ray diffraction result for the graded down $Ba_xSr_{1-x}TiO_3$ film (x from 1 to 0.6).

REFERENCES

1. M.E. Lines and A. M. Glass, *Principles and Applications of Ferroelectrics and Related Materials* ,Oxford University Press, Oxford, England, 1977, Chapter 1.

2. S. T. Liu and D. Long, Proc. IEEE **66**, 14 (1978).

3. R. W. Whatmore, P. C. Osbond and N. M. Shorrocks, Ferroelectrics **76**, 351 (1987).

4. L. E. Cross and K. H. Hardtl, Encyclopedia of Chemical Technology **10**, 1 (1980).

5. R. Watton, Integrated Ferroelectrics **4**, 175 (1994).

6. C. Lucas, Sensors and Actuators A **25**, 147 (1991).

7. A. Tebo, Laser Focus, 68 (July, 1984).

8. N. M. Shorrocks, S. G. Porter, R. W. Whatmore, A. D. Parsons, J. N. Gooding and D. J. Pedder, Proc. SPIE **1320**, 88 (1990).

9. E. H. Putley, Infrared Physics **29**, 139 (1979).

10. N. M. Shorrocks and I. M. Edwards, Proc. IEEE 58 (1991).

11. P. W. Kruse, Proc. IEEE 643 (1995).

12. J. C. Slater, in Ferroelectricity, edited by E. F Weller, Elsevier Publish, New York,1967. P1 - P15.

13. M.E. Lines and A. M. Glass, *Principles and Applications of Ferroelectrics and Related Materials* ,Oxford University Press, Oxford, England, 1977, Chapter 3.

14. C. B. Sawyer and C. H. Tower, Phys. Rev. **35**, 269 (1930).

15. M.E. Lines and A. M. Glass, *Principles and Applications of Ferroelectrics and Related Materials* ,Oxford University Press, Oxford, England, 1977, Chapter 16.

16. M.E. Lines and A. M. Glass, *Principles and Applications of Ferroelectrics and Related Materials* ,Oxford University Press, Oxford, England, 1977, Chapter 6.

17. S. Li, J. A. Eastman, R. E. Newnham and L. E. Cross, Phys. Rev. B **55**, 1 (1996).

18. V. S. Tiwari, N. Singh and D. Pandey, J. Phys.: Condens. Matter **7**, 1441 (1994).

19. M.E. Lines and A. M. Glass, *Principles and Applications of Ferroelectrics and Related Materials* ,Oxford University Press, Oxford, England, 1977, Chapter 8.

20. A. F. Devonshire, Philosophical Magazine **40**, 1040 (1949).

21. A. F. Devonshire, Philosophical Magazine **42**, 1065 (1951).

22. A. S. Shaikh, R. W. Vest and G. M. Vest, IEEE Trans. on Ultrasonics **36**, 407 (1989).

23. G. Arlt, D. Hennings and G. de With, J. Appl. Phys. **58**, 1619 (1985).

24. G. Arlt and H. Peusens, Ferroelectrics **48**, 213 (1983).

25. J. Paletto, G. Grange, R. Goutte and L Eyraud, J. Phys. D: Appl. Phys. **7**, 78 (1974).

26. Y. Hirata, A. Nitta, S. Sameshima and Y. Kamino, Materials Letters **29**, 229 (1996).

27. M. A. Saifi and L. E. Cross, Phys. Rev. B **2**, 677 (1970).

28. A. Z. Kain, C. L. Pettie-Hall, K. P. Daly, A. E. Lee, R. Hu and J. F. Burch, IEEE Trans. on Applied Superconductivity **3**, 1421 (1993).

29 W. B. Pennebaker, IBM J. Res. Develop., **5**, 686 (1980).

30. K. Takemura, T. Sakuma and Y. Miyasake, Appl. Phys. Lett. **64**, 2967 (1994).

31. Y. Miyasake and S. Matsubara, Proc. IEEE, 121 (1991).

32. A. I. Kingon, S. K. Streiffer, C. Basceri and S. R. Summerfelt, MRS Bulletin **21**, 46 (July, 1996).

33. A. Yuuki, M. Yamamuka, T. Makita, T. Horikawa, T. Shibano, N. Hirano, H. Maeda, N. Mikami, K. Ono, H. Ogata and H. Abe, IEEE IEDM-95, 115 (1995).

34. S. Yamamichi, P-Y. Lesaicherre, H. Yamaguchi, K. Takemura, S. Sone, H. Yabuta, K. Tokashiki, Y. Nakajima, S. Ohnishi, K. Tokashiki, Y. Hayashi, Y. Kato, Y. Miyasaka, M. Yoshida and H. Ono, IEEE IEDM-95, 119 (1995).

35. C-J. Peng and S. B. Krupanidhi, J. Mater. Res. **10**, 708 (1995).

36. A. B. Catalan, J. Mantese, A. L. Micheli and N. W. Schubring, J Appl. Phys. **76**, 2541 (1994).

37. E. Wiener-Avnear, Appl. Phys. Lett. **65**, 1784 (1994).
38. B. M. Kulwicki, A. Amin, H.R. Beratan and C.M. Hanson, *Proc. 8th Int. Symp. Appl. Ferroelectrics*, IEEE, 1(1992).

39. C. Hanson and H. Beratan, *Proc. 9th Int. Symp. Appl. Ferroelectrics*, IEEE, 657 (1994).

40. C. Ye, T. Tamagawa and D. L. Polla, J. Appl. Phys. **70**, 5538 (1991).

41. D. L. Polla, C. Ye and T. Tamagawa, Appl. Phys. Lett., **59**, 3539 (1991).

42. K. C. McCarthy, F. S. McCarthy, G. Teowee, T. J. Bukowski, T. P. Alexander and D. R. Uhlmann, Integrated Ferroelectrics, **V17, N1 - 4**, (377) 1997

43. R. Bruchhaus, D. Pitzer, R. Primig, M. Schreiter, W. Wersing, N, Neumann, N. Hess, J. Vollheim, R. Kohler and M. Simon, Integrated Ferroelectrics, **V17, N1 - 4**, (369) 1997.

44. A. Patel, N. M. Shorrocks, R. W. Whatmore, MRS Symp. Proc. **243**, 67 (1992).

45. M. S. Mohammed, R. Naik, J. V. Mantese, N. W. Schubring, A. L. Micheli and A. B. Catalan, J. Mater. Res., **11**, 2588 (1996).

46. C. Allard, *Fiber optics Handbook for Engineers and Scientists*, McGraw-Hill, New York, 1990.

47. Sampath, H.Herman, N.Shimoda, T.Saito, MRS Bulletin **20**, 21 (January, 1995)

48. N. W. Schubring, J. V. Mantese, A. L. Micheli, A. B. Catalan, and R. J. Lopez, Phys. Rev. Lett. **68**, 1778 (1992).

49. J. V. Mantese, N. W. Schubring, A. L. Micheli, A. B. Catalan, M. S. Mohammed, R. Naik and G. Auner, Appl. Phys. Lett. **71**, 2047 (1997).

50. J. V. Mantese, N. W. Schubring, A. L. Micheli, A. B. Catalan, Appl. Phys. Lett. **67**, 721 (1995).

72. S. M. Rossnagel, in *Thin Films Processes II*, Edited by J. L. Vossen and W. Kern, Academic Press, London, 1991. P11 - P77.

52. T. Miura and T. Asamaki, Thin solid Films **281**, 190 (1996).

53. T. Horikawa, N. Mikami, T. Makita, J. Tanimura, M. Kataoka, K. Sata and M. Nunoshita, Jan. J. Appl. Phys. **32**, 4126 (1993).

54. S-G. Yoon, A. Safari, Thin Solid Films **254**, 211 (1995).

55. J. W. Jang, S. J. Chung, W. J. Cho, T. S. Hahn and S. S. Choi, J. Appl. Phys. **81**, 6322 (1997).

56. K. Abe, S. Komatsu, J. Appl. Phys. **77**, 6461 (1995).

57. H. Tabata, H. Tanaka and T. Kawai, Appl. Phys. Lett. **65**, 1970 (1994).

58. H. Tabata, H. Tanaka, T. Kawai and M. Okuyama, Jan. J. Appl. Phys. **34**, 544 (1995).

59. F. Tcheliebou and S. Baik, J. Appl. Phys. **80**, 7046 (1996).

60. V. Srikant, E. J. Tarsa, D. R. Clarke, and J. S. Speck, J. Appl. Phys. **77**, 1517 (1995).

61. H. Shigetani, M. Fujimoto, W. Sugimura, Y. Matsui and J. Tanaka, Mater. Sci. Eng. **B41**, 148 (1996).

62. T. Maeda, G. H. Lee, T. Ohnishi, M. Kawasaki, M. Yoshimoto and H. Koinuma, Mater. Sci. Eng. **B41**, 134 (1996).

63. C. S. Chern, S. Liang, Z. Q. Shi, S. Yoon, A. Safari, B. H. Goodreau, T. J. Marks, S. Y. Hou, Appl. Phys. Lett. **64**, 3181 (1994).

64. D. L. Kaiser, M. D. Vaudin, L. D. Rotter, Z. L. Wang, J. P. Cline, C. S. Hwang, R. B. Marinenko and J. G. Gillen, Appl. Phys. Lett. **66**, 2801 (1995).

65. M. Yoshida, H. Yamaguchi, T. Sakuma and Y. Miyasaka, J. Electrochem. Soc. **142**, 244 (1995)

66. D. Tahan, A. Safari, and L. C. Klein, Proc. IEEE. 13th International Symposium on Applications of Ferroeletcrics, 427 (1995).

67. M. Sedlar, M. Sayer and L. Weaver, J. Sol-Gel Science and Technology **5**, 201 (1995).

68. J. Kim, S. I. Kwun and J. G. Yoon, Proc. IEEE **20**, 423 (1995).

69. D. Ivanov, M. Caron, L. Quellet, S. Blain, N. Hendricks and J. Currie, J. Appl. Phys. **77**, 2666 (1995)

70. J. R. Hanrahan, E. Sanchez and J. J. Santiago, Thin Solid Films **202**, 235 (1991).

71. J. J. Xu, A. S. Shaikh and R. W. Vest, IEEE Trans. on Ultrasonics **36**, 307 (1989).

72. S. B. Krupanidhi and C. J. Peng, Thin Solid Films **305**, 141 (1997).

73. W. Ousi-Benomar, S. S. Xue and R. A. Lessard, J. Mater. Res. **9**, 970 (1994).

74. B. D. Cullity, *Elements of X-ray Diffraction*, 2nd Edition, Addison-Wesley, 1978. Chapter 3.

75 K. Iijima, Y.Yano, T. Terashima, and Y. Bando, Oyo-Butsuri, **62**, 1250 (1993)

76. K. Abe, S. Komatsu, N. Yanase, K. Sano and T. Kawakubo, Jan. J. Appl. Phys. **36**, 5846 (1997).

ABSTRACT

NEW PYROELECTRIC PHENOMENA FROM GRADED FERROELECTRIC BARIUM STRONTIUM TITANATE THIN FILMS

by

FENG JIN

May, 1998

Advisor: Professor Gregory Auner

Major: Electrical Engineering

Degree: Doctor of Philosophy

In this study we explored the potential application of graded ferroelectric thin films in uncooled pyroelectric detectors. We built a magnetron sputter system, and developed a method of deposited compositional graded ferroelectric thin films using rf magnetron sputtering, a silicon compatible thin film fabrication process. By obtaining giant effective pyroelectric coefficients from graded ferroelectric BST thin films, we demonstrated their potential in fabricating low cost high sensitive uncooled pyroelectric infrared detectors. Structure and properties of the graded ferroelectric BST thin films were characterized using various techniques, and were correlated with each other. The basic physics of the new pyroelectric effects from the graded thin film devices were investigated, and a phenomenological model was proposed to explain the experimental observations. The model not only successfully explained the experimental results previously observed, but also correctly predicted the results of some newly designed

experiments. From our current understanding of the origin and mechanism of the new pyroelectric phenomena discussed in this study, we proposed to further simplify the structure of future pyroelectric infrared detectors by adopting a new operational mode.

AUTOBIOGRAPHICAL STATEMENT

Feng Jin received his B.S degree from Physics Department, Fudan University, Shanghai, China, in 1985, and his M.S. degree from Physics Department, Fisk University, Nashville, Tennessee, in 1993.

From 1985 to 1991, He worked in Shanghai Electric Light Sources Company as a research and development engineer, and as a quality control engineer. During that period of time, he established one of the first few spectroscopic laboratories in the lighting industry in China, and devised a practical method of optimizing the color rendering index of compact low pressure Ar-Hg discharge fluorescent lamps. He was a certified engineer in Shanghai, China.

He came to the U.S. in 1991. From 1991 to 1993, he was a graduate research assistant at Photonic Materials Characterization Laboratories, Fisk University, where he studied the initial nucleation process of crystal growth from solution using FTIR and Raman spectroscopy.

He was a graduate research assistant, and a graduate teaching assistant at Wayne State University from 1993 to 1998, where he worked on polarized light scattering instrumentation, ferroelectric thin films and wide band gap nitride thin films growth and characterization. From 1996 to 1998, he worked on his dissertation research project at both General Motors Research and Wayne State University. He also taught four laboratory classes on electronics, electrical circuit, computer and physical chemistry during that period of time.

Feng Jin is a member of the Materials Research Society and IEEE. He published 7 technical papers, and gave 5 presentations in professional conferences in the past few years.